



METEOROLOGY HYDROLOGY
AND WATER MANAGEMENT

IMGW-PIB Science Journal since 2013

VOL. 11 | ISSUE 1 | 2023



Reducing flood hazard by effective polder operation: A case study of the Golina polder

Albert Malinger, Małgorzata Wawrzyniak, Maksymilian Rybacki, Ewelina Szalkiewicz

Institute of Meteorology and Water Management – National Research Institute

Tomasz Dysarz

Poznan University of Life Sciences, Department of Hydraulic and Sanitary Engineering

Abstract

The aim of the study was to determine an effective variant of operation of the Golina polder to reduce flood hazard in the Warta River valley. We implemented a trial-and-error method for the development of computational variants. Our approach was based on staged analyses of alternatives, which took into account different locations and parameters of the inlet and outlet-controlling structures. Various control scenarios for flooding and draining the polder were also considered. A hybrid hydrodynamic model consisting of a 1D part for the main river area and a 2D part for the polder area was used for calculations. The model was built based on a digital elevation model (1 m resolution) and channel sections of the Warta River. The calibration was based on data collected during the flood in 2010 from the water gauge Slawsk (located directly at the Warta River) and water surface elevation measurements carried out in the polder area. Alternatives in subsequent stages were determined based on the results of previous stages, as well as experiences from the 2010 flood and consultations with the Regional Water Management Board in Poznań. The performance of the alternatives was evaluated according to six criteria that described the effectiveness of the polder operation in terms of its practical use and effectiveness in reducing flood hazard. The results showed that our approach made it possible to identify an effective variant of polder operation. Additional calculations were also performed to determine the magnitude of flows for which flooding of the polder should be considered to reduce downstream flooding.

Keywords

Flood risk management, flood hazard management, polder operation, hydrodynamic modeling, optimization of polder operation.

Submitted 1 December 2021, revised 12 October 2022, accepted 14 November 2022

DOI: 10.26491/mhwm/156516

1. Introduction

In the aftermath of major floods in the 1990s and extreme flooding in Central Europe in 2002, it was realized that these phenomena pose a serious threat to the economic development and general livelihood of citizens of European Union (EU) countries (Müller 2013; Kienzler et al. 2015). It was also recognized that the lack of coherent legislative and policy actions at the EU level undermines effective flood management (Priest et al. 2016). The result of these considerations was the development and implementation of the so-called Floods Directive (Directive 2007/60/ec of the European Parliament and of the Council of 23 October 2007 on the assessment and management of flood risks). Essentially, the aim of the Floods Directive is to reduce flood risk and control the effects of flooding. Flood risk management, according to the directive, includes preliminary flood risk assessment, development of flood hazard and flood risk maps, and preparing flood risk management plans (Tiukalo et al. 2015; Nones 2017). The last includes investments and measures planned to prevent or, where possible, reduce flood risk (Hartmann, Spit 2016).

Flood control investments can simultaneously create conflicts of interest and paradoxically increase flood risk (Schultz 2008; Warner et al. 2018). Cutting floodplains off from the riverbed decreases retention capacity and increases the flood risk in downstream sections (Di Baldassarre et al. 2009; Kienzler et al. 2015). In addition, hydro-technical structures such as reservoirs or dikes can create an artificial sense of security (Di Baldassarre et al. 2009; Wiśniewski 2016), frequently resulting in management and development of behind-levee areas, with catastrophic consequences in the case of structural failures (Schultz 2008; Di Baldassarre et al. 2009; Kienzler et al. 2015). As indicated by Warner et al. (2018), an increase in the economic value of land in built-up areas protected by levees turns a flood risk situation from one of “high flood frequency and low consequences” to one of “low flood frequency and significant consequences.” Polders may be an example of such facilities. They are often created in the areas behind the levees, allowing agricultural use of the land. During flood wave propagation, they provide additional retention capacity through a system of hydraulic structures (Bouwer et al. 2009; Warner et al. 2018). As a result, the management of lands protected by dikes and flood protection facilities leads to changes in social structures, decision-making power, and trade-offs between when and how much water is extracted or discharged. Furthermore, flood risks are redistributed among stakeholders (Warner et al. 2018).

The redistributed flood risk applies to many areas worldwide (e.g., Huang et al. 2007; Ungvári, Kis 2021), including the Warta River Valley from Konin to Ślęgocin (Wielkopolska region, Western Poland). Until the 1980s, the Warta River Valley was characterized by un-embanked floodplains, protecting the downstream areas against floods, e.g., the city of Poznań, the fifth most populous city in Poland. The situation changed with the construction of the Jeziorsko Reservoir, which was officially commissioned in 1986. The investment resulted in additional flood protection plans for drained agricultural areas along the Warta River in the Konin-Pyzderska Valley (Ilnicki et al. 1987). As a result, a significant river reach was embanked, limiting the natural retention of the valley and shifting the task of flood wave reduction to the Jeziorsko Reservoir. In the course of the reservoir’s operation, however, it turned out that when unfavorable factors occurred simultaneously, such as maintaining a normal water level in the reservoir in advance of a peak flood wave, the flood reserve of the reservoir is not sufficient to reduce the flood wave volume to the required extent. Consequently, a decision was taken to increase the retention capacity in the Warta River Valley, by building the Golina polder below the Jeziorsko Reservoir. The area of the polder was completely flooded during a high water event in 2010, exposing the negative effects of the illusory safety of the Golina polder and the lack of adequate facilities and procedures that would allow safe and optimal use of the structure. Conflicts of interest among local residents (who used sandbags to protect the polder and their properties from flooding), and the threat that controlled drainage of water from the polder could not be accomplished came to the fore. Following the flood of 2010, several initiatives were undertaken to improve the operation of the Golina polder. At the request of the Wielkopolska Voivode, the Regional Water Management Board in Poznań undertook efforts to transform the polder into a fully controllable flood control structure.

Controlled operation of polders provides a higher-value risk mitigation service per unit of land area, assuming it is technically feasible to open high-flow-through-capacity floodgates at the optimal hydrological moment to cut off and store the top of the flood wave that poses the greatest threat (Ungvári, Kis 2021). Hence, there is a distinct economic decision point warranting the opening of the floodgate only under a controlled inundation case. However, design, operation, and management of large flood protection facilities may be a difficult problem for decision-makers and structure operators (Fayaed et al. 2013). Therefore, hydrodynamic simulations and optimization algorithms have been highlighted in the scientific literature as auxiliary tools for these decisions (Huang et al. 2007; Fayaed et al. 2013; Dobson et al. 2019). Hydrodynamic modeling has been widely adopted in practice in EU countries, for example, as a result of implementing the Floods Directive (Myronidis et al. 2009, Tsakiris 2014; Nones 2017). For polder systems, 2D hydrodynamic modeling was used, for instance, to analyze the effectiveness of capping the peak discharge of an extreme flood event in the Elbe River in Germany (Huang et al. 2007). In contrast to hydrodynamic modeling, case studies of the application of optimization algorithms to polder operations are few. Optimization refers to a mathematical formulation in which an algorithm is used to compute a set of decision variable values that minimize or maximize an objective function subject to constraints (Fayaed et al. 2013; Dobson et al. 2019). There are many optimization methods, which include implicit and explicit stochastic optimization (e.g., linear programming, stochastic dynamic programming), computational intelligence (e.g., fuzzy set theory, artificial neural networks), multiobjective optimization, and simulation-optimization techniques (Ko et al. 1992; Le Ngo et al. 2007; Rani, Moreira 2010; Fayaed et al. 2013). Nevertheless, complicated mathematical algorithms are difficult to apply in practice and thus, hydrodynamic simulation methods remain the strategic instrument for planning and management of flood protection system studies. Additionally, most of the mathematical optimization algorithms so far have been applied to analyses of reservoir operations (e.g., Le Ngo et al. 2007; Bashiri-Atrabi et al. 2015; Côté, Leconte 2016; Lai et al. 2021). One of the few examples of polder operation optimization involves fuzzy set rules and their application in multi-criteria decision-making to develop a flood retention plan (Schumann, Nijssen 2010).

The aim of our study was to design an effective operational alternative for the Golina polder to reduce flood hazard in the Warta River Valley. Considering the difficulties associated with the practical application of advanced optimization methods, we implemented a trial-and-error approach to the development of computational variants. Our approach was based on 1D/2D hydrodynamic modeling and staged analyses of alternatives, which evaluated differing locations and parameters of the inlet and outlet control structures. Various control scenarios for flooding and draining the polder were also considered. The approach as implemented has proven to be effective, thus, our simplified trial-and-error staged variant analyses may be a valuable clue for practitioners. The basis for building the computational variants was our practical experience and evidence gathered during the polder flooding in 2010. For this reason, this paper also presents detailed information about the flood event in the Warta River Valley from Konin to Slugocin in 2010. This information and evidence gave a broader context to our study and may be

valuable to other researchers in future analyses. The results of our calculations were the basis for developing documentation for the Regional Water Management Board in Poznań, indicating the means for effective polder operation and the scope of hydro-technical investments required.

2. Study area and the 2010 flood event

The Golina polder is located on the right bank of the Warta River below the town of Konin (Fig. 1). The area of the Warta River Valley from Konin to Slugocin is a part of the mesoregion of the Konin Valley and a part of the Warsaw-Berlin Proglacial Valley. In the northern part, the edges of the valley form distinct escarpments, while the southern ones are much gentler. The valley is relatively wide, 4-6 km, filled with sandy loam, medium loam, and hydromorphic soils, in which strong fluvial processes have created varied relief (Ilnicki et al. 1987). The existing Golina polder is limited on the east by a permanent concrete overflow, on the south by the right-bank levee of the Warta River, on the west by the A2 highway embankment (Poznan-Warsaw) and on the north by the high bank of the Konin-Pyzderska Valley (Fig. 2). The land constituting the Golina polder area is located within the administrative borders of three communes: Golina, Rzgów, and Stare Miasto. The Golina polder area is about 2900 ha. On the section of the Warta River analyzed there are flood embankments that narrow the natural floodplains. The smallest width between the embankments near the Slawsk water gauge is ~350 m. The main riverbed in the section analyzed is ~50 m wide, and the length of the river along the Golina polder is 11.5 km. The water gauge station Slawsk is located on the left bank of the Warta River. In the water gauge cross-section, the depth is ~2 m at bankfull stage.

Current, uncontrolled utilization of the Golina polder is possible because of the following hydro-technical structures:

- lower levee spillway in Osieczka - concrete spillway, 200 m long with the elevation of the crest 80.30 m a.s.l.;
- weir in Radolina - with gates 3×4.0 m;
- levee culvert in Radolina - with Ø 3×1.2 m;
- culvert in A2 highway embankment - Ø 2×1.6 m;
- culvert in A2 highway embankment on Struga Kawnicka – Ø 2×1.6 m;
- right and left levees of the Warta River.

Primarily, the inability to control the water flow through the polder led to the danger of catastrophe during the flood event in 2010. On 22nd May 2010, i.e., four days before the flood peak, the water surface elevation at the Warta River reached the level of the upper levee spillway. During the first hours, the flow of water into the polder was prevented by sandbags placed on the crest of the levee spillway by local residents. As a result, excessive water was dammed up above the structure and significant water infiltration through the embankment led to sliding of the slabs forming the top layer of the spillway. The resulting breach reached a width of about 15 m (after the flood wave culmination it was about 16 m). In the following hours, the water level increased systematically in the Warta River, which caused the sandbags

placed in several other places to be washed away. Sandbags were also placed on the lower levee spillway. Although the ordinates of the water level during the peak exceeded the ordinate of the spillway crest, they prevented the inflow of water to the polder.

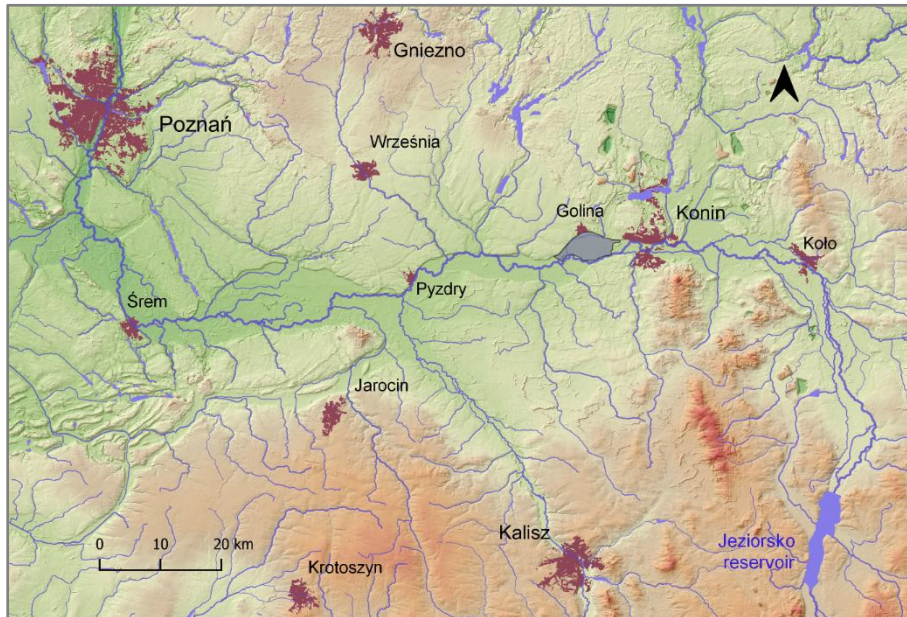


Fig. 1. Location of the Konin-Pyzderska Valley in the middle section of the Warta River.

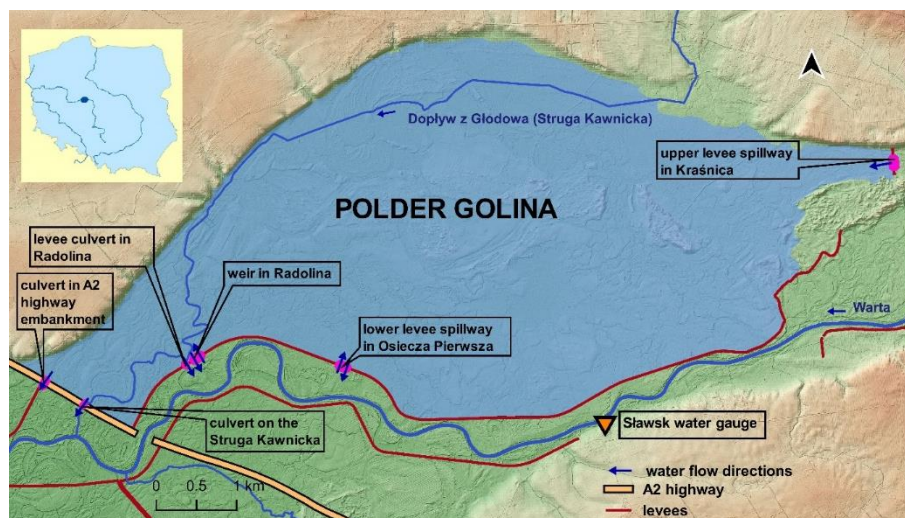


Fig. 2. Location of existing hydro-technical facilities in the Golina polder and assumed possibility of water exchange between the polder and the Warta riverbed.

When water started to flow into the polder area through the upper levee spillway, the weir in Radolina remained closed. Therefore, on 27th May, a day after the peak, the water levels on the polder side and in the Warta riverbed equalized. This situation caused weir gates to be raised, allowing water to flow away from the polder area. However, under these conditions the capacity of the structure was insufficient. Additionally, at the weir, the water surface elevation on the riverside was close to the water level in the polder, which also impeded water outflow. In the following days, the water surface elevations in the

polder began to exceed the water level in the riverbed. The complete opening of the weir did not help, because water was still flowing into the polder in an uncontrolled way through the breach near the upper levee spillway. As a result, the A2 highway was in danger of being closed; although its embankment limits the polder from the west, it is not adapted to serve as a levee. Therefore, it was decided to drain the water from the polder by an additional breach in the levee. The work started on 29th June about 300 m above the A2 highway embankment. The width of the crosscut was ~25 m. The water level in the polder started to decrease, and on 3 June the weir was closed to prevent inflow from the river. Further, on 7 June, a closing ring was constructed in the location of the damaged upper levee spillway (Fig. 3).

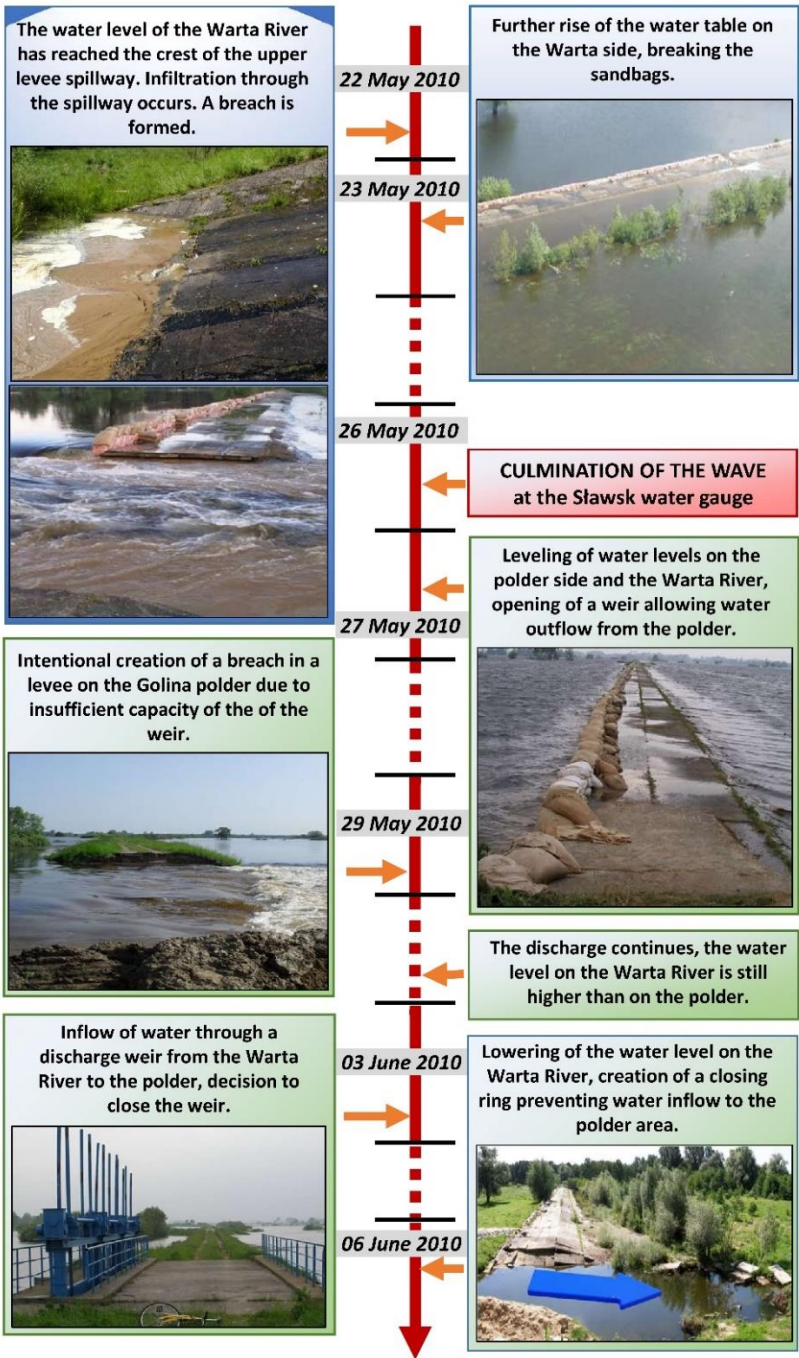


Fig. 3. Course of flooding in the Golina polder in 2010.

3. Materials and methods

3.1. Hydrodynamic models

Variants leading to an effective scenario for Golina polder operation were calculated by coupled 1D/2D hydrodynamic model. The model consisted of a one-dimensional section (1D, developed in MIKE11 software), which included the embanked Warta River Valley from km 369+500 to km 400+000, and a two-dimensional section (2D, developed in MIKE 21 software) of the Golina polder (Fig. 4). The basic input data for modeling were topographic data. A digital elevation model (DEM) with a grid size of 1 m, acquired through laser scanning technology (LIDAR), was used as source data for topographic relief of the floodplains. Measured cross-sections of the riverbed were used to represent the channel bathymetry. In the 1D part of the model, valley cross sections (combinations of channel cross sections and cross sections through the floodplains) were implemented. In the 2D part, a generalized DEM was used. The generalization procedure was performed using the nearest neighbor method, creating a grid with 1.4 million cells, each 8×8 m. The processed DEM was also updated with measured elevations of the levees. Subsequently, Manning's roughness coefficients were defined, with preliminary values based on Ven Te Chow's tables (Chow 1959). The data used were topographic maps at the scale of 1:10000, orthophoto maps, Corine Land Cover, and information and photographs from the field inspection. It was assumed that the area below the designed weirs was not overgrown with bushes that could hinder the polder inflow. The values of roughness coefficients ranged from 0.025-0.12 [s/m^{1/3}]. In the 1D part, the values were assigned to cross sections, while in the 2D part roughness coefficients were implemented as a grid file (Fig. 5). Existing hydro-technical structures were also implemented into the model.

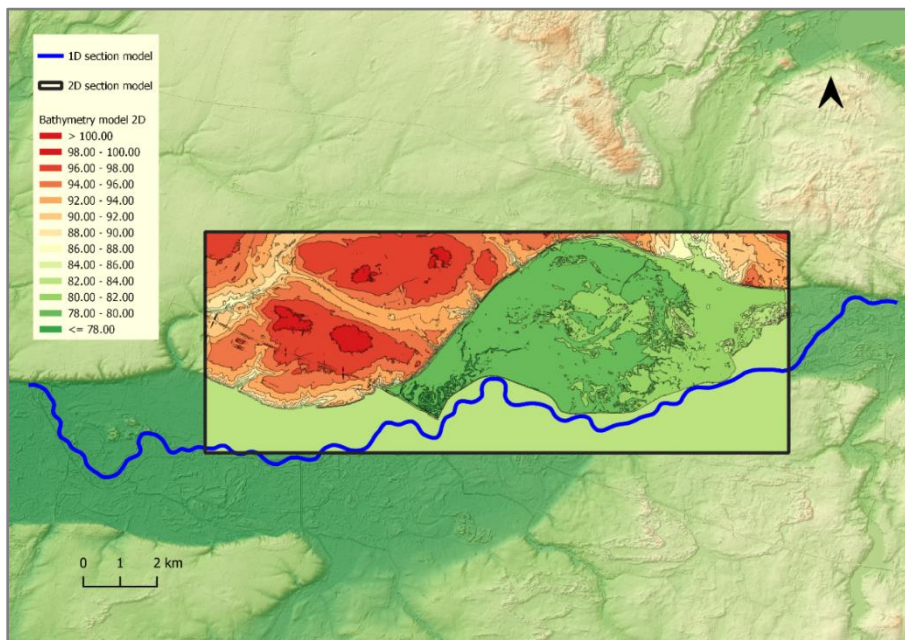


Fig. 4. The computational domain of the coupled 1D/2D hydrodynamic model of the analyzed Warta River section and Golina polder.

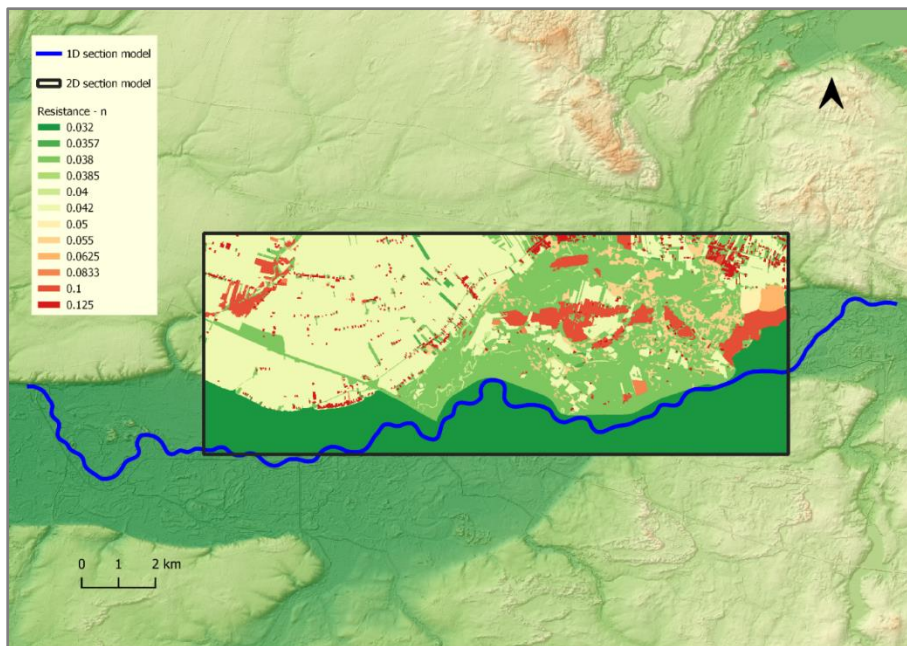


Fig. 5. The grid presenting Manning roughness coefficient variability within the 2D hydrodynamic model.

The 1D and 2D models were connected using the MIKE FLOOD module, by standard link connections (DHI 2011b). In the case analyzed, this connection consisted in assigning the first or last computational cross-section in the 1D model to the appropriate computational cells in the 2D model, so it was used on both the inflow and outflow from the 2D model area at sites of hydro-technical structures. The water exchange was simulated by draining the flow at the lower boundary condition of the 1D model and feeding it to selected computational cells of the 2D model. The water exchange could also be modeled by draining water from selected computational cells of the 2D model, in place of the upper boundary condition of the 1D model, or the opposite (DHI 2011a). Furthermore, using the Dam Break module in the 1D model (DHI 2011a), for calibration purposes breaches were defined based on evidence and measurements obtained during the 2010 flood. The breaches were defined at the location of the upper levee spillway and close to the A2 highway, in the location of the excavated levee crosscut. The model was calibrated based on data from the 2010 flood event. Several types of data were employed for the process of calibration: measurements of water level in the polder area during the flood, information about the operation of hydro-technical structures and levee crosscut (information from Voivodship Authority of Land Reclamation and Water Structures – WZMiUW, and field observations), and observed hydrological data at the water gauge Slawsk. The parameters of the breach, such as the width, depth, and time of the breach formation were predefined based on the measured data (during and after the flood) and information obtained from the WZMiUW. Parameters that were optimized were roughness coefficients and parameters of the breach of the upper levee spillway. The aim was to obtain the smallest possible differences between calculated and observed flow and water surface elevation hydrographs in the Warta River, and between calculated and observed water surface elevations in the polder. To assess the calibration performance for the water gauge data, the following parameters were determined (Książek

2010): coefficient of determination (R^2), absolute and percentage error of water surface elevation at the peak of the flood wave (ΔH_{max} , $\% \Delta H_{max}$), absolute and percentage error of flow at the peak of the flood wave (ΔQ_{max} , $\% \Delta Q_{max}$), and root mean square error ($RMSE$). Parameters used for assessment of the calibration performance at the Golina polder included coefficient of determination and absolute and percentage error of water surface elevation at the peak of the flood wave. Because the Golina polder was completely flooded only once, in 2010, no additional data were available for model verification. For this reason, model verification was not performed.

3.2. Calculation variants

The calibrated model was used for calculations of variants aimed at determining the most effective scenario for reducing flood hazard by controlled polder operation. The alternatives analyzed accounted for the different locations of hydro-technical structures at the inlet and outlet of the polder, their parameters, and the complexity of the operating rules. The most effective variant was understood as the one which provided the greatest reduction of maximum flow on the Warta River below the Golina polder, while taking advantage of the polder's retention capacity, the possibility of effective water supply and discharge from the polder area, and the feasibility of practical implementation of the variant (due to costs and complexity of operating rules). First, the calculations were carried out for the variant "0" (W0), which assumed no possibility of flooding the Golina polder through inlet and outlet structures and overtopping the levees. Subsequent calculation variants were tested in stages using a trial-and-error approach. In the first stage, the methods of flooding the polder were varied, while in the second stage, to increase the efficiency of the polder operation, different parameters and locations of new structures were tested. In the third stage, the final scenario of polder operation was selected and tested. Alternatives in subsequent stages were determined based on the results of previous stages, as well as experiences from the 2010 flood and consultations with the Regional Water Management Board in Poznań.

The efficiency of the analyzed polder operation variants was qualitatively assessed using the following criteria:

K1 – flooded area of the polder;

K2 – duration of water presence in the polder;

K3 – the maximum volume of water in the polder;

K4 – the maximum water level in the Golina polder close to the A2 highway;

K5 – the maximum water surface elevation and percentage reduction of maximum flow (relative to variant W0) in the control cross-section located on the Warta River, downstream of the A2 highway;

K6 – the possibility of practical implementation of the variant (based on expert evaluation of cost-effectiveness and complexity of operating rules).

Explanation and justification of the adopted criteria were presented in Table 1. For each variant, points were assigned to the listed criteria. Points were given on a scale from 1 (the worst variant with respect to a given criterion) to 7 (the best variant with respect to a given criterion). Points were allocated based on

modeling results (criteria K1-K5) and expert assessment in the case of criterion K6. If the simulation results for a given criterion were the same for several alternatives, they received the same number of points. The final assessment results were obtained by a weighted sum (K) of the assigned points, using the following formula:

$$K = 0.2 (0.33K1 + 0.33K2 + 0.33K3) + 0.3K4 + 0.3K5 + 0.2K6 \quad (1)$$

The adopted weights for particular criteria were related to the significance of the reduction of flood hazard. Thus, the criteria K4 and K5, which referred to the maximum water level on the Warta River and the Golina polder close to the A2 highway, received a weight of 0.3. Other criteria were also important, hence, the sum of points for criteria related to the effectiveness of polder utilization and the feasibility of practical implementation of the variant each received the weight 0.2. The weights were assumed based on our practical experience in flood hazard management and cooperation with regional water authorities. Additionally, the polder effectiveness criteria were combined to avoid problems associated with overestimating the importance of these criteria among the others.

Table 1. Description of the criteria adopted to evaluate the analyzed polder operation alternatives.

Criterion	Detailed description	Justification
K1	The criterion comparing alternatives for use of the Golina polder area. The larger the flooded area the better.	The flooded area indicates the effectiveness of using the available retention capacity of the polder.
K2	The criterion comparing alternatives for the duration of water presence in the polder. The shorter the duration of water in the polder the better.	During the 2010 flood event, one of the problems with polder operation was drainage after the flood wave culmination. This problem was caused by insufficient capacity of outlet hydro-technical facilities, leading to water surface elevations in the polder exceeding the water level in the riverbed.
K3	Criterion comparing alternatives for use of the Golina polder retention capacity. The larger the volume of water the better.	Similarly to the flooded area, the volume of water indicates the efficiency of using the available retention capacity of the polder.
K4	A criterion comparing variants of the maximum water level in the Golina polder close to the A2 highway. The lower the maximum water level the better.	During the 2010 flood event, high water in the Golina polder posed a danger for use of the A2 highway. Thus, this criterion also balances the scores obtained from criteria K1 and K2.
K5	A criterion comparing variants for effectiveness in lowering the flood wave peak on the Warta River. The lower the maximum water level and the bigger reduction of the flood peak the better.	The most important criterion that is indirectly related to decreasing the flood hazard in the areas located downstream.
K6	A criterion comparing variants for the feasibility of implementation; assessment was based on expert evaluation of cost-effectiveness and complexity of operating rules.	Assuming very precise and complicated rules resulting from the modeling and considering them as suitable for implementation during a flood could lead to a real decrease in the effectiveness of polder operation. In addition, planning very large structures would not be economically viable due to cost.

In the modeling studies of operational variants, a hypothetical flood peak with maximum flow probability of exceedance $p = 1\%$ was used as the upper boundary condition. Once the effective variant was selected, additional calculations were performed to determine the flow values for which polder flooding should be considered to lower the flood wave culmination. In these simulations, hypothetical waves with maximum

flows for the following probabilities of exceedance: $p = 10\%$, $p = 2\%$, $p = 1\%$, $p = 0.5\%$, and $p = 0.2\%$ were used as upper boundary conditions. The applied hypothetical waves were determined by the Institute of Meteorology and Water Management (IMGW-PIB) based on maximum annual flows, using the maximum reliability method for the 60-year observation period (1951-2010) at the Slawsk water gauge station.

4. Results and discussion

4.1. Calibration

Based on hydrological observations at the Slawsk water gauge, hydrographs of the water surface elevations and flows were developed. These hydrographs were compared graphically with hydrographs obtained from the calibrated mathematical model (Fig. 6, 7). The coefficient of determination between the hydrographs for flow and water elevations was $R^2 = 0.99$ (Table 2). The maximum water surface elevations at the peak of the flood wave, obtained from the model calculations and observations, were very similar (the difference was 2 cm). For maximum flows, the difference was 1.47 m³/s (0.36%). The *RMSE* errors for differences in water level and flow rate during calibration were 0.08 m and 11.01 m³/s, respectively. The *RMSE* value for the flow appears to be high, but given the flow hydrograph for the 2010 flood, it was only 2.70% of the peak flow value. For the polder area, calibration results also indicated good model performance. The coefficient of determination between modeled and measured data was 0.99 (Table 2). The difference in maximum water surface elevations at the peak of the flood wave was 2 cm.

Table 2. Summary of calibration results for the water gauge Slawsk.

No.	Assessment parameter	Water surface elevation	Discharge
WATER GAUGE SŁAWSK			
1.	Coefficient of determination, R^2	0.99	0.99
2.	Water surface elevation absolute error at the peak of the flood wave (ΔH_{max})	2 cm	-
	Water surface elevation percentage error at the peak of the flood wave ($\% \Delta H_{max}$)	0.35%	
	Calculated maximum water surface elevation	81.48 m a.s.l.	
	Observed maximum water surface elevation	81.46 m a.s.l.	
3.	Flow absolute error at the peak of the flood wave (ΔQ_{max})	-	1.47 m ³ /s
	Flow percentage error at the peak of the flood wave ($\% \Delta Q_{max}$)		0.36%
	Maximum calculated flow		405.91 m ³ /s
	Maximum observed flow		407.38 m ³ /s
4.	Root mean square error (<i>RMSE</i>)	8 cm	11.01 m ³ /s
GOLINA POLDER			
1.	Coefficient of determination, R^2	0.99	-
2.	Water surface elevation absolute error at the peak of the flood wave (ΔH_{max})	2 cm	-
	Water surface elevation percentage error at the peak of the flood wave ($\% \Delta H_{max}$)	0.95%	-
	Calculated maximum water surface elevation	80.13 m a.s.l.	-
	Observed maximum water surface elevation	80.11 m a.s.l.	-

The differences obtained during the calibration between the observed and calculated values were compared with literature data, which indicated that these errors are not significantly different from the results obtained by other authors for hydrodynamic models (e.g., Pasternack et al. 2004; Wright et al. 2017; Gao et al. 2018). Examples from the literature show that during calibration, *RMSE* errors for water surface elevations were less than 0.10 m. For instance, in the publication by Anderson et al. (2006) the *RMSE* error for the water surface elevations was 0.04 m. For polder analyses, Gao et al. (2018) obtained values of $R^2 = 0.981$ and absolute error of water level = 0.07 m. In addition, the values of other parameters used to evaluate model performance indicate a very good fit between model data and observed data, in accordance with national guidelines for calibration of hydrodynamic models for flood hazard mapping (KZGW 2020).

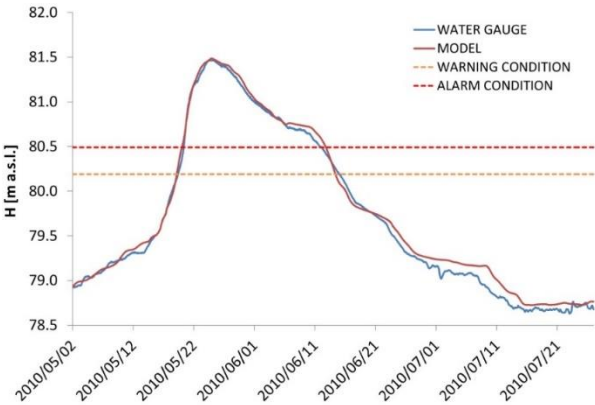


Fig. 6. Calibration results – comparison between calculated and observed hydrographs of water surface elevations for the water gauge Slawsk.

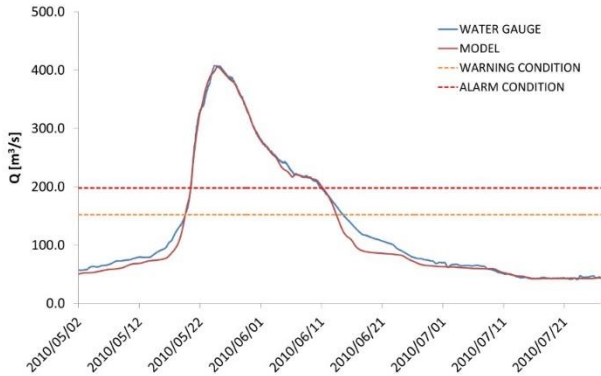


Fig. 7. Calibration results – comparison between calculated and observed hydrographs of flows for the water gauge Slawsk.

4.2. Calculation variants

The initial assumptions for defining effective operational variants of the Golina polder included the new upper weir in place of the upper levee spillway in Kraśnica (4×5.0 m), the new lower weir in place of the lower levee spillway in Osieczka (4×5.0 m), and the existing weir in Radolina. In the first three variants, alternative processes of polder flooding were considered: only through the upper weir (W1), only through

the lower weir (W2), and through the upper and lower weir (W3). In all three variants the possibility of emptying the polder through the weir in Radolina was assumed (Fig. 8). Moreover, for each variant, many methods of controlling the times of opening and closing of the weirs were tested.

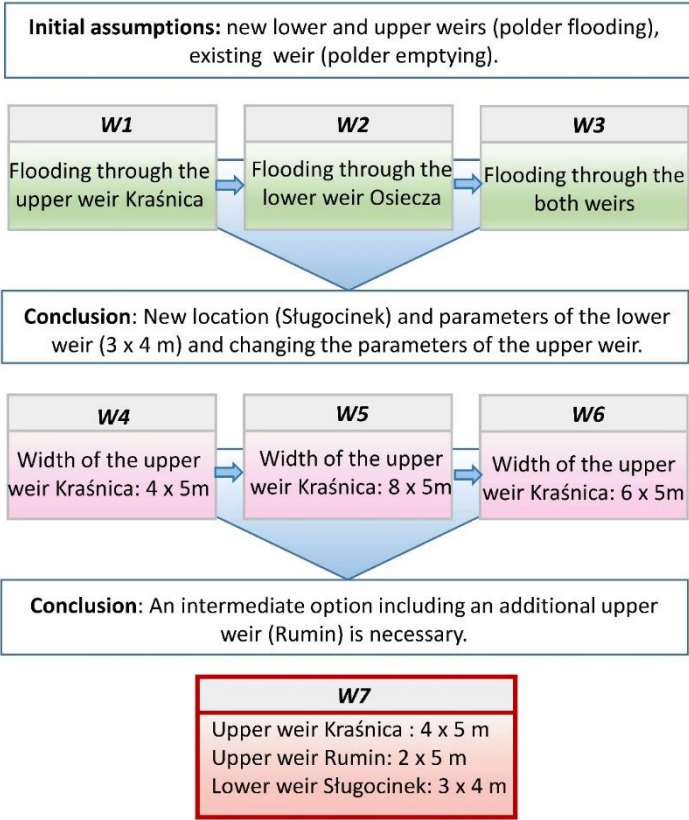


Fig. 8. Description of the hydro-technical structures and their parameters in modeled variants.

The results for variant W1 showed that the adopted weir size (4×5.0 m) was not sufficient for effective reduction of the flood wave in the Warta River – the least reduction of water level at control cross-sections and the least flow reduction was obtained (Table 3). Flooding of the polder through a weir at the lower levee spillway (W2) also did not allow for full utilization of polder capacity, as the maximum water level in the polder depended on the level of the water level in the Warta River. Additionally, the reduction of the maximum flow was highly dependent on detailed weir operation based on the water level in the Warta River. Yet, despite precise control of the structures (which is very difficult in flood conditions) the full capacity of the polder was not reached. Therefore, additional calculations were necessary to consider the increase in the structures’ throughput. In comparison to variants W1 and W2, by utilization of both inlet weirs (W3), a greater reduction of flood peak in the Warta River and effective use of the polder retention capacity were obtained. However, because of the complicated way of controlling the lower weir (similar to W2), that solution could be difficult to apply in practice. It should also be noted that flooding the polder through both weirs was possible until the water levels in the Warta River and the polder equalized at the location of the lower weir. To flood the polder to the assumed water surface elevations, it was necessary to close the lower weir in Osiecza and to continue flooding only through the upper weir in Kraśnica.

Table 3. Summary of selected results for the variants analyzed.

Tested variants	Flooded area in the Golina polder	Duration of water presence in the polder	Maximum water level in the Golina polder (next to the A2 highway)	Maximum volume of water in the Golina polder	Maximum water level in the control cross section below the A2 highway	Maximum flow in the control cross section below the A2 highway	Reduction of the peak flow	Assessment of the variants*						
								K1	K2	K3	K4	K5	K6	Weighted sum K
	[ha]	[hours]	[m a.s.l.]	[10 ⁶ m ³]	[m a.s.l.]	[m ³ /s]	[%]	-	-	-	-	-	-	-
W0	-	-	-	-	80	522	-	-	-	-	-	-	-	-
W1	2098	1525	80.12	16.57	79.84	466	11.06	1	2	1	1	1	3	1.466
W2	2204	1549	80.39	21.75	79.8	454	13.36	2	1	2	2	2	2	1.933
W3	2677	1549	80.87	33.41	79.73	430	17.94	4	1	3	5	6	1	4.033
W4	2098	1486	80.12	16.57	79.84	466	11.06	1	6	1	1	1	6	2.333
W5	2865	1512	81.63	52.98	79.74	433	17.36	6	3	5	4	4	4	4.132
W6	2717	1501	81.02	36.4	79.78	446	14.88	5	4	4	3	3	5	3.666
W7	2661	1500	80.87	33.41	79.73	431	17.74	3	5	3	5	5	5	4.733

* Criteria for the assessment of variants: K1 – flooded area of the polder; K2 – duration of water presence in the polder; K3 – the maximum volume of water in the polder; K4 – the maximum water level in the Golina polder close to the A2 highway; K5 – the maximum water surface elevation and percentage reduction of maximum flow in control cross-section located on the Warta River, downstream of A2 highway; K6 – the possibility of practical implementation of the variant.

Based on the results for variants W1-W3, it appeared that with a different location of the outlet weir (closer to the A2 highway embankment) it would be possible to start the discharge of water from the polder to the Warta River earlier (less time needed to empty the polder with higher discharge capacity of the weir). Therefore, removal of the existing weir in Radolina and the construction of a new outlet weir at the levee crosscut in 2010 (Slugocinek) was proposed. The location of the new outlet weir and the dimensions of the structure (3×4.0 m) were verified in variants W4-W6 (Fig. 8). Additional assumptions included the new upper (inlet) weir in place of the upper levee spillway in Kraśnica. The variants did not account for the operation of the existing lower levee spillway in Osieczka and the existing outlet weir in Radolina. In subsequent variants, different inlet weir dimensions were tested: 4×5.0 m (W4), 8×5.0 m (W5), and 6×5.0 m (W6). Increasing the number and size of the gates of the inlet weir in Kraśnica had a significant impact on the maximum discharge in the polder and the use of its retention capacity. These parameters also reduced the maximum flows in the Warta River. The greatest reduction of the flood wave peak was in variant W5. However, this result was connected with the need to build a large, eight-span weir and to flood the polder to the maximum water level. Moreover, the additional retention volume was almost the same as in variant W6. Therefore, further calculations were performed to identify an alternative solution. The location of an additional weir in Rumin was proposed. The purpose of the structure was to reduce the number of spans at the weir in Kraśnica, to lower the flood wave peak in the Warta River (similar to that obtained in variant W5), and to allow a smaller retention volume of the polder. These assumptions were defined and verified by conducting model calculations for the next variant, W7. The following inlet and outlet hydro-technical structures were tested: the new inlet weir in Kraśnica (4×5.0 m), the new inlet weir in Rumin (2×5.0 m), and the new outlet weir in Slugocinek (3×4.0 m). Similarly, as in variants W4-W6, the existing lower levee spillway in Osieczka and the existing outlet weir in Radolina were not considered. The results showed that W7 was the most effective of the cases tested (Table 3). A significant reduction of peak flood wave and lower water surface elevations in the polder was achieved (in comparison to W5). Furthermore, the weighted sum of the points assigned according to the assumed criteria for the evaluation of the variants indicates that W7 is the most effective compared to the other alternatives. The results for W7 in terms of flood hazard reduction and the criteria analyzed were also considered satisfactory by the Regional Water Management Board. Therefore, at this stage, the analyses of variants were terminated. The location of the proposed hydro-technical structures in the W7 variant is shown in Figure 9.

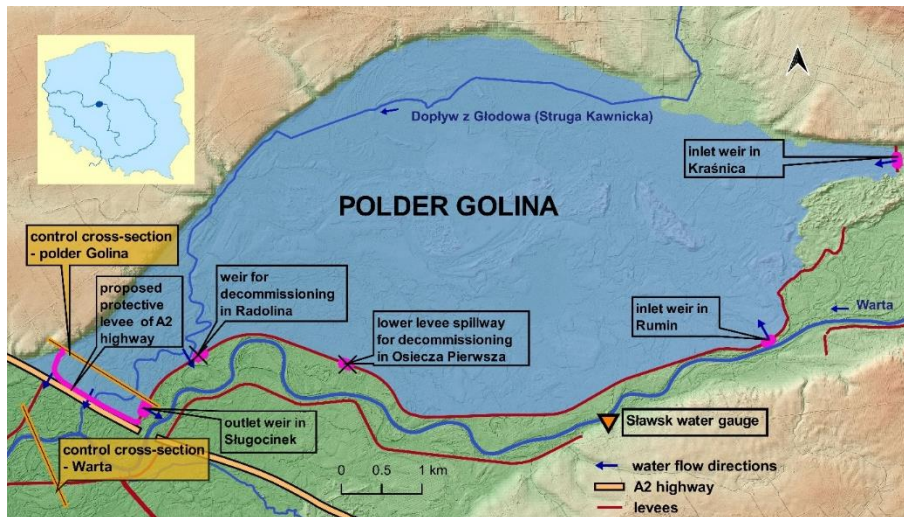


Fig. 9. Location of hydro-technical structures in the Golina polder in the most optimal variant (W7).

4.3. Additional computational scenarios for optimal variant W7

In designing the polder with full controllability, it was important to determine the flows for which inundation should be considered. Therefore, additional model calculations for variant W7 were carried out. The hypothetical flood waves with maximum flows for the following probabilities of exceedance were considered: 10%, 2%, 1%, 0.5%, and 0.2%. Selected results of model calculations are summarized in Table 4. The results indicated that for the wave with maximum flow probability of exceedance $p = 10\%$, the total capacity of the polder was not used. The calculated maximum water level in the polder was 80.11 m a.s.l. Therefore, effective utilization of the polder capacity is possible for flows greater than flows with a probability of exceedance $p = 10\%$. That means that statistically the polder should be flooded no more often than once every 10 years.

Table 4. Summary of selected results for additional flow scenarios for variant W7.

Flow in the Warta River with the probability of exceedance	Maximum water level in the Golina polder (next to the A2 highway)	Maximum water level in the control cross section below the A2 highway, without polder	Maximum water level in the control cross section below the A2 highway, with polder	Maximum flow in the control cross section below the A2 highway, without polder	Maximum flow in the control cross section below the A2 highway, with polder	Reduction of the peak flow
[%]	[m a.s.l.]	[m a.s.l.]	[m a.s.l.]	[m ³ /s]	[m ³ /s]	[%]
10.0%	80.11	79.46	79.25	342	292	14.62%
2.0%	80.64	79.85	79.61	469	390	16.84%
1.0%	80.87	80.00	79.73	522	431	17.43%
0.5%	81.04	80.12	79.84	572	469	18.01%
0.2%	81.04	80.30	79.99	638	521	18.34%

4.4. Summary

The 2010 flood in the Warta River Valley in the reach from Konin to Ślugocin showed how important it is to properly control the operation of the Golina polder. The existing arrangement of structures provided limited possibilities for controlling water inflow and outflow. Water flowed into the polder automatically when the water elevation exceeded the level of the crest of the levee overflows (the upper levee spillway in

Kraśnica and the lower one in Osieczka). Also, the discharge facilities (levee culverts and weir) did not ensure proper regulation of the timing and volume of water drained from the polder area. Inadequate management procedures, a faulty system of hydro-technical structures, and a lack of social consent to redirect flood risk led to increased flood risk and could cause catastrophic consequences. Therefore, it was necessary to find solutions that will prevent such problems in the future, and at the same time contribute to increasing the retention reserve, another element of flood protection in the Warta Valley downstream from the Jeziorsko Reservoir.

The data collected during the 2010 event flood were crucial for model calibration. First, the data reflected the operation of hydro-technical structures during the flood. Second, this process was extremely important for defining the hydraulic parameters of the model that was used to calculate variants. Simulation analyses supported many computations of flood wave propagation, which in the case of designing and establishing management principles for such large objects is certainly significant (Hesselink et al. 2003; Huang et al. 2007; Chatterjee et al. 2008; Gao et al. 2018). Finally, experience and data obtained during the 2010 flood were the basis for determining the modeled variants. Importantly, the Golina polder was completely flooded only once, which makes the data unique. In many cases, the lack of relevant information makes the analysis more complicated and uncertain. For instance, in the study of the Dutch polders (Netherlands), data from the 1805 inundation were used for model development, because there has not been another inundation event recently (since 1926). Further, in comparison to available data from the 1926 event, the evidence for the 1805 inundation included a detailed description of the dike breach and flooding, which enabled the reconstruction of topographical characteristics of the polder, water levels of the rivers Rhine and Meuse, and dike breach dimensions (Hesselink et al. 2003). Thus, information on the flood wave propagation presented in this paper may be valuable for other researchers in future analyses.

We have determined an effective variant for operation of the Golina polder, to reduce flood hazard in the Warta River Valley. Compared with other studies, we implemented a simpler trial-and-error approach in which we aimed to obtain effective polder performance with respect to six assessment criteria. The most effective variant was understood as the one which provided substantial reduction of maximum flow on the Warta River below the Golina polder, while taking advantage of the polder's retention capacity, the possibility of effective water supply and discharge from the polder area, and feasibility. Typically, in the scientific literature this type of analysis is performed during the process of optimizing the operation of flood protection structures (e.g., Le Ngo et al. 2007; Bashiri-Atrabi et al. 2015; Côté, Leconte 2016; Lai et al. 2021). The advantage of optimization is the identification of the most optimal variant in terms of the assumed objective functions. However, as Simonovic (1992) pointed out, the adaptation of new and complicated techniques and tools is slow, thus there is a gap between research and the application of the systems approach in practice. Therefore, our simplified approach can be an easy guideline for practitioners as to how the computational variants may be constructed, assessment criteria assumed, and historical data used effectively. In addition, our analyses allowed for considering criteria that were evaluated in an expert

manner, i.e., the feasibility of practical implementation of the variant. Assuming very precise and complicated rules resulting from the modeling and considering them as suitable for implementation during a flood could lead to a real decrease in the effectiveness of polder operation. The same consideration applied to the potential costs of implementing the variants, which were consulted with the Regional Water Management Board. In studies that consider the optimization process of hydro-technical structures (e.g., reservoirs), the definition of objective functions was more constrained. The objective functions considered decreasing the flood hazard in the terms of water surface elevations and flooded area (e.g., van Manen, Brinkhuis 2005; Le Ngo et al. 2007), damages, including their economic value (e.g., van Manen, Brinkhuis 2005; Bashiri-Atrabi et al. 2015; Ungvári, Kis 2021), assumed operating rules (e.g., Dobson et al. 2019), or demands on water resources by other users (e.g., Latif et al. 2021). Nevertheless, the approach presented in our paper is worth testing for other complex problems of operating hydro-technical structures operation.

In our study, we did not consider the social aspects of the polder operation and thus, the most effective variant does not solve the conflicts of interests and problems of the polder area inhabitants. Lack of social consent for flooding of the polder may therefore hinder proper use of the structures during floods. Therefore, future actions and analyses should also be directed towards land buyouts, legal sanctioning of farming in the polder area or implementation of other flood protection measures (e.g., additional embankments in the polder area, defining flooding rules to protect nearby residents, etc.). Only in this way, it will be possible to effectively reduce the flood hazard in the Warta River Valley between Konin and Slugocin. The social aspect was addressed, for example, in the study by Wei et al. (2022), in which the operation of the Baojixia reservoir was optimized. The irrigation needs of local residents and the water needs of other stakeholders were considered. When linking resident needs to modeling results, similar analyses could also be performed using the approach described in our study.

In closing, it is worth mentioning that to efficiently inundate the Golina polder, it will be also necessary to carry out actions aimed at facilitating water flow below the inlet weirs. First of all, shrubs and embankments of small local roads directly below the planned weirs should be eliminated. Further, information on forecasted water levels and flows at the water gauge profile in Sławsk and planned water discharges from the Jeziorsko Reservoir should be used for proper control of the inlet weirs. Building a levee to protect the A2 highway should also be an important additional measure. The water level in the polder in variant W7 was very close to the elevations of the highway embankment.

5. Conclusions

A trial-and-error approach implemented in our study to reduce flood hazard in the Warta River Valley, by designing effective operation of the Golina polder, led us to several conclusions. We summarize our key findings in the following points:

1. The data and experience obtained during the 2010 event flood were key to conducting the analyses in the study.

2. The calculations showed that the greatest reduction of the maximum flow in the Warta River below the Golina polder was obtained for variants W3, W5, and W7. However, the reduction in variant W3 was related to precise and complicated gate opening rules for the weirs, especially the lower weir in Osieczka, which had to be closed when the water level in the polder and in the Warta River equalized (to prevent water outflow from the polder area). The reduction of maximum flow rate in the Warta River in variant W5 was related to flooding the polder to the water level of 81.63 m a.s.l., which indicated the necessity of raising the levees. Thus, the most effective alternative analyzed was variant W7.
3. The location of the outlet weir closer to the A2 highway, near Ślugocinek, where the levee was breached during the flood in 2010, was more favorable compared to the location of the present weir in Radolina.
4. Effective use of the polder retention capacity occurred for flows higher than those with maximum probability of exceedance $p = 10\%$.
5. The duration of water storage in the polder in specific variants was similar and related to the rate of water decrease in the Warta River. However, emptying of the polder should occur as a result of gradual opening of the outlet weirs, within a few days after the peak of the flood wave. It will provide slow water inflow to the Warta River and will prevent creation of additional flood peaks.
6. The trial-and-error method, along with assumed criteria of variant performance, made it possible to indicate the most effective variant of polder operation. Therefore, our simplified approach can be an easy guideline for practitioners for how the computational variants may be constructed, assessment criteria assumed, and historical data used effectively.

Acknowledgments

Model tests were carried out under the study “Golina polder – stage II documentation” in part B – “Hydraulic modeling of the Golina polder with the use of 2D model”, commissioned by the Regional Water Management Board in Poznań and carried out by BIPROWODMEL Sp. z o.o. Biuro Projektów Wodnych Melioracji i Inżynierii Środowiska and Institute of Meteorology and Water Management – National Research Institute, Flood and Drought Modelling Centre in Poznań.

References

- Anderson K.E., Paul A.J., McCauley E., Jackson L.J., Post J.R., Nisbet R.M., 2006, Instream flow needs in streams and rivers: the importance of understanding ecological dynamics, *Frontiers in Ecology and the Environment*, 4 (6), 309-318, DOI: 10.1890/1540-9295(2006)4[309:IFNISA]2.0.CO;2.
- Bashiri-Atrabi H., Qaderi K., Rheinheimer D.E., Sharifi E., 2015, Application of harmony search algorithm to reservoir operation optimization, *Water Resources Management*, 29, 5729-5748, DOI: 10.1007/s11269-015-1143-3.
- Bouwer L.M., Bubeck P., Wagtenonk A.J., Aerts J.C.J.H., 2009, Inundation scenarios for flood damage evaluation in polder areas, *Natural Hazards and Earth System Sciences*, 9 (6), 1995-2007, DOI: 10.5194/nhess-9-1995-2009.
- Chatterjee C., Förster S., Bronstert A., 2008, Comparison of hydrodynamic models of different complexities to model floods with emergency storage areas, *Hydrological Processes*, 22 (24), 4695-4709, DOI: 10.1002/hyp.7079.
- Chow V.T., 1959, *Open-channel hydraulics*, McGraw-Hill, New York, 680 pp.

- Côté P., Leconte R., 2016, Comparison of stochastic optimization algorithms for hydropower reservoir operation with ensemble streamflow prediction, *Journal of Water Resources Planning and Management*, 142 (2), 04015046.
- Di Baldassarre G., Castellarin A., Brath B., 2009, Analysis of the effects of levee heightening on flood propagation: example of the River Po, Italy, *Hydrological Sciences Journal*, 54 (6), 1007-1017, 10.1623/hysj.54.6.1007.
- DHI 2011a, Reference Manual. A Modelling System for Rivers and Channels.
- DHI, 2011b, User Manual. Mike Flood, 1D-2D Modeling.
- Dobson B., Wagener T., Pianosi F., 2019, An argument-driven classification and comparison of reservoir operation optimization methods, *Advances in Water Resources*, 128, 74-86, DOI: 10.1016/j.advwatres.2019.04.012.
- Fayaed S.S., El-Shafie A., Jaafar O., 2013, Reservoir-system simulation and optimization techniques, *Stochastic Environmental Research and Risk Assessment*, 27, 1751-1772, DOI: 10.1007/s00477-013-0711-4.
- Gao Y., Yuan Y., Wang H., Zhang Z., Ye L., 2018, Analysis of impacts of polders on flood processes in Qinhuai River Basin, China, using the HEC-RAS model, *Water Supply*, 18 (5), 1852-1860, DOI: 10.2166/ws.2018.008.
- Hartman T., Spit T., 2016, Legitimizing differentiated flood protection levels – Consequences of the European flood risk management plan, *Environmental Science & Policy*, 55, 361-367, DOI: 10.1016/j.envsci.2015.08.013.
- Hesselink A.W., Stelling G.S., Kwadijk J.C., Middelkoop H., 2003, Inundation of a Dutch river polder, sensitivity analysis of a physically based inundation model using historic data, *Water Resources Research*, 39 (9), DOI: 10.1029/2002WR001334.
- Huang S., Rauberg J., Apel H., Disse M., Lindenschmidt K.-E., 2007, The effectiveness of polder systems on peak discharge capping of floods along the middle reaches of the Elbe River in Germany, *Hydrology and Earth System Sciences*, 11, 1391-1401, DOI: 10.5194/hess-11-1391-2007.
- Ilnicki P., Orłowski W., Machczyński J., Winięcki A., 1987, Koncepcja melioracji i zagospodarowania polderu III-Rataje oraz polderu IV-Wrąbczyn w aspekcie studium przyrodniczego doliny środkowej Warty, WZIR Technical Report.
- Kienzler S., Pech I., Kreibich H., Müller M., Thielen A.H., 2015, After the extreme flood in 2002: changes in preparedness, response and recovery of flood-affected residents in Germany between 2005 and 2011, *Natural Hazards and Earth System Sciences*, 15 (3), 505-526, DOI: 10.5194/nhess-15-505-2015.
- Ko S.-K., Fontane D.G., Labadie J.W., 1992, Multiobjective optimization of reservoir systems operation, *JAWRA Journal of the American Water Resources Association*, 28 (1), 111-127, DOI: 10.1111/j.1752-1688.1992.tb03158.x.
- Książek L., Wałęga A., Bartnik W., Krzanowski S., 2010, Kalibracja i weryfikacja modelu obliczeniowego rzeki Wisłok z wykorzystaniem transformacji fali wezbraniowej, *Infrastruktura i Ekologia Terenów Wiejskich*, 8 (1), 15-28.
- KZGW, 2020, Metodyka opracowania map zagrożenia powodziowego i map ryzyka powodziowego w II cyklu planistycznym.
- Lai V., Huang Y.F., Koo C.H., Ahmed A.N., El-Shafie A., 2021, Optimization of reservoir operation at Klang Gate Dam utilizing a whale optimization algorithm and a Lévy flight and distribution enhancement technique, *Engineering Applications of Computational Fluid Mechanics*, 15 (1), 1682-1702, DOI: 10.1080/19942060.2021.1982777.
- Latif S.D., Marhain S., Hossain M.S., Ahmed A.N., Sherif M., Sefelnasr A., El-Shafie A., 2021, Optimizing the operation release policy using charged system search algorithm: a case study of Klang Gates Dam, Malaysia, *Sustainability*, 13 (11), DOI: 10.3390/su13115900.
- Le Ngo L., Madsen H., Rosbjerg D., 2007, Simulation and optimisation modelling approach for operation of the Hoa Binh reservoir, Vietnam, *Journal of Hydrology*, 336 (3-4), 269-281, DOI: 10.1016/j.jhydrol.2007.01.003.
- Müller U., 2013, Implementation of the flood risk management directive in selected European countries, *International Journal of Disaster Risk Science*, 4, 115-125, DOI: 10.1007/s13753-013-0013-y.
- Myronidis D., Emmanouloudis D., Stathis D., Stefanidis P., 2009, Integrated flood hazard mapping in the framework of the E.U. directive on the assessment and management of flood risks, *Fresenius Environmental Bulletin*, 18 (1), 102-111.
- Nones M., 2017, Flood hazard maps in the European context, *Water International*, 42 (3), 324-334, DOI: 10.1080/02508060.2016.1269282.
- Pasternack G.B., Wang C.L. Merz J.E., 2004, Application of a 2D hydrodynamic model to design of reach-scale spawning gravel replenishment on the Mokelumne River, California, *River Research and Applications*, 20 (2), 205-225, DOI: 10.1002/rra.748.

- Priest S.J., Suykens C., Van Rijswick H.F.M.W., Schellenberger T., Goytia S., Kundzewicz Z.W., Van Doorn-Hoekveld W.J., Beyers J., Homewood S., 2016, The European Union approach to flood risk management and improving societal resilience: lessons from the implementation of the Floods Directive in six European countries, *Ecology and Society*, 21 (4), DOI: 10.5751/ES-08913-210450.
- Rani D., Moreira M.M., 2010, Simulation-optimization modeling: a survey and potential application in reservoir systems operation, *Water Resources Management*, 24, 1107-1138, DOI: 10.1007/s11269-009-9488-0.
- Schultz B., 2008, Water management and flood protection of the polders in the Netherlands under the impact of climate change and man-induced changes in land use, *Journal of Water and Land Development*, 12, 71-94, DOI: 10.2478/v10025-009-0007-8.
- Schumann A.H., Nijssen, D., 2011, Application of scenarios and multi-criteria decision making tools in flood polder planning, [in:] *Flood Risk Assessment and Management*, A. Schumann (eds), Springer, Dordrecht, DOI: 10.1007/978-90-481-9917-4_12.
- Simonovic, S.P., 1992, Reservoir systems analysis: closing gap between theory and practice, *Journal of Water Resources Planning and Management*, 118 (3), 262-280, DOI: 10.1061/(ASCE)0733-9496(1992)118:3(262).
- Tiukalo A., Malinger A., Orczykowski T., Pasiok R., Bedryj M., Wawrzyniak M., Dysarz T., Grzelka T., Krawczak E., 2015, Ocena ryzyka powodziowego na potrzeby planów zarządzania ryzykiem powodziowym, *Gospodarka Wodna*, 3, 79-85.
- Tsakiris G., 2014, Flood risk assessment: concepts, modelling, applications, *Natural Hazards and Earth System Sciences*, 14 (5), 1361-1369, DOI: 10.5194/nhess-14-1361-2014.
- Ungvári B., Kis A., 2021, Reducing flood risk by effective use of flood-peak polders: A case study of the Tisza River, *Journal of Flood Risk Management*, 15 (3), DOI: 10.1111/jfr3.12823.
- van Manen S.E., Brinkhuis M., 2005, Quantitative flood risk assessment for Polders, *Reliability Engineering & System Safety*, 90 (2-3), 229-237, DOI: 10.1016/j.res.2004.10.002.
- Warner J.F., van Staveren M.F., van Tatenhove J., 2018, Cutting dikes, cutting ties? Reintroducing flood dynamics in coastal polders in Bangladesh and the Netherlands, *International Journal of Disaster Risk Reduction*, 32, 106-112, DOI: 10.1016/j.ijdrr.2018.03.020.
- Wei N., He S., Lu K., Xie J., Peng Y., 2022, Multi-stakeholder coordinated operation of reservoir considering irrigation and ecology, *Water* 14, (12), DOI: 10.3390/w14121970.
- Wiśniewski J., 2016, Dlaczego powinniśmy zbudować polder Golina na Warcie?, *Gospodarka Wodna*, 1, 25-32.
- Wright K.A., Goodman D.H., Som N.A., Alvarez J., Martin A., Hardy T.B., 2017, Improving hydrodynamic modelling: an analytical framework for assessment of two-dimensional hydrodynamic models, *River Research and Applications*, 33 (1), 170-181, DOI: 10.1002/rra.3067.

Comprehensive evaluation of trend analysis of extreme drought events in the Ceyhan River Basin, Turkey

Musa Esit

Adiyaman University, Turkey

Mehmet Ishak Yuce 

Gaziantep University, Turkey

Abstract

The investigation of extreme meteorological drought events is crucial for disaster preparedness and regional water management. In this study, trends in extreme drought events, namely annual maximum drought severity (AMDS) and annual maximum drought duration (AMDD), were examined for the Ceyhan Basin. The analyses of extreme events were conducted using the standard precipitation index (SPI) index for multiple-time scales of 1, 3, 6, 9, and 12 months for 23 meteorological stations located in the Ceyhan Basin, Turkey. The Wallis-Moore and Wald-Wolfowitz methods were employed to determine the homogeneity of the data sets, whereas trend analyses were conducted using Mann-Kendall and Spearman Rho tests. The magnitude of trends was defined by Sen's slope and linear regression, and change points were detected using the standard normal homogeneity test, Buishand's range test, and Pettitt's test. Although increasing trends were detected in most of the stations, only in nine of them, statistically significant results were noted at a significance level of 95%. The results of this paper provide valuable information to water resource management decision-makers in the Ceyhan River Basin for evaluating the effect of droughts and preparing for drought mitigation measures to avoid future drought risks.

Keywords

Climate change, drought severity, drought duration, trend, Ceyhan Basin.

Submitted 16 February 2022, revised 27 June 2022, accepted 15 September 2022

DOI: 10.26491/mhwm/154573

1. Introduction

Droughts are recurrent natural disasters characterized by a significant rainfall deficit, leading to water scarcity, streamflow depletion, crop damage, and groundwater reduction. They can be classified as meteorological, hydrological, agricultural, and socio-economic droughts (Dracup et al. 1980; Wilhite, Glantz 1985). Various parameters must be considered when defining the temporal and spatial scales and the regional characteristics of droughts (Tallaksen, Lanen 2004). More than 130 published drought definitions can be categorized in several ways, as noted by Wilhite and Glantz (1985). Some of the most commonly used definitions of droughts have been listed by Tate and Gustard (2000) and Demuth and Bakenhus (1994). Droughts have negative impacts on social life, the economy, and the environment, although these impacts are difficult to detect. Several indices have been developed to identify and analyze droughts, of which the most commonly used one is the standard precipitation index (SPI) (McKee et al. 1993; Ganguli, Reddy 2014). Other indices, such as the Palmer drought severity index (PDSI) (Palmer 1965), the surface water supply index (SWSI) (Shafer, Dezman 1982), and the crop moisture index (CMI) (Palmer 1968), are also widely applied to detect drought events.

Several drought trend studies have been conducted all over the world (Piccarreta et al. 2004; Xu et al. 2011), and the hydrological time series of precipitation, temperature, soil moisture, and evapotranspiration at the catchment scale have been widely investigated (Villarini et al. 2009; Burn et al. 2010; Gocic, Trajkovic 2013; Zhang et al. 2015). As a consequence of global warming and climate change, water resources, the environment, agricultural activities, and industrial production have been significantly affected (Shi, Xu 2008). However, the detection of changes in climate and hydrological time series is complex and challenging but has become an important issue because of the role of such changes in water resources management and drought analysis. According to the report of the Intergovernmental Panel on Climate Change (Houghton et al. 1996), in the 20th century, global land precipitation has increased by 2% on average. The impact of climate change on the maximum and minimum temperatures of Gombe City in northeastern Nigeria has shown an increasing trend (Alhaji et al. 2018). Asfaw et al. (2018) investigated trends in the precipitation and temperature parameters for the Woleka Basin in northern Ethiopia and found that the number of dry years increased. Although the mean and minimum temperatures presented an increasing trend, an insignificant trend was observed for the maximum temperature values. Keskin et al. (2015) studied monthly and annual water levels in Lake Eğirdir in Turkey, using Mann-Kendall and Sen's slope tests. Based on their results, the annual water level was reduced by approximately 0.026 m. Karabulut et al. (2008) analyzed trends in rainfall and temperature data in the Samsun region between 1931 and 2006 and noted statistically significant trends in summer temperatures. Although there are numerous investigations on trends in hydrometeorological parameters and climate change (Cannarozzo et al. 2006; Yu et al. 2006; Kampata et al. 2008; Zhong, Li 2009; Kumar, Jain 2010; Santos et al. 2011; Yuce et al. 2015, 2018), only few studies have performed trend analyses in drought events (duration and severity) (Tabari et al. 2012; Ganguli, Reddy 2014; Spinoni et al. 2014; Dashtpajardi et al. 2015; Zhang et al. 2015; Yuce et al. 2022).

As of the beginning of 2021, most of Turkey is facing a severe drought. An increase in the number of dry days is inevitable after several low-rainfall seasons. In 2019, the summer and autumn months were largely devoid of rain, resulting in decreased reservoir water levels. The year 2020 was the driest of the last 5 years, with particularly little rainfall in the latter half of the year, according to a NASA report¹. This study will investigate the presence of any systematic changes in extreme drought events, using historical hydrometeorological data in the Ceyhan River Basin, which plays a critical role in the agricultural and hydropower production of the country. If the presence of any trend is detected, its magnitude and change point in the time series will be studied in detail. Furthermore, the trends of extreme drought events, such as the annual maximum drought severity (AMDS), defined as the largest cumulative severity value for each year, and the annual maximum drought duration (AMDD), which is described as the length of the maximum drought duration for each year, will be investigated. Notably, these two parameters are independent of one another. Here, the length of the AMDS may not be the same as the length of the AMDD within 1 year. Hence, AMDS and AMDD will be evaluated as different time series in statistical analysis tests. Both parameters of the extreme events are calculated by using the SPI method for multiple-time scales of 1, 3, 6, 9, and 12 months.

¹ <https://earthobservatory.nasa.gov/images/147811/turkey-experiences-intense-drought>

Table 1. Statistical parameters of observed rainfall stations; S.D., standard deviation; Cv, coefficient of variance; Cs, skewness; r1, kurtosis.

Station	Earliest record year	Latest record year	Latitude	Longitude	Mean (mm)	St. Dev.	Cv	Cs	r1
7767	1998	2012	37.3575	36.0907	65.64	55.53	0.85	1.06	0.26
8275	1964	1995	37.0901	36.3094	85.75	83.87	0.98	1.28	0.39
17255	1963	2016	37.5760	36.9150	60.39	65.57	1.09	1.27	0.50
17355	1986	2016	37.1021	36.2539	69.10	63.75	0.92	1.12	0.33
17866	1963	2011	38.0240	36.4823	51.19	46.29	0.90	1.07	0.39
17868	1970	2011	38.2405	36.9190	35.31	31.16	0.88	0.99	0.34
17870	1963	2011	38.2038	37.1982	33.30	28.87	0.87	0.97	0.33
17871	1993	2011	37.7867	37.6532	60.15	66.40	1.10	1.55	0.46
17908	1963	2011	37.4337	35.8188	70.24	58.79	0.84	1.11	0.23
17960	1964	2011	37.0153	35.7955	59.00	58.64	0.99	1.43	0.33
17979	1964	2011	36.7687	35.7903	67.54	70.99	1.05	1.55	0.33
D20M001	1963	2009	38.3000	37.5833	29.13	26.70	0.92	1.12	0.31
D20M002	1980	2005	37.5458	36.7747	58.40	66.96	1.15	1.51	0.42
D20M004	1970	1988	37.3833	37.1666	41.15	41.77	1.02	0.96	0.42
D20M006	1963	1974	37.1666	35.7000	53.98	60.21	1.12	1.85	0.30
D20M009	1963	2009	37.8833	36.8500	78.89	81.62	1.03	1.28	0.44
D20M011	1963	1996	38.6166	36.9333	32.32	29.73	0.92	1.28	0.27
D20M013	1968	2015	37.4666	37.2500	50.28	54.04	1.07	1.36	0.41
D20M014	1973	2015	37.3352	36.0056	90.27	78.25	0.87	1.15	0.25
D20M015	1976	2015	37.0500	36.0666	76.15	66.45	0.87	1.12	0.28
D20M016	1977	2015	37.5000	35.8333	78.27	69.64	0.89	1.25	0.25
D20M017	1980	2003	38.1520	36.4654	65.48	65.48	1.00	1.43	0.33
D20M018	1982	2002	38.2918	36.7604	25.09	28.13	1.12	2.29	0.19

3. Methodology

3.1. Standardized Precipitation Index

The *SPI* method, developed by McKee et al. (1993), is used to evaluate the level of deficiency in precipitation on different time scales ranging from 1 to 48 months. It is the most well-known and used index among many other indices to identify meteorological drought events and is based on fitting precipitation data to a probability distribution function (PDF). Gamma is the most suitable probability density distribution function for climatological data (Ganguli, Reddy 2014; Zhang et al. 2015). The dry period is considered to be the period in which the index is less than or equal to -1 . The *SPI*, which is classified based on values presented in Table 2, is determined by Equation 1:

$$SPI = \frac{X_{ij} - X_{im}}{\sigma} \quad (1)$$

where X_{ij} is the monthly precipitation amount and X_{im} and σ are the mean and standard deviation of precipitation evaluated from the all-monthly time series, respectively.

Table 2. *SPI* classification (McKee et al. 1993); *SPI* = Standardized Precipitation Index.

<i>SPI</i> value	Category
≥ 2	Extremely wet
1.50 to 1.99	Very wet
1.0 to 1.49	Moderately wet
0.99 to 0	Normal
0 to 0.99	Near normal
-1.00 to -1.49	Moderately dry
-1.50 to -1.99	Severely dry
≤ -2	Extremely dry

3.2 Homogeneity test

3.2.1 Wallis-Moore and Wald-Wolfowitz

The Wallis and Moore phase frequency test (Wallis, Moore 1941) is used to detect deviations of time series for randomness in the sequence of values. The test is based on sign differences (- or +), while the first and last phases named sequence of signs are not accounted thus the number of phases is identified. If $n \geq 10$ and continuity correction is applied, a fairly good test may be based on the hypothesis that the data are normally distributed, when $n \geq 25$, the correction is not used (Wallis, Moore 1941). The z test statistic is calculated as follows:

$$E[H] = \frac{1}{3}(2n - 7) \quad (2)$$

$$var[H] = \frac{1}{90}(16n - 29) \quad (3)$$

$$z = (H - E[H]) / \sqrt{\left(\frac{1}{90}(16n - 29)\right)} \quad (4)$$

where h is the number of phases, although the first and last phases are not taken into account. The z -statistic is normally distributed. A continuity correction of -0.5 is added to the denominator for $n \leq 30$.

The Wald-Wolfowitz test, which is also known as Runs test, measures the randomness of the data and examines whether an observation influences the subsequent observation. Time series data are cut from a certain level that could be the mean, medium, or mode to determine if each value in the series is lower or higher than this level. The number of passes from one data to the other above or below a certain level is called the run number, it is small if it is below or above long periods. Such series may not have homogeneity (Wald, Wolfowitz 1940). The result of the test is z , the number of data N , the number of runs r , the number of values below the medium level Na , the number of values above the medium level Nu ; the equations are as follows:

$$E[r] = \frac{2Na*Nu}{(Na+Nu)} + 1 \quad (5)$$

$$V[r] = \frac{2Na*Nu(2Na*Nu-N)}{(N-1)N^2} \quad (6)$$

$$z = \frac{r-1-E[r]}{\sqrt{V[r]}} \quad (7)$$

3.3. Trend Analysis

3.3.1. Mann-Kendall Test

The Mann-Kendall test is a non-parametric test to determine the trend in the hydrometeorological variable in a time series (Mann 1945; Kendall 1975; Helsel et al. 2002). It is the most preferred statistical method for time series since it is not fitted to any distribution. The application of the Mann-Kendall test statistic Z is expressed as follows:

$$S = \sum_{k=1}^{n-1} \sum_{j=k+1}^n \text{sgn}(x_j - x_k) \quad (8)$$

where n is the number of the data, x_j and x_k are the data point in years j and k ($j > k$), and t_i is the length of the tied rank group.

$$\text{sgn}(x_j - x_k) = \begin{cases} 1 & (x_j - x_k) > 0 \\ 0 & (x_j - x_k) = 0 \\ -1 & (x_j - x_k) < 0 \end{cases} \quad (9)$$

$$\text{Var}(S) = \frac{n(n-1)(2n+5) - \sum_i^r t_i(t_i-1)(2t_i+5)}{18} \quad (10)$$

$$Z = \begin{cases} \frac{S-1}{\sqrt{\text{Var}(S)}} & S > 0 \\ 0 & S = 0 \\ \frac{S+1}{\sqrt{\text{Var}(S)}} & S < 0 \end{cases} \quad (11)$$

A positive Z value indicates an increasing trend, whereas a negative value indicates a decreasing trend. Critical test statistical values are 1.645, 1.97, and 2.57 for different significance levels of 90%, 95%, and 99%, respectively (Yu et al. 1993).

3.3.2. Spearman's Rho Method

Spearman's rho test is a commonly employed nonparametric method to investigate the presence of trends (Lehmann, D'Abrera 1975; Sneyers 1990). Its statistics r_s and Z (standardized test statistics) are computed as follows:

$$r_s = 1 - \frac{[6 \sum_{i=1}^n (Rx_i - i)^2]}{n(n^2-1)} \quad (12)$$

$$z = r_s \sqrt{\frac{n-2}{1-r_s^2}} \quad (13)$$

where R_{xi} (rank statistic) is obtained by sorting the data, and n is the length of the time series. Negative z values show decreasing trends, whereas positive z values indicate increasing trends. At the 90% significance level, for $z > \pm 1.645$, the null hypothesis of no trend is rejected.

3.4. Trend Slope

3.4.1. Linear Regression Method

Regression analysis is a statistical method used to predict the relationships between one dependent variable and one or more independent variables. It forms the basis of complex estimation methods and is used to evaluate the strength of the relationship between variables and to model the relationship between them. The dependent variable is usually represented by Y , and the independent variables are denoted by X (Gocic, Trajkovic 2013). The linear regression formula is given as follows:

$$Y = a + bX \quad (14)$$

where a is the intercept, and b is the slope of the line. A positive b value indicates increasing trends, and a negative a value indicates decreasing trends.

3.4.2. Sen's Slope Estimator

Sen's slope test (Sen 1968) is a non-parametric test that calculates the slope of the trend in a data set; it is used for equiponderant time series. For each data point, the slope difference is calculated per changing time. The slope of the trend can be estimated by the median of all slopes between data pairs in the same season (Helsel et al. 2002). All slope pairs are ranked from smallest to largest, and if the calculated number of slopes (n) is odd, the median slope gives the slope S . If n is even, the two median slopes are averaged. Here, Q represents data, n is the length of the data, and T is time. The slope of n pair of data is predicted as follows:

$$S = \frac{Q_2 - Q_1}{T_2 - T_1} \quad (15)$$

$$S = \begin{cases} \frac{S_{n+1}}{2} & n = \text{even} \\ S_{\frac{n}{2}} & n = \text{odd} \end{cases} \quad (16)$$

3.5. Tests for Change Point Detection

Considering the importance of climatic variability in terms of water availability, increasing irrigation demand, crop yields, and other factors, it is crucial to identify and evaluate the trends in the monthly, seasonal, and annual historical data series. Change point detection is substantial to evaluate the period in which a significant change occurs in a time series. In this study, the standard normal homogeneity test (SNHT), Buishand's range test (BRT), and Pettitt's test (PT) were employed to detect change points in the time series.

3.5.1. Standard Normal Homogeneity Test

The statistic of the SNHT (Alexandersson 1986), (T_k), is used to compare the average of the first n year with the average of the last $(n - k)$ year with n data points (Vezzoli et al., 2012; Jaiswal et al., 2015). The T_k equation is as follows:

$$T_k = kZ_1^2 + (n - k)Z_2^2 \quad (17)$$

Z_1 and Z_2 can be calculated as follows:

$$Z_1 = \frac{1}{k} \sum_{i=1}^k \frac{(X_i - \bar{X})}{\sigma_X} \quad (18)$$

$$Z_2 = \frac{1}{n-k} \sum_{i=k+1}^n \frac{(X_i - \bar{X})}{\sigma_X} \quad (19)$$

Here, \bar{X} and σ_X are mean and standard deviation, respectively. The year in which T_k reaches the maximum value is considered as the point of change. The significant critical values for SNHT are given in Table 3.

Table 3. Critical values for different change point detection test statistics.

Number of Observations	Buishand Range Test			Pettitt Test		Standard Normal Homogeneity Test		
	1%	5%	10%	1%	5%	1%	5%	10%
20	1.6	1.43	1.1	71	57	9.56	6.95	6.07
30	1.7	1.5	1.12	133	107	10.45	7.65	6.6
40	1.74	1.53	1.13	208	167	11.01	8.1	6.92
50	1.78	1.55	1.14	293	235	11.38	8.45	7.15
70	1.81	1.59	1.17	488	393	11.89	8.8	7.47
100	1.86	1.62	1.22	841	677	12.32	9.15	7.77

3.5.2. Buishand's Range Test

The adjusted partial sum, S_k , is computed as follows:

$$S_k = \sum_{i=1}^k (X_i - \bar{X}) \quad (20)$$

When the series is homogeneous, the value of S_k fluctuates around zero. The test captures data showing sensitivity to break in the middle of distorting the homogeneity of the time series. If there is a change in K year, it reaches the maximum or minimum value around the year $k = K$ (Buishand 1982). The significant change can be computed by evaluating the rescale-adjusted range R :

$$R = \frac{\text{Max}(S_k) - \text{Min}(S_k)}{\bar{X}} \quad (21)$$

3.5.3. Pettitt's Test

PT is a non-parametric method (Pettitt 1979) to determine change detection in a time series. It is commonly used to calculate the occurrence of an unexpected change in hydrometeorological records (Sneyers 1990; Smadi, Zghoul 2006). The null hypothesis indicates that the series has an independent and random distribution, whereas the alternative hypothesis indicates a sudden change. The U_k test statistic is expressed as follows:

$$U_k = 2 \sum_{i=1}^k r_i - k(n+1) \quad k = 1, \dots, n \quad (22)$$

The U_k test results are presented graphically. In case of a break in $k = K$ year, the test statistic is at maximum or minimum values. Significant critical values are given in Table 3.

$$K = \max|U_k| \quad (23)$$

4. Analysis of Results

4.1. Homogeneity Analyses

The precipitation data of 23 meteorological stations in the Ceyhan River Basin were analyzed by the *SPI* drought index for time scales of 1, 3, 6, 9, and 12 months. The AMDS and AMDD time series for station 17355 are illustrated in Figure 2. These graphs do not show any statistically significant trend in the data and provide only a rough view of the variation of the data over time.

The Wallis and Moore phase-frequency test and the Wald-Wolfowitz test were employed for the analysis of extreme drought events (AMDS and AMDD), verifying the homogeneity for different time scales. The results of these two tests were compared to achieve an accurate homogeneity and randomness in the time series. If the outcomes of both tests suggest homogeneity in the time series, the presence of homogeneity is accepted. When only one of the methods suggests homogeneity of the time series, the results are defined as doubtful; if both methods suggest no homogeneity in the data set, it is labeled as non-homogeneous. The homogeneity test results for the AMDS and the AMDD time series of 23 meteorological stations for time scales of 1, 3, 6, 9, and 12-month are presented in Table 4.

In the AMDS time series, for *SPI* 1-month time scale, the data of 19 out of 23 stations indicated homogeneity by both tests, whereas stations 17871, 17979, and D20A011 presented homogeneity by one of the methods. Only station 17908 showed non-homogeneity by both tests for the significance level of 90%. For the same time scale, stations 8275, 17355, 17870, 17908, and D20A016 presented homogeneity by one of the methods, and only station D20A006 illustrated non-homogeneity by both methods; the data for the remaining stations were homogeneous in the AMDD time series. The AMDS time series were homogenous in all stations for the *SPI* 3-month time scale, apart from station 17960, which presented homogeneity by the Wald-Wolfowitz test. Although the AMDS time series presented homogeneity by one of the methods at 10 stations (17866, 17870, 17960, 17979, D20A002, D20A009, D20A011, D20A013,

D20A015, and D20A016), the data at only one station (8275) showed non-homogeneous characteristics. The data at the other stations showed homogeneous features.

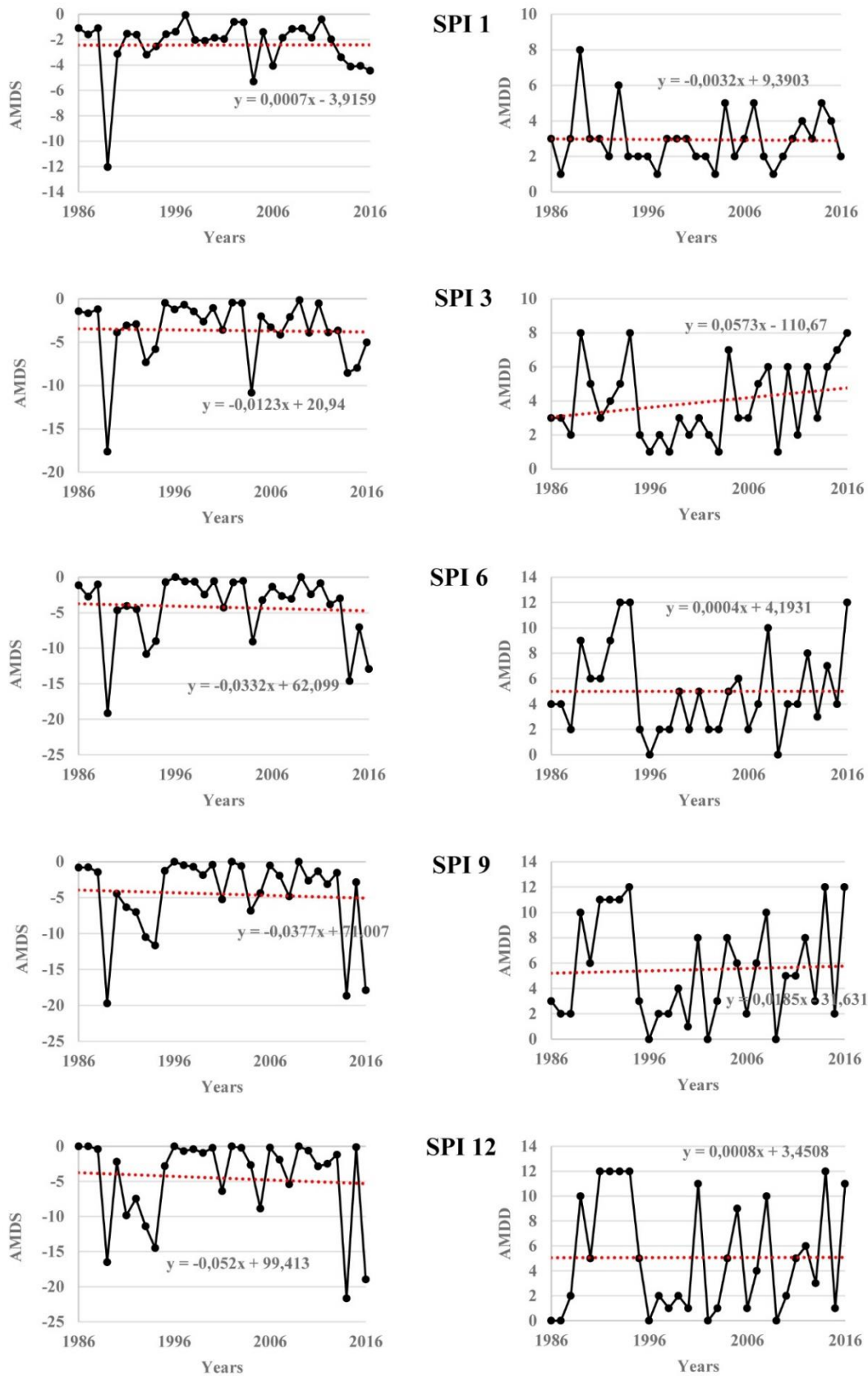


Fig. 2. The extreme drought events' both AMDS and AMDD time series of station 17355 at different time scales.

The *SPI* 6-month time scale AMDS time series presented homogeneity by one of the methods at stations 8275, 17868, and D20A002, whereas the other stations indicated homogenous data sets. The AMDD time series displayed non-homogenous features at stations 8275 and D20A013, homogeneous features by one of the methods at stations 17868, D20A016, and D20A017, and the data sets at the other stations were homogeneous by the two tests. With the increase in the length of the time scales, the number of non-homogenous stations also increased. For instance, three and five stations were non-homogenous for the *SPI* 9-month time scale and the *SPI* 12-month time scale, respectively. Station 17868 in both AMDS and AMDD as well as stations D20A001 and D20A016 in the AMDD time series were non-homogenous for the *SPI* 9-month time scale. Station 17868 in AMDS, stations D20A011 and D20A013 in both AMDS and AMDD, and stations D20A009 and D20A016 in the AMDD time series were non-homogenous for the *SPI* 12-month time scale.

Table 4. Homogeneity test results for extreme drought events at different time scales.

Station	Tests	<i>SPI</i> 1		<i>SPI</i> 3		<i>SPI</i> 6		<i>SPI</i> 9		<i>SPI</i> 12	
		AMDS	AMDD	AMDS	AMDD	AMDS	AMDD	AMDS	AMDD	AMDS	AMDD
7767	WM	-0.109	0.762	-0.109	1.415	0.762	0.109	0.109	1.415	0.762	0.762
	WW	-0.023	1.023	0.601	-0.369	1.607	1.513	2.246	1.815	2.161	1.714
	Result	H	H	H	H	H	H	D	D	D	D
8275	WM	1.727	3.453	0.863	3.453	2.590	1.727	1.727	1.727	1.295	0.432
	WW	0.387	1.238	0.671	2.887	1.331	1.710	0.103	0.837	-0.011	0.608
	Result	H	D	H	N-H	D	N-H	D	D	H	H
17255	WM	0.875	0.547	0.438	0.438	0.219	0.438	0.219	0.219	0.875	0.875
	WW	0.875	0.547	0.438	0.438	0.219	0.438	0.219	0.219	0.875	0.875
	Result	H	H	H	H	H	H	H	H	H	H
17355	WM	0.585	2.341	0.732	0.146	0.293	1.024	0.146	1.024	0.293	1.499
	WW	0.455	0.027	0.309	0.438	0.858	1.039	0.080	0.450	-0.476	0.759
	Result	H	D	H	H	H	H	H	H	H	H
17866	WM	1.957	1.151	1.266	2.187	0.115	1.496	0.806	0.806	0.460	1.496
	WW	-1.505	-1.232	-0.184	0.665	1.381	1.244	1.283	1.930	1.495	1.289
	Result	H	H	H	D	H	H	H	D	H	H
17868	WM	0.499	0.624	1.372	1.746	0.624	1.372	2.120	2.120	2.120	1.746
	WW	0.099	0.312	1.236	0.977	3.192	1.961	3.302	2.038	3.348	1.585
	Result	H	H	H	H	D	D	N-H	N-H	N-H	D
17870	WM	1.266	2.532	0.575	2.877	0.806	1.496	0.806	0.806	1.841	1.841
	WW	-0.988	-0.854	-0.293	0.048	0.217	0.839	0.348	0.603	0.956	1.540
	Result	H	D	H	D	H	H	H	H	D	D
17871	WM	0.095	0.095	0.095	0.474	0.667	-0.095	0.667	-0.095	0.477	0.477
	WW	-2.218	-1.781	-1.531	-1.103	-0.379	0.603	0.910	0.747	2.095	2.133
	Result	D	D	H	H	H	H	H	H	D	D
17908	WM	2.302	0.906	0.806	1.496	0.230	0.230	0.460	1.151	0.460	0.230
	WW	-2.217	-1.924	-1.293	-1.062	-0.166	0.088	0.452	0.511	0.742	0.336
	Result	N-H	D	H	H	H	H	H	H	H	H
17960	WM	0.465	0.233	1.861	2.160	0.116	0.116	0.116	0.582	0.931	0.233
	WW	-1.060	-0.731	-1.440	-0.941	0.116	0.116	1.137	0.989	2.242	1.343
	Result	H	H	D	D	H	H	H	H	D	H
17979	WM	1.861	0.233	0.814	2.155	0.465	0.465	0.116	0.931	0.465	1.603
	WW	-1.273	-1.320	-1.346	-0.790	0.376	-0.471	0.358	0.229	1.829	1.483
	Result	D	H	H	D	H	H	H	H	D	H
D20A001	WM	1.163	1.629	0.465	0.931	0.233	1.629	1.629	2.327	1.629	1.214
	WW	-1.294	-1.493	-1.297	-0.574	-0.276	1.231	0.166	1.945	1.098	2.059
	Result	H	H	H	H	H	H	H	N-H	H	D

D20A002	WM	0.723	0.723	0.723	1.688	0.723	0.723	0.723	0.723	0.241	1.741
	WW	-1.070	-0.054	-0.142	0.224	1.844	0.199	1.867	1.189	2.366	0.952
	Result	H	H	H	D	D	H	D	H	D	D
D20A004	WM	0.477	0.477	0.095	0.477	0.477	1.621	1.621	1.621	0.095	0.477
	WW	0.299	-0.257	-0.097	0.129	0.970	1.265	1.596	1.685	0.927	0.960
	Result	H	H	H	H	H	H	H	D	H	H
D20A006	WM	-0.124	2.849	0.124	1.610	0.124	1.610	1.610	1.610	0.124	0.124
	WW	-1.027	-1.976	-0.951	0.360	0.104	-0.491	0.142	0.053	0.091	-0.351
	Result	H	N-H	H	H	H	H	H	H	H	H
D20A009	WM	0.353	0.353	1.059	1.764	0.353	1.059	1.764	1.282	1.059	2.470
	WW	0.707	0.005	-0.629	0.244	0.484	1.610	0.675	2.166	0.763	2.414
	Result	H	H	H	D	H	H	D	D	H	N-H
D20A011	WM	1.812	0.558	0.975	2.443	0.975	0.975	0.139	1.665	1.812	2.648
	WW	-0.190	0.403	-1.091	-1.233	0.382	0.539	0.822	1.163	1.719	2.297
	Result	D	H	H	D	H	H	H	D	N-H	N-H
D20A013	WM	0.233	0.931	0.582	1.978	0.582	2.676	0.582	1.978	1.978	1.978
	WW	-0.688	0.043	-0.491	0.253	1.180	1.729	1.738	1.273	2.021	2.414
	Result	H	H	H	D	H	N-H	D	D	N-H	N-H
D20A014	WM	0.562	1.601	0.616	0.985	1.355	0.616	0.862	1.601	0.616	0.862
	WW	-0.977	-0.156	-0.549	-0.235	-0.371	0.349	-0.201	1.510	-0.061	1.018
	Result	H	H	H	H	H	H	H	H	H	H
D20A015	WM	1.024	1.279	0.640	0.128	0.640	0.128	0.128	0.640	0.640	0.128
	WW	-0.954	-0.985	-0.952	-1.950	-0.189	0.732	-0.192	1.006	-0.103	1.576
	Result	H	H	H	D	H	H	H	H	H	H
D20A016	WM	0.519	1.815	1.037	1.815	0.648	1.426	1.426	2.204	1.426	2.204
	WW	-0.636	-0.255	-0.496	-0.544	1.628	1.699	1.753	2.184	1.482	2.095
	Result	H	D	H	D	H	D	D	N-H	H	N-H
D20A017	WM	0.420	1.594	0.420	0.084	1.091	2.602	0.084	0.084	0.084	1.091
	WW	-0.044	0.614	-0.176	-0.187	0.187	1.160	-0.375	-0.120	-0.358	0.290
	Result	H	H	H	H	H	D	H	H	H	H
D20A018	WM	0.090	1.173	0.451	1.173	0.451	0.090	1.173	0.090	1.715	-0.090
	WW	-0.095	-0.103	-0.592	-0.373	-0.755	-0.362	0.410	0.056	1.151	0.282
	Result	H	H	H	H	H	H	H	H	D	H

H: Homogeneous, **D:** Doubtful, **N-H:** Non-homogeneous

4.2. Trend Analyses

Trend detection analysis of extreme drought event time series under the influence of climate change is critical to propose and make use of management strategies. Table 5 summarizes the outcomes of the Spearman Rho and Mann-Kendall statistical tests used to detect any trends in the *SPI* 1-,3-,6-,9-, and 12-month time series. The null hypothesis is not rejected at the 90% significance level where $-1.64 < z < 1.64$. The Mann-Kendall and Spearman Rho methods performed similarly in the analysis of trend detection in the extreme drought event time series (Table 5). For the *SPI* 1-month time scale, a significant trend was not detected by both tests in the extreme drought events, except in the data of stations 17868 and D20A014. Although two tests showed a statistically significant increasing trend in the AMDS series of station 17868, the AMDD series of station D20A014 showed a statistically significant decreasing trend. In the *SPI* 3-month time scale, the statistically significant increasing trend was evaluated only in the AMDS series of station 7767 and in the AMDD series of station 8275. In the case of the *SPI* 6-month time scale, the time series at four stations showed statistically significant trends in both test results. The AMDS and AMDD time series at station 7767 showed increasing and decreasing trends, respectively. Statistically

significant increasing trends were observed in the AMDS time series of stations 8275, 17866, and D20A016, whereas decreasing trends were noted in the AMDS time series of station D20A016, with a significance level of 90%. As in the *SPI* 3-month period, similar results were clearly seen for the *SPI* 9-month time scale of stations 7767, 8275, and D20A016. In the time series at five stations, statistically significant trends were determined for the *SPI* 12-month time scale. Increasing trends were perceived in the AMDS time series of stations 7767 and D20A018, whereas decreasing trends were detected in the AMDS time series of stations 8275 and D20A016. Furthermore, both tests demonstrated a statistically significant increasing trend in the AMDD time series of stations 8275 and D20A009.

Table 5. Trend detection results for extreme drought events.

Station	Tests	<i>SPI</i> 1		<i>SPI</i> 3		<i>SPI</i> 6		<i>SPI</i> 9		<i>SPI</i> 12	
		AMDS	AMDD	AMDS	AMDD	AMDS	AMDD	AMDS	AMDD	AMDS	AMDD
7767	MK	1.683	-1.093	1.683	-0.855	2.474	-2.448	2.428	-1.910	2.138	-1.706
	SR	1.537	-1.131	1.684	-0.974	2.499	-2.497	2.160	-1.935	1.918	-1.628
	Result	N	N	I	N	I	D	I	D	I	N
8275	MK	-0.276	0.685	-0.584	1.755	-1.674	1.947	-1.384	1.704	-1.860	1.874
	SR	-0.297	0.697	-0.534	1.691	-1.595	1.787	-1.409	1.693	-1.762	1.957
	Result	N	N	N	I	N	I	N	I	D	I
17255	MK	0.149	-0.265	0.261	0.008	0.351	-0.196	0.441	-0.565	0.211	-0.479
	SR	0.143	-0.273	0.411	0.079	0.425	-0.259	0.478	-0.506	0.179	-0.419
	Result	N	N	N	N	N	N	N	N	N	N
17355	MK	-1.105	0.283	-0.952	1.211	-0.391	0.242	-0.255	0.377	-0.307	0.309
	SR	-1.203	0.369	-1.014	1.123	-0.370	0.066	-0.234	0.345	-0.474	0.251
	Result	N	N	N	N	N	N	N	N	N	N
17866	MK	-0.060	0.894	-0.681	0.755	-0.534	1.712	-1.036	1.050	-1.529	1.432
	SR	-0.063	0.897	-0.674	0.787	-0.663	1.901	-1.151	1.086	-1.616	1.440
	Result	N	N	N	N	N	I	N	N	N	N
17868	MK	1.767	-1.019	0.900	-0.373	0.293	0.000	-0.163	0.087	0.043	-0.515
	SR	1.667	-1.012	1.009	-0.512	0.282	0.232	-0.179	0.153	-0.020	-0.547
	Result	I	N	N	N	N	N	N	N	N	N
17870	MK	0.448	0.323	0.509	-0.731	0.552	0.409	-0.276	0.772	0.000	0.529
	SR	0.459	0.243	0.413	-0.667	0.498	0.426	-0.333	0.837	0.626	-0.984
	Result	N	N	N	N	N	N	N	N	N	N
17871	MK	1.469	-0.184	0.350	0.606	0.000	0.748	-0.771	0.634	-0.703	0.958
	SR	1.236	-0.257	0.055	0.582	-0.045	0.816	-0.760	0.823	-0.800	1.065
	Result	N	N	N	N	N	N	N	N	N	N
17908	MK	0.620	-0.254	1.121	-1.243	0.992	0.452	-0.173	0.564	-0.476	0.923
	SR	0.620	0.111	1.228	-1.323	0.946	0.469	-0.104	0.531	-0.463	0.836
	Result	N	N	N	N	N	N	N	N	N	N
17960	MK	-0.453	0.009	0.604	-0.579	0.871	-0.729	0.792	-0.626	0.561	-1.433
	SR	-0.513	0.045	0.053	-0.493	0.791	-0.741	0.696	-0.567	0.562	-1.403
	Result	N	N	N	N	N	N	N	N	N	N
17979	MK	-1.129	0.256	-0.044	-0.469	0.836	-1.044	0.818	-1.117	0.873	-0.777
	SR	-1.137	0.264	0.200	-0.445	0.852	-1.000	0.655	-1.185	0.938	-0.689
	Result	N	N	N	N	N	N	N	N	N	N
D20A001	MK	0.756	-0.347	0.053	0.000	0.231	0.072	-0.044	-0.134	-0.250	0.467
	SR	0.831	-0.325	0.159	0.155	0.216	0.126	-0.010	-0.185	-0.221	0.400
	Result	N	N	N	N	N	N	N	N	N	N
D20A002	MK	-1.058	-0.206	-1.236	-0.246	-0.243	-0.178	0.133	-0.621	-0.441	0.155
	SR	-1.250	-0.180	-1.280	-0.203	-0.456	-0.107	-0.175	-0.472	-0.024	0.155
	Result	N	N	N	N	N	N	N	N	N	N
D20A004	MK	1.295	-0.616	0.910	0.146	0.560	-0.543	0.070	-0.035	0.596	0.035
	SR	1.396	-0.644	0.968	0.035	0.514	-0.622	0.246	-0.180	0.775	-0.120

	Result	N	N	N	N	N	N	N	N	N	N
D20A006	MK	0.480	0.287	-0.069	-0.071	-0.206	0.972	-0.754	1.038	-0.630	1.196
	SR	0.255	0.349	-0.162	-0.250	-0.186	0.971	-0.742	0.864	-0.449	1.031
	Result	N	N	N	N	N	N	N	N	N	N
D20A009	MK	-0.578	0.973	-0.604	0.046	-0.569	0.805	-0.991	1.519	-1.584	1.656
	SR	-0.541	0.978	-0.205	0.123	-0.396	0.702	-0.965	1.502	-1.575	1.706
	Result	N	N	N	N	N	N	N	N	N	I
D20A011	MK	-0.030	-0.076	-0.030	0.406	-0.445	0.569	-0.742	0.313	-0.388	0.165
	SR	-0.180	-0.109	-0.020	0.422	-0.442	0.577	-0.883	0.449	-0.560	0.158
	Result	N	N	N	N	N	N	N	N	N	N
D20A013	MK	-0.764	-0.009	-0.098	0.451	-0.018	0.537	-0.463	0.789	-0.602	0.976
	SR	-0.680	-0.083	-0.090	0.446	0.017	0.580	-0.569	0.881	-0.591	0.897
	Result	N	N	N	N	N	N	N	N	N	N
D20A014	MK	1.026	-1.901	1.256	-1.063	-0.345	0.453	-1.057	1.381	-0.744	1.157
	SR	0.949	-1.910	1.181	-1.058	-0.463	0.520	-1.064	1.204	-0.769	1.084
	Result	N	D	N	N	N	N	N	N	N	N
D20A015	MK	-0.350	-0.303	0.105	-0.142	0.245	-0.647	0.478	-0.844	-0.117	0.459
	SR	-0.304	-0.316	-0.013	-0.099	0.305	-0.684	0.471	-0.787	-0.178	0.407
	Result	N	N	N	N	N	N	N	N	N	N
D20A016	MK	-1.476	0.224	-1.694	1.583	-2.762	2.421	-2.407	2.002	-1.947	1.783
	SR	-1.424	0.225	-1.599	1.550	-2.586	2.301	-2.335	1.917	-1.696	1.514
	Result	N	N	N	N	D	I	D	I	D	N
D20A017	MK	-0.819	-0.027	0.050	-1.236	-0.273	0.505	-0.893	0.526	-0.821	-1.706
	SR	-0.776	-0.138	0.123	-1.205	-0.225	0.521	-0.913	0.481	-0.844	0.785
	Result	N	N	N	N	N	N	N	N	N	N
D20A018	MK	-1.300	0.415	-0.151	0.093	-0.091	-0.092	-0.151	0.731	-0.967	1.798
	SR	-1.377	0.418	-0.279	0.340	-0.087	0.029	-0.296	0.921	-1.078	1.714
	Result	N	N	N	N	N	N	N	N	N	I

N: No Trend, D: Decreasing, I: Increasing, MK: Mann-Kendall, SR: Spearman Rho

4.3. Trend Magnitude

Sen's slope estimator and linear regression analysis were employed to determine the slope of trends in the AMDS and AMDD time series. The signs of the slopes were in line with the results of the Spearman Rho and Mann-Kendall tests. The slopes of the trend lines are indicated in bold in the time series where the trend was detected (Table 6). The highest slopes of the trend line, ranging from 0.6 to 0.8 for both tests, were detected in the AMDS time series of station 7767 for the *SPI* 9-month time scale. The other evaluated slopes of the trend were 0.067 in AMDD time series of station 8275 for the *SPI* 3-month time scale, 0.179 in the AMDD time series of station 8275 for the *SPI* 6-month period, 0.106 in the AMDD time series of station 8275 for the *SPI* 9-month period, 0.083 in AMDS time series of station 8275 for the *SPI* 12-month period, and 0.138 in the AMDD time series of station 8275 for the *SPI* 12-month period.

Table 6. Trend Magnitude Test results for all stations.

Station	Tests	<i>SPI</i> 1		<i>SPI</i> 3		<i>SPI</i> 6		<i>SPI</i> 9		<i>SPI</i> 12	
		AMDS	AMDD	AMDS	AMDD	AMDS	AMDD	AMDS	AMDD	AMDS	AMDD
7767	SS	0.132	0.000	0.340	-0.125	0.495	-0.333	0.768	-0.600	0.710	-0.500
	R	0.150	-0.079	0.297	-0.118	0.480	-0.379	0.759	-0.464	0.798	-0.432
8275	SS	-0.007	0.000	-0.032	0.067	-0.091	0.179	-0.076	0.106	-0.071	0.083
	R	-0.018	0.024	-0.045	0.073	-0.129	0.138	-0.149	0.145	-0.189	0.138
17255	SS	0.002	0.000	0.006	0.000	0.010	0.000	0.005	0.000	0.000	0.000
	R	-0.003	-0.003	0.000	0.003	-0.014	0.001	-0.010	-0.020	0.002	-0.027
17355	SS	-0.025	0.000	-0.050	0.050	-0.025	0.000	-0.018	0.000	-0.007	0.000

17866	R	0.001	-0.003	-0.012	0.057	-0.033	0.000	-0.038	0.019	-0.052	0.001
	SS	0.000	0.000	-0.013	0.000	-0.016	0.042	-0.028	0.032	-0.023	0.036
17868	R	-0.002	0.017	-0.021	0.021	-0.025	0.059	-0.033	0.034	-0.050	0.060
	SS	0.024	0.000	0.032	0.000	0.016	0.000	-0.002	0.000	0.000	0.000
17870	R	0.018	-0.021	0.032	-0.012	0.068	-0.007	0.061	0.005	0.079	-0.037
	SS	0.005	0.000	0.013	0.000	0.018	0.000	-0.005	0.010	-0.009	0.000
17871	R	0.019	-0.010	0.021	-0.012	0.024	0.012	0.005	0.023	-0.008	0.023
	SS	0.081	0.000	0.033	0.000	0.017	0.100	-0.081	0.125	-0.073	0.143
17908	R	0.042	-0.004	0.080	0.042	-0.007	0.096	-0.078	0.109	-0.124	0.175
	SS	0.006	0.000	0.030	0.000	0.031	0.000	-0.001	0.000	-0.001	0.000
17960	R	0.005	-0.006	0.031	-0.023	0.026	0.013	-0.003	0.020	-0.018	0.026
	SS	-0.006	0.000	0.014	0.000	0.028	0.000	0.019	0.000	0.010	-0.048
17979	R	-0.015	0.004	0.004	0.001	0.029	-0.022	0.061	-0.045	0.080	-0.072
	SS	-0.010	0.000	-0.001	0.000	0.029	0.000	0.022	-0.028	0.019	0.000
D20A001	R	-0.011	0.003	0.003	-0.008	0.043	-0.026	0.062	-0.037	0.098	-0.046
	SS	0.008	0.000	0.001	0.000	0.008	0.000	0.000	0.000	0.000	0.000
D20A002	R	-0.010	-0.001	-0.041	0.022	-0.009	0.002	-0.005	-0.017	-0.021	0.149
	SS	-0.038	0.000	-0.011	0.000	-0.023	0.000	-0.003	-0.077	0.000	0.000
D20A004	R	-0.025	0.057	-0.029	-0.009	-0.116	0.021	-0.102	-0.049	-0.123	-0.014
	SS	0.062	0.000	0.106	0.000	0.108	0.000	0.016	0.000	0.038	0.000
D20A006	R	0.064	-0.047	0.144	-0.072	0.175	-0.111	0.190	-0.021	0.137	0.044
	SS	0.080	0.000	-0.019	0.000	-0.062	0.367	-0.256	0.438	-0.345	0.500
D20A009	R	0.012	0.042	-0.005	0.038	-0.083	0.245	-0.101	0.329	-0.134	0.378
	SS	-0.005	0.000	-0.002	0.000	-0.021	0.000	-0.023	0.050	-0.025	0.037
D20A011	R	-0.010	0.016	-0.006	-0.002	-0.003	0.016	-0.017	0.060	-0.020	0.066
	SS	-0.001	0.000	-0.001	0.000	-0.027	0.000	-0.029	0.000	0.000	0.000
D20A013	R	-0.014	0.006	-0.008	0.008	-0.013	0.017	-0.033	0.024	-0.097	0.028
	SS	-0.011	0.000	-0.005	0.000	0.000	0.000	-0.006	0.000	0.000	0.000
D20A014	R	-0.010	-0.003	0.003	0.011	0.021	0.010	0.020	0.016	0.012	0.032
	SS	0.014	0.000	0.042	0.000	-0.009	0.000	-0.024	0.054	-0.012	0.000
D20A015	R	0.024	-0.042	0.051	-0.035	0.017	0.018	-0.010	0.051	-0.027	0.057
	SS	-0.006	0.000	0.005	0.000	0.007	0.000	0.017	-0.034	0.000	0.000
D20A016	R	0.007	-0.005	-0.011	-0.006	-0.001	-0.025	0.016	-0.038	-0.001	0.013
	SS	-0.033	0.000	-0.072	0.043	-0.156	0.133	-0.096	0.100	-0.071	0.091
D20A017	R	-0.034	0.011	-0.081	0.050	-0.163	0.125	-0.184	0.111	-0.198	0.115
	SS	-0.034	0.000	0.002	-0.080	-0.034	0.000	-0.042	0.024	-0.034	0.079
D20A018	R	-0.008	-0.016	0.034	-0.084	-0.023	0.020	-0.073	0.047	-0.059	0.065
	SS	-0.050	0.000	-0.026	0.000	-0.051	0.000	-0.018	0.100	-0.127	0.286
D20A018	R	-0.056	0.031	-0.011	0.025	-0.019	-0.014	-0.098	0.106	-0.203	0.227

4.4. Change Point Detection

After determining the presence of a trend as well as its slope in the time series of extreme drought events, SNHT, BRT, and PT were applied to define the point where the change had started. The change point is identified as the point where the change point occurs in SNHT and BRT, which can be depicted graphically. The outcomes of the three methods were compared to assess a precise change point. As two of the three tests presented the same results, that specific point was chosen to be the change point for the particular time series. However, if the outcomes of all three tests were inconsistent, the change point selection was denoted as suspicious (S). The change points for extreme drought events of the AMDS and AMDD time series are presented in Table 7.

Table 7. Change point results of extreme drought events.

Station	Tests	Test criteria	SPI 1		SPI 3		SPI 6		SPI 9		SPI 12	
			AMDS	AMDD	AMDS	AMDD	AMDS	AMDD	AMDS	AMDD	AMDS	AMDD
7767	BRT	R/sqrt(n)min	0.91	1.14	0.99	0.83	1.48	1.09	1.29	1.17	1.34	1.21
		CP	NC	NC	2000	NC	2001	2008	2001	2008	2001	NC
	SNH T	T	3.15	4.97	6.08	3.80	7.08	6.05	7.62	5.68	7.25	4.94
		CP	NC	NC	2000	NC	2001	2008	2001	2008	2001	NC
	PT	U	28	31	59	28	62	61	58	65	68	34
		CP	NC	NC	2000	NC	2001	2004	2001	2008	2008	NC
	Result	NC	NC	2000	NC	2001	2008	2001	2008	2001	NC	
8275	BRT	R/sqrt(n)min	0.99	0.93	1.07	1.49	1.2	1.22	1.06	1.5	1.05	1.4
		CP	NC	NC	NC	1979	NC	1980	NC	1969	1980	1980
	SNH T	T	3.92	3.1	2.31	6.91	4.4	6.7	3.55	6.3	6.2	6.4
		CP	NC	NC	NC	1979	NC	1969	NC	1969	1982	1969
	PT	U	65	65	63	123	59	105	92	102	113	105
		CP	NC	NC	NC	1979	NC	1979	NC	1969	1980	1969
	Result	NC	NC	NC	1979	NC	SC	NC	1969	1980	1969	
17866	BRT	R/sqrt(n)min	0.9	0.93	0.84	0.9	0.94	1.12	0.96	0.95	1.04	1.07
		CP	NC	NC	NC	NC	NC	1984	NC	NC	NC	NC
	SNH T	T	1.3	3.11	2.09	2.38	2.17	7.1	2.17	2.22	2.84	3.49
		CP	NC	NC	NC	NC	NC	1981	NC	NC	NC	NC
	PT	U	102	127	122	135	148	225	185	157	228	195
		CP	NC	NC	NC	NC	NC	1981	NC	NC	NC	NC
	Result	NC	NC	NC	NC	NC	1981	NC	NC	NC	NC	
D20A009	BRT	R/sqrt(n)min	0.83	1.66	0.79	0.82	0.8	0.87	0.82	0.9	0.83	1.14
		CP	NC	NC	NC	NC	NC	NC	NC	NC	NC	1982
	SNH T	T	3.95	5.77	1.76	2.82	2.65	1.89	2.38	3.88	2.01	7.3
		CP	NC	NC	NC	NC	NC	NC	NC	NC	NC	1982
	PT	U	143	130	112	121	115	126	148	130	123	205
		CP	NC	NC	NC	NC	NC	NC	NC	NC	NC	1982
	Result	NC	NC	NC	NC	NC	NC	NC	NC	NC	1982	
D20A014	BRT	R/sqrt(n)min	0.95	1.14	1.068	0.96	1.05	1.53	1.14	1.87	1.23	1.64
		CP	NC	1980	NC	NC						
	SNH T	T	2.78	3.4	3.42	5.53	2.17	3.89	2.7	5.5	3.17	5.32
		CP	NC	1975	NC	NC						
	PT	U	128	159	134	134	136	157	141	128	116	142
		CP	NC	1999	NC	NC						
	Result	NC	SC	NC								
D20A016	BRT	R / sqrt(n)min	0.82	0.97	1.04	0.88	1.22	1.26	1.3	1.65	1.34	0.9
		CP	NC	NC	NC	NC	1988	1988	1988	1988	1996	NC
	SNH T	T	3.95	5.43	5.16	3.48	7.02	7.28	6.93	7.7	6.95	5.3
		CP	NC	NC	NC	NC	1988	1984	1988	1984	1988	NC
	PT	U	116	69	144	120	188	181	193	188	169	158
		CP	NC	NC	NC	NC	1988	1988	1988	1988	1988	NC
	Result	NC	NC	NC	NC	1988	1988	1988	1988	1988	NC	
D20A018	BRT	R/sqrt(n)min	0.77	0.85	0.94	0.82	0.61	0.67	0.83	0.84	1.01	1.04
		CP	NC	NC	NC	NC	NC	NC	NC	NC	NC	1988
	SNH T	T	3.42	1.82	1.68	2.91	1.42	1.64	1.62	1.94	2.99	6.98
		CP	NC	NC	NC	NC	NC	NC	NC	NC	NC	1984
	PT	U	45	34	36	31	22	23	28	42	44	63
		CP	NC	NC	NC	NC	NC	NC	NC	NC	NC	1988
	Result	NC	NC	NC	NC	NC	NC	NC	NC	NC	1988	

NC: No change

All three tests were performed with a significance level of 90%. According to test results, no abrupt changes were found at station 7767 for the *SPI* 1-month period in the AMDS and AMDD time series, the *SPI* 3-month period in the AMDD time series, and the *SPI* 12-month period in the AMDD time series. Changes in the AMDS time series were noted in the year 2000 for *SPI* 3-, in 2001 for *SPI* 6-, 9-, and 12-month time scales. Changes in the AMDD series were found in 2008 for *SPI* 6- and *SPI* 9- at station 7767. We detected no changes in both the AMDS and AMDD time series at station D20A014. Changes were observed in 1981 at station 17866 for the *SPI* 6- in the AMDD time series, in 1982 at station D20A009 for the *SPI* 12- in the AMDD time series, and in 1988 at station D20A018 for the *SPI* 12- AMDD time series (Fig. 3).

In general, numerous change points were detected at stations 7767, 8275, and D20A016, with a significance level of 90%. Although there were no changes for the *SPI* 1- month time scales and the *SPI* 3-month time scales at station 8275, the years 1979, 1969, and 1980 were critical for the *SPI* 6- AMDS time series, the *SPI* 9- AMDD time series, and the *SPI* 12- AMDS time series, respectively. At station D20A016, the change point was detected in 1988, which was a critical year for the *SPI* 6-AMDS and AMDD time series, for the *SPI* 9- AMDS and AMDD time series, and for the *SPI* 12- AMDS time series.

5. Discussion and Conclusions

The AMDS and the AMDD trends in extreme drought events were evaluated in this study. The *SPI* drought index was used to assess the extreme events for 23 meteorological stations in Ceyhan Basin over several time scales of 1, 3, 6, 9, and 12 months. The AMDS and AMDD time series are important extreme hydrological drought events in disaster preparedness and the regional management of water supplies. The homogeneity of the extreme drought occurrence time series was investigated using the Wallis-Moore and Wald-Wolfowitz methods, and Mann-Kendal and Spearman Rho trend analyses were carried out. Sen's slope estimator and linear regression analysis were used to assess the magnitude of trends, and the SNHT, BRT, and PT were used to identify the change point that denotes the start of the trend.

The number of stations with non-homogeneous data increased as the *SPI* time scales increased, especially in the AMDS time series. Most of the stations seemed to have homogeneous time series; however, the data in a few stations were homogeneous by one of the methods and non-homogeneous by the other one, with a significance level of 90%.

In the AMDS series, an increasing trend was observed only in the station 7767 data for 3-, 6-, 9-, and 12-month time scales, whereas decreasing trends were detected in station 8275 for the 12-month time scale and in station D20A016 for the 6-, 9-, and 12-month time scales. Nevertheless, in the AMDD time series, increasing trends were noted in station 8275 for the 3-, 6-, 9-, and 12-month time scales, station 17866 for the 6-month time scale, station D20A009 for the 12-month time scale, station D20A016 for the 6- and 9-month time scales, and station D20A018 for the 12-month time scale, whereas decreasing trends were perceived in the station 7767 for the 6- and 9-month time scales and in station D20A014 for the 1-month time scale.

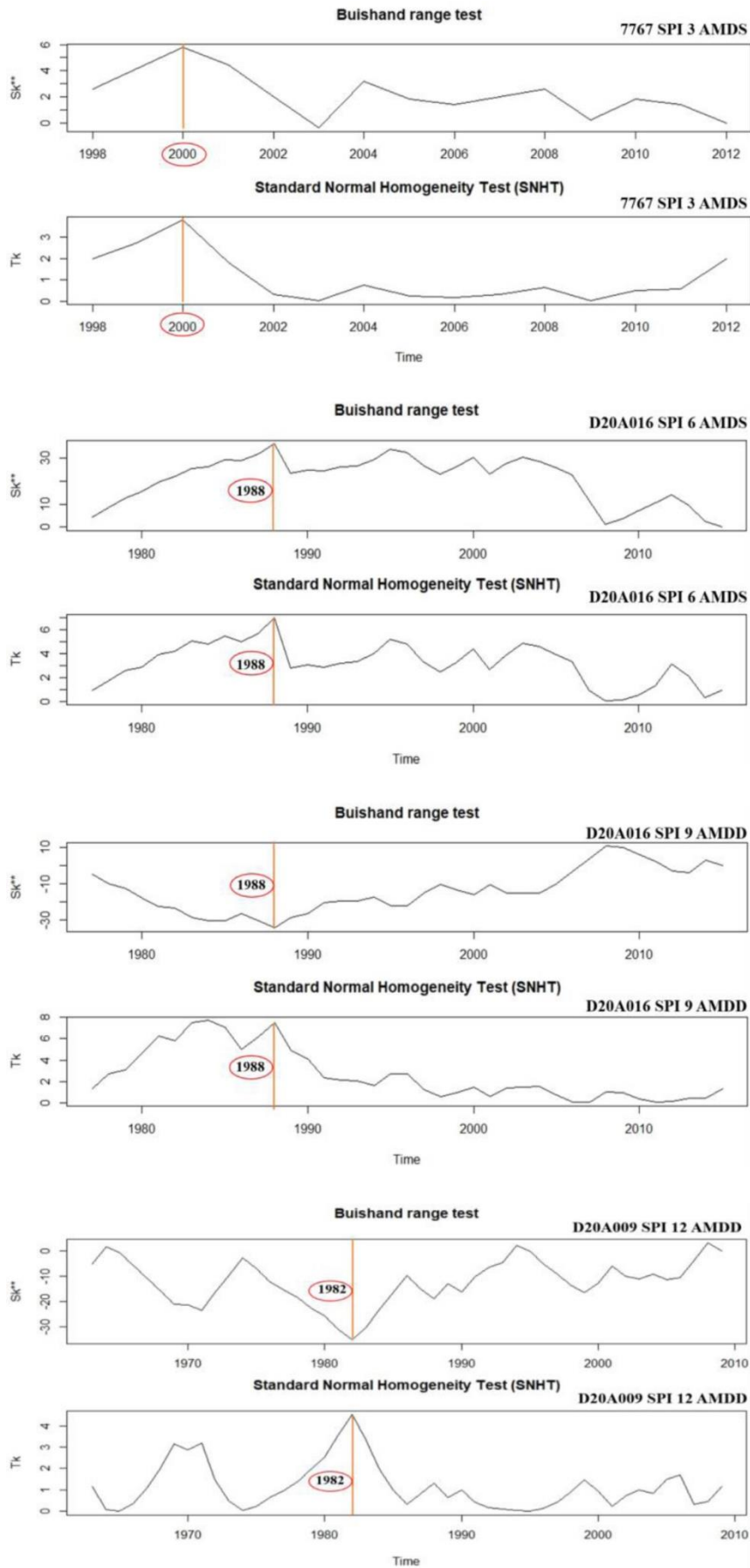


Fig. 3. Change point results for different time scales of *SPI* 3, 6, 9, and 12 months.

These results indicate that the AMDD time series with higher time scales revealed an increasing trend, whereas the AMDS time series showed a decreasing trend, which was statistically significant at the 90% confidence level.

Possible change points started after 1988 for D20A016 and D20A018, whereas the data in stations 7767, 8275, 17866, and D20A009 shifted after late 2000, 1969, 1981, and 1982, respectively. Change point detection tests captured different years in the data of some stations, most likely because of climate type, topography, and hydrological conditions, among others. Investigations on drought and climate change at local scales need to be periodically repeated to assess the impacts of precipitation, temperature, evapotranspiration, and groundwater level on agriculture, water resources and food security, energy production and security, economic growth, ecosystem sustainability, environmental health, and health security. The results of this study are consistent with previous findings. For instance, Dikici and Aksel, (2021) indicated that precipitation is generally decreasing, considering a 50-year period. According to their calculations, the basin faces a severe drought threat in the 20-year return period. Tosunoglu and Kisi (2016) investigated the trends of maximum hydrologic drought variables, annual maximum duration (AMD), and annual maximum severity (AMS) using MK, modified MK, and the recently developed Sen's innovative trend analysis (ITA) techniques. Increasing trends in the severity of the drought at the stations 2316 and 2323 were captured by the modified MK and ITA techniques, respectively. The possibility of future droughts or water shortages in these stations should be considered. The results of this paper provide valuable information to water resource management decision-makers in the Ceyhan River Basin for evaluating the effects of droughts and preparing for drought mitigation measures to avoid future drought risks.

Declaration of Competing Interests

The authors declare that they have no known competing financial interests or personal relationships that could have appeared to influence the work reported in this paper.

Acknowledgment

We are grateful to the General Directorate of Meteorology of the Ministry of Agriculture and Forestry in Turkey for providing us with the data used in this study.

Reference

- Alexandersson H., 1986, A homogeneity test applied to precipitation data, *International Journal of Climatology*, 6 (6), 661-675, DOI: 10.1002/joc.3370060607.
- Alhaji U., Yusuf A.S., Edet C.O., Oche C.O., Agbo E.P., 2018, Trend analysis of temperature in Gombe State using Mann Kendall Trend Test, *Journal of Scientific Research and Reports*, DOI: 10.9734/JSRR/2018/42029.
- Asfaw A., Simane B., Hassen A., Bantider A., 2018, Variability and time series trend analysis of rainfall and temperature in northcentral Ethiopia: A case study in Woleka sub-basin, *Weather and Climate Extremes*, 19, 29-41, DOI: 10.1016/j.wace.2017.12.002.
- Buishand T.A., 1982, Some methods for testing the homogeneity of rainfall records, *Journal of Hydrology*, 58 (1), 11-27, DOI: 10.1016/0022-1694(82)90066-X.

- Burn D.H., Sharif M., Zhang K., 2010, Detection of trends in hydrological extremes for Canadian watersheds, *Hydrological Processes*, 24 (13), 1781-1790, DOI: 10.1002/hyp.7625.
- Cannarozzo M., Noto L.V., Viola F., 2006, Spatial distribution of rainfall trends in Sicily (1921-2000), *Physics and Chemistry of the Earth. Parts A/B/C*, 31 (18), 1201-1211, DOI: 10.1016/j.pce.2006.03.022.
- Dashtpajardi M.M., Kousari M.R., Vagharfard H., Ghonchepour D., Hosseini M.E., Ahani H., 2015, An investigation of drought magnitude trend during 1975-2005 in arid and semi-arid regions of Iran, *Environmental Earth Sciences*, 73, 1231-1244, DOI: 10.1007/s12665-014-3477-1.
- Demuth S., Bakenhus A., 1994, *Hydrological Drought – A literature review*, University of Freiburg, Freiburg, Germany.
- Dikići M., Aksel M., 2021, Comparison of drought indices in the case of the Ceyhan Basin, *International Journal of Environment and Geoinformatics*, 8 (2), 113-125, DOI: 10.30897/ijegeo.792379.
- Dracup J.A., Lee K.S., Paulson E.G., 1980, On the definition of droughts, *Water Resources Research*, 16 (2), 297-302, DOI: 10.1029/WR016i002p00297.
- Eris E., Aksoy H., Onoz B., Cetin M., Yuce M.I., Selek B., Aksu H., Burgan H.I., Esit M., Yildirim I., Karakus E.U., 2019, Frequency analysis of low flows in intermittent and non-intermittent rivers from hydrological basins in Turkey, *Water Supply*, 19 (1), 30-39, DOI: 10.2166/ws.2018.051.
- Ganguli P., Reddy M.J., 2014, Evaluation of trends and multivariate frequency analysis of droughts in three meteorological subdivisions of western India, *International Journal of Climatology*, 34 (3), 911-928, DOI: 10.1002/joc.3742.
- Gocic M., Trajkovic S., 2013, Analysis of precipitation and drought data in Serbia over the period 1980-2010, *Journal of Hydrology*, 494, 32-42, DOI: 10.1016/j.jhydrol.2013.04.044.
- Helsel D.R., Hirsch R.M., Ryberg K.R., Archfield S.A., Gilroy E.J., 2002, *Statistical methods in water resources*, Techniques and Methods 4-A3, DOI: 10.3133/tm4A3.
- Houghton J.T., Meiro Filho L.G., Callander B.A., Harris N., Kattenburg A., Maskell K., 1996, *Climate Change 1995: The Science of Climate Change*, IPCC assessment report, available online <https://digitallibrary.un.org/record/223181> (data access 04.10.2022).
- Jaiswal R.K., Lohani A.K., Tiwari H.L., 2015, Statistical analysis for change detection and trend assessment in climatological parameters, *Environmental Processes*, 2 (4), 729-749, DOI: 10.1007/s40710-015-0105-3.
- Kampata J.M., Parida B.P., Moalafhi D.B., 2008, Trend analysis of rainfall in the headstreams of the Zambezi River Basin in Zambia, *Physics and Chemistry of the Earth. Parts A/B/C*, 33 (8-13), 621-625, DOI: 10.1016/j.pce.2008.06.012.
- Karabulut M., Gürbüz M.A., Korkmaz H., 2008, Precipitation and temperature trend analyses in Samsun, *Journal of International Environmental Application and Science*, 3 (5), 399-408.
- Kendall M.G., 1975, *Rank correlation methods*, 4th edition, Charles Griffin, London.
- Keskin M.E., Taylan D., Aslanbaş T., 2015, An investigation of water potential of Lake Eğirdir, Turkey, *Procedia Earth and Planetary Science*, 15, 244-248, DOI: 10.1016/j.proeps.2015.08.060.
- Kumar V., Jain S.K., 2010, Trends in seasonal and annual rainfall and rainy days in Kashmir Valley in the last century, *Quaternary International*, 212 (1), 64-69, DOI: 10.1016/j.quaint.2009.08.006.
- Lehmann E.L., D'Abbrera H.J., 1975, *Nonparametrics: Statistical methods based on ranks*, Springer, Oxford, 479 pp.
- Mann H.B., 1945, Nonparametric Tests Against Trend, *Econometrica*, 13 (3), 245-259, DOI: 10.2307/1907187.
- McKee T.B., Doesken N.J., Kleist J., 1993, The relationship of drought frequency and duration to time scales, [in:] 8th Conference on Applied Climatology, Anaheim, 17-22 January, 179-184.
- Palmer W.C., 1965, Meteorological drought, Research Paper No. 45, US Weather Bureau, Washington, DC.
- Palmer W.C., 1968, Keeping track of crop moisture conditions, nationwide: The new crop moisture index, *Weatherwise*, 21 (4), 156-161, DOI: 10.1080/00431672.1968.9932814.
- Pettitt A.N., 1979, A Non-parametric approach to the change-point problem, *Journal of the Royal Statistical Society. Series C: Applied Statistics*, 28 (2), 126-135, DOI: 10.2307/2346729.
- Piccarreta M., Capolongo D., Boenzi F., 2004, Trend analysis of precipitation and drought in Basilicata from 1923 to 2000 within a southern Italy context, *International Journal of Climatology*, 24 (7), 907-922, DOI: 10.1002/joc.1038.

- Santos C.A.C. dos, Neale C.M.U., Rao T.V.R., da Silva B.B., 2011, Trends in indices for extremes in daily temperature and precipitation over Utah, USA, *International Journal of Climatology*, 31 (12), 1813-1822, DOI: 10.1002/joc.2205.
- Sen P.K., 1968, Estimates of the regression coefficient based on Kendall's Tau, *Journal of the American Statistical Association*, 63 (324), 1379-1389, DOI: 10.1080/01621459.1968.10480934.
- Shafer B.A., Dezman L.E., 1982, Development of a surface water supply index (SWSI) to assess the severity of drought conditions in snowpack runoff areas, [in:] *Proceedings of the 50th Annual Western Snow Conference*, Reno, Nevada.
- Shi X., Xu X., 2008, Interdecadal trend turning of global terrestrial temperature and precipitation during 1951-2002, *Progress in Natural Science*, 18 (11), 1383-1393, DOI: 10.1016/j.pnsc.2008.06.002.
- Smadi M.M., Zghoul A., 2006, A sudden change in rainfall characteristics in Amman, Jordan during the mid 1950s, *American Journal of Environmental Sciences*, 2 (3), 84-91, DOI: 10.3844/ajesp.2006.84.91.
- Sneyers R., 1990, On the statistical analysis of series of observations, WMO Technical Note, 192 pp.
- Spinoni J., Naumann G., Carrao H., Barbosa P., Vogt J., 2014, World drought frequency, duration, and severity for 1951-2010, *International Journal of Climatology*, 34 (8), 2792-2804, DOI: 10.1002/joc.3875.
- Tabari H., Abghari H., Talaei P.H., 2012, Temporal trends and spatial characteristics of drought and rainfall in arid and semiarid regions of Iran, *Hydrological Processes*, 26 (22), 3351-3361, DOI: <https://doi.org/10.1002/hyp.8460>.
- Tallaksen L., van Lanen H.A.J., 2004, *Hydrological drought. Processes and estimation methods for streamflow and groundwater*: Elsevier.
- Tate E.L., Gustard A., 2000, Drought definition: A hydrological perspective, [in:] *Drought and Drought Mitigation in Europe*, J.V. Vogt, F. Somma (eds.), Springer Netherlands, Dordrecht, 23-48, DOI: 10.1007/978-94-015-9472-1_3.
- Tosunoglu F., Kisi O., 2016, Joint modelling of annual maximum drought severity and corresponding duration, *Journal of Hydrology*, 543, 406-422, DOI: 10.1016/j.jhydrol.2016.10.018.
- Uzunkol M., Kızılelma Y., 2016, Determination of drought status and trends in the Ceyhan Basin. *The Journal of Academic Social Sciences*, 29 (4), 503-519, DOI: 10.16992/ASOS.1258.
- Vezzoli R., Pecora S., Zenoni E., Tonelli F., 2012, Data Analysis to Detect Inhomogeneity, Change Points, Trends in Observations: An Application to Po River Discharge Extremes, CMCC Research Paper No. 138.
- Villarini G., Serinaldi F., Smith J.A., Krajewski W.F., 2009, On the stationarity of annual flood peaks in the continental United States during the 20th century, *Water Resources Research*, 45 (8), DOI: 10.1029/2008WR007645.
- Wald A., Wolfowitz J., 1940, On a test whether two samples are from the same population, *The Annals of Mathematical Statistics*, 11 (2), 147-162.
- Wallis W.A., Moore G.H., 1941, A Significance Test for Time Series and Other Ordered Observations, National Bureau of Economic Research.
- Wilhite D.A., Glantz M.H., 1985, Understanding: the drought phenomenon: The role of definitions, *Water International*, 10 (3), 111-120, DOI: 10.1080/02508068508686328.
- Xu Y., Lin S., Huang Y., Zhang Q., Ran Q., 2011, Drought analysis using multi-scale standardized precipitation index in the Han River Basin, China, *Journal of Zhejiang University-SCIENCE A*, 12 (6), 483-494, DOI: 10.1631/jzus.A1000450.
- Yu P.-S., Yang T.-C., Kuo C.-C., 2006, Evaluating long-term trends in annual and seasonal precipitation in Taiwan, *Water Resources Management*, 20 (6), 1007-1023, DOI: 10.1007/s11269-006-9020-8.
- Yu Y.-S., Zou S., Whittemore D., 1993, Non-parametric trend analysis of water quality data of rivers in Kansas, *Journal of Hydrology*, 150 (1), 61-80, DOI: 10.1016/0022-1694(93)90156-4.
- Yuce M.I., Esit M., Ercan B., 2018, A relationship between flow discharges, sediment discharge and sub-basin areas in Ceyhan Catchment, [in:] *13th International Congress on Advances in Civil Engineering*, 12-14 September, Izmir.
- Yuce M.I., Esit M., Kalaycioglu V., 2022, Investigation of trends in extreme events: a case study of Ceyhan Basin, Turkey, *Journal of Applied Water Engineering and Research*, DOI: 10.1080/23249676.2022.2113462.
- Yuce M.I., Esit M., Karatas M.C., 2019, Hydraulic geometry analysis of Ceyhan River, Turkey, *SN Applied Sciences*, 1 (7), 763, DOI: 10.1007/s42452-019-0800-1.

- Yuce M.I., Esit M., Muratoglu A., 2015, Determining the hydraulic geometry parameters of Seyhan River, American Journal of Engineering, Technology and Society, 2 (4), 77-84.
- Zhang Y., Cai W., Chen Q., Yao Y., Liu K., 2015, Analysis of changes in precipitation and drought in Aksu River Basin, Northwest China, Advances in Meteorology, DOI: 10.1155/2015/215840.
- Zhong A.H., Li Y.Q., 2009, Spatial and temporal distribution characteristics and variation tendency of precipitation in Mianyang, Sichuan Province, Plateau and Mountain Meteorology Research, 29 (4), 63-69.

Identification of nominal release policies implemented in a multi-purpose water reservoir

Koichi Unami 

Kyoto University, Graduate School of Agriculture

Rasha M Fadhil 

University of Mosul, College of Engineering

Md Kamal Rowshon, Ahmad Fikri, Wayayok Aimrun

Universiti Putra Malaysia, Faculty of Engineering

Abstract

A water reservoir's operation should follow a rational policy to ensure adequate water provision for different purposes without adverse effects. However, it is not well-studied how to identify operational policies currently being implemented. This study establishes a new approach to identifying nominal release policies as implemented in a multi-purpose water reservoir. We chose Bukit Merah Reservoir (BMR), located in Perak State, Malaysia, as a study site to examine its release policies for meeting irrigation, municipal, and industrial water demands and for mitigating floods and environmental hazards. The operator of BMR releases the reservoir's water into two primary irrigation canals, the Main Canal and the Selinsing Canal. Generalized additive models (GAMs) are applied to time series data observed at BMR to identify the annual dynamics of its water management. Operational policies for the release discharges into the two primary irrigation canals are assumed to be based on information on the time-of-year and the reservoir water level. First, a backfitting algorithm identifies each contributing function of the GAMs representing the release policies. Then, spurious oscillations in the functions are removed by total variation (TV) regularization (TVR) to obtain nominal release policies, which are quite reasonable in the sense of conventional reservoir management practice. Finally, the identified nominal release policies are utilized to examine shifts in the operation of BMR during the period from 2000 through 2011. The decomposition of release policies illustrates the two aspects of the irrigation demand's annual patterns and the hydraulic structures' functions. The spurious oscillations removed by TVR are considered to represent indecision by the reservoir operator.

Keywords

Reservoir operation, policy identification, generalized additive model, total variation regularization, Bukit Merah Reservoir.

Submitted 5 May 2022, revised 19 June 2022, accepted 15 September 2022

DOI: 10.26491/mhwm/154592

1. Introduction

In recent decades, climate change and socio-economic growth have had impacts on available water resources and food security in most parts of the world (Biemans et al. 2013; Lee, Bae 2015). Thus, more sophisticated management of existing water resources (Mereu et al. 2016; Wałęga et al. 2020), environments (Alam et al. 2018), and ecosystems (Yaegashi et al. 2018) is required to adapt to the impacts. A water reservoir's operation should follow a rational policy to ensure adequate water provision for its various intended purposes without adverse effects. Figure 1 shows a conceptual diagram of a typical reservoir operation system in the context of feedback control theory. Hydrologic inputs, including precipitation, evapotranspiration, and runoff from the catchment, affect the reservoir's water balance and the water supply to the command area (i.e. the downstream area serviced by the reservoir's functions). The release from the reservoir as a control variable also contributes to the reservoir's water balance and the

water supply to the command area. The operator's role is to implement a policy determining the release discharges based on the reservoir's water level and the water demand from the command area. However, a more sophisticated system of reservoir operation might also account for hydrologic inputs and/or possible conveyance losses as parts of the information on which the policy is based.

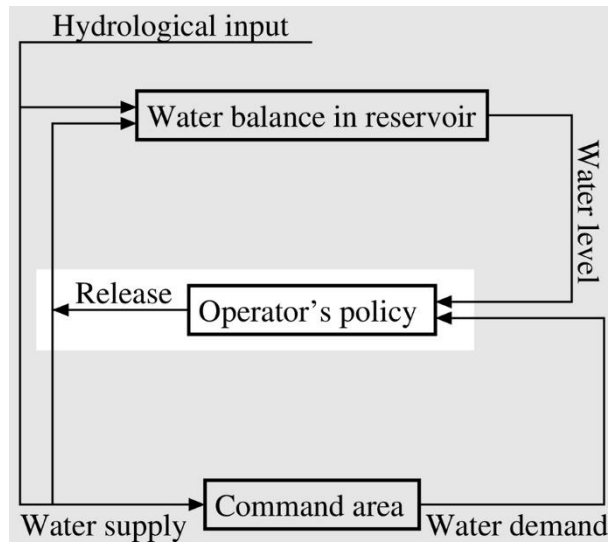


Fig. 1. Conceptual block diagram of a reservoir operation system.

Labadie (2004), Rani and Moreira (2010), and Ahmad et al. (2014) reviewed a variety of methods for computationally determining suitable reservoir operation policies. Stochastic dynamic programming (SDP) theory is the general framework to establish reservoir operation policies, as explored decades ago (Heidari et al. 1971; Tejada-Guibert et al. 1993, 1995; Yakowitz 1982). The SDP typically provides optimal operation policies with thresholds of opening valves or switching pumps (Nop et al. 2021; Unami, Mohawesh 2018; Unami et al. 2019b). However, reservoir operators generally do not accept such theoretically generated policies but instead rely on their empirical knowledge to make decisions when unexpected risks are involved (El-Shafie et al. 2014). Therefore, attention should be paid to the actual policies that may be identified from historical data (Giuliani et al. 2014). Turner et al. (2021) firstly attempted to inventory reservoir operation policies in the United States.

This study aims at establishing a new approach to identifying nominal release policies implemented in a multi-purpose water reservoir. Bukit Merah Reservoir (BMR), located in the northern part of Perak State, Malaysia, was chosen as a study site. The water levels and release discharges of BMR were recorded daily from 2000 through 2011. Generalized additive models (GAMs; Chen, Tsay 1993) are applied for representing the operational policies for release discharges, which are assumed to have an annual period based on the day of the year and the water levels (Unami et al. 2019a). The backfitting algorithm works well to identify each contributing function of the GAMs (Breiman, Friedman 1985). However, the release policies identified with that method include spurious oscillations, which are removed with total variation regularization (TVR), known as the Rudin–Osher–Fatemi model (ROF) for the initials of its three authors (Rudin et al. 1992). The ROF model contains a scale parameter dominating the discrepancy of the

reconstructed data from the original data that includes spurious oscillations (Osher et al. 2005). Further application of TVR in agricultural water management was discussed in Fadhil and Unami (2021). The identified release policies, which are considered nominal because they have been smoothed and regularized, are utilized to examine shifts in the operation of BMR during the period. Several factors stemming from climate change and socio-economic growth are inferred to have burdened the operation of BMR with more demanding release policies.

2. Materials and methods

2.1. Study site and datasets

Figure 2 shows the topography of BMR's catchment and command areas, extracted from the Shuttle Radar Topography Mission (SRTM) digital elevation data (Farr et al. 2007), with the boundaries of sub-catchments demarcated with white lines. The climatic zone is tropical rainforest with a mean annual rainfall of more than 3000 mm. The bimodal annual rainfall pattern enables paddy rice cultivation twice a year. BMR has a catchment area of 480 km²; it supplies irrigation water to the paddy fields of the Kerian Irrigation Scheme (KIS), covering an area of 236 km², and urban water for municipal and industrial purposes to the Kerian, Larut, Matang, and Selama Districts. The catchment includes four river systems: Merah, Jelutong, Selarong, and Kurau Rivers (Ismail, Najib 2011), located between 04 51 N and 05 10 N latitude and 100 38 E to 101 00 E longitude. The region is primarily rural with numerous riverine villages established along the middle and lower reaches of the rivers. The land use in the areas with elevations lower than 50 m is predominantly for tree plantations such as oil palm, rubber, and coconut. At the same time, the surrounding steep mountain slopes are covered with rainforests. The rainfall characteristics in the catchment area have been modeled with a stochastic generator (Fadhil et al. 2017). Analysis using rainfall-runoff models with fractional derivatives has shown that the hydrologic response in the catchment area of the Kurau River is unstable (Unami et al. 2021). The KIS's 236 km² command area consists of low-lying lands between the Strait of Malacca and BMR. Two primary irrigation canals, the Main Canal and the Selinsing Canal, convey the irrigation water by gravity. The urban water is taken from the Selinsing Canal at a pumping station located 6.5 km downstream of BMR. Dor et al. (2011) conducted a detailed hydro-geological study on the Selinsing Canal. Approximately 61% of water consumed in the paddy fields of the KIS originates from BMR, and the rest is from rainfall (Hamidon et al. 2015). Urban demand depends on the local population and its economy. The Department of Irrigation and Drainage (DID, 2011) projected that the growth rates of the population and economy in the state of Perak would decrease but remain positive until the year 2050. Intensive research on the operation of BMR has been conducted in the context of future climate change and SDP (Fadhil 2018). Besides the irrigation and urban demands, the operation of BMR needs to account for flood control and environmental hazards. There are two gated spillways of Ogee weir type with the same crest level, draining water from BMR to the original water course of the Kurau River, which meanders through the KIS with widths of 30-50 m.

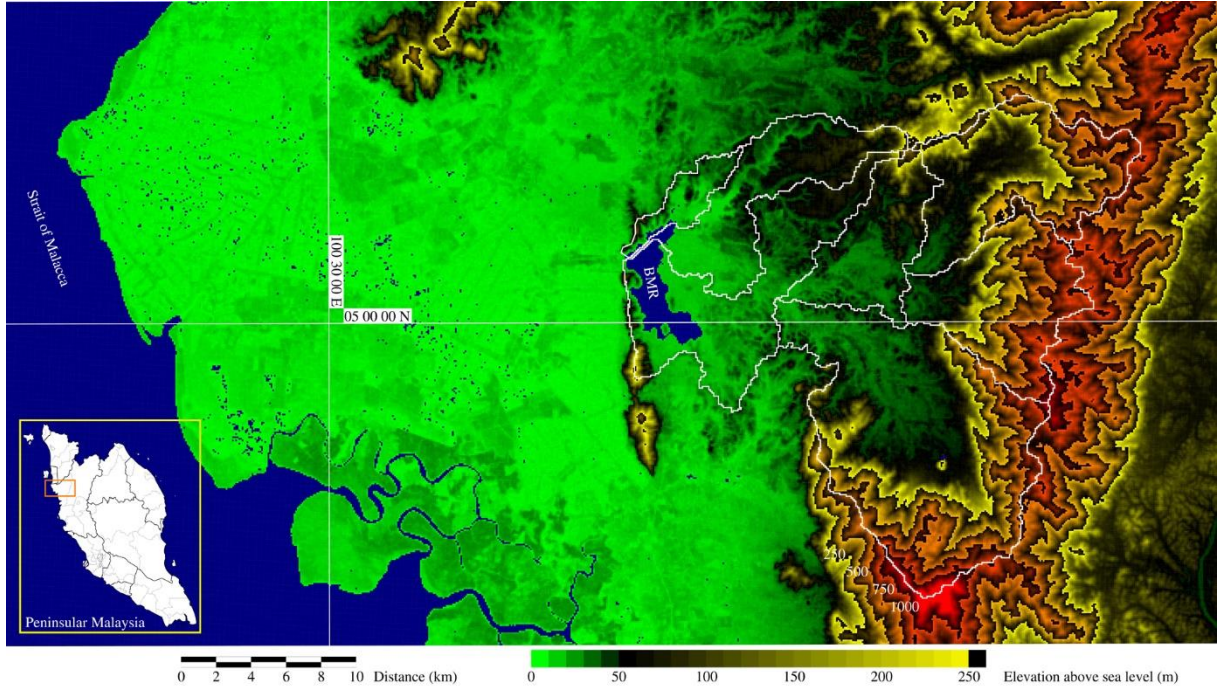


Fig. 2. The topography of the catchment and command areas of BMR, located in Peninsular Malaysia.

The key dimensional parameters of BMR are summarized in Table 1. The dam embankment is at an elevation above the sea level (EL) of 11.28 m. The datum level is taken as the lowest level of the reservoir. The water level above the sea level is denoted by h (m). The storage volume of the reservoir when the water level is equal to h is denoted by $V(h)$. The maximum capacity of the spillways at MWL is 565 m³/s. However, the bed slope of the Kurau River receiving the water from the spillways is about 1/10,000, implying insufficient discharge capacity.

Table 1. Key dimensional parameters of BMR.

Parameter	Description
Maximum water level (MWL) H (m)	EL 10.25
Flood control level (FCL) η_F (m)	EL 9.75
Normal water level (NWL) η_N (m)	EL 8.69
Spillway crest level (SCL) η_S (m)	EL 8.14
Intake gate crest level (IGL) η_G (m)	EL 6.10
Datum level η_0 (m)	EL 2.00
Storage volume (10 ⁶ m ³)	$V(h) = 0.190 (h - \eta_0)^{3.17}$

A daily log of the operation of BMR in terms of water levels, rainfall depths, and release discharges into the two primary irrigation canals for the period from 2000 through 2011 was provided from the DID. The complete source data are available in a supporting information file.

Hamidon et al. (2015) estimated the irrigation demand Q_{irr} in the KIS for each month. The urban demand Q_{urb} was assumed to be constant at 1.70 m³/s (Anwar 2010). Then, the sum of the irrigation demand Q_{irr} and the constant urban demand Q_{urb} becomes the total demand discharge Q_D for each month. Table 2 summarizes the average monthly rainfall depths R during 2000-2011, the values of Q_{irs} , Q_{urb} , and Q_D , and

the observed average monthly release discharge Q_R . However, it is noteworthy that the actual irrigation demand varies on a daily scale, according to the GIS-based estimation by Rowshon et al. (2003a-b).

Table 2. Monthly parameter values relevant to the water balance of BMR.

Parameter	Jan	Feb	Mar	Apr	May	Jun	Jul	Aug	Sep	Oct	Nov	Dec
Rainfall depth R (mm)	243.0	174.8	294.3	305.5	155.0	163.1	170.3	215.6	296.9	406.3	356.6	266.8
Irrigation demand Q_{irr} (m ³ /s)	11.35	0.39	13.99	15.63	14.95	13.63	10.12	0.35	11.54	12.23	12.54	12.84
Urban demand Q_{urb} (m ³ /s)	1.70	1.70	1.70	1.70	1.70	1.70	1.70	1.70	1.70	1.70	1.70	1.70
Total demand Q_D (m ³ /s)	13.05	2.09	15.69	17.33	16.65	15.33	11.82	2.05	13.24	13.93	14.24	14.54
Observed average release discharge Q_R (m ³ /s)	5.74	4.18	24.07	28.91	27.18	13.86	4.06	2.79	23.32	29.88	28.52	14.92

2.2. Generalized additive models for release discharges

The water level of BMR at the beginning of day t is denoted by h_t . The release discharge into the primary irrigation canal k on the day t of the year y is denoted by $Q_{y,t}^k$. Here, $k=0$ and $k=1$ indicate the Main Canal and the Selinsing Canal, respectively. It is assumed that the operator's nominal policy $u^k(t, h_t)$ for release discharge into canal k , based on the information of t and h_t , is yearly invariant. We introduce an additive decomposition structure into $u^k(t, h_t)$ to write it as a GAM:

$$u^k(t, h_t) = f_{time}^k(t) + f_{WL}^k(h_t) + C^k \quad (1)$$

where f_{time}^k and f_{WL}^k are functions that may be nonlinear, and C^k is a constant. Representing the day t as:

$$t = 2\pi \frac{\text{The day of the year} - 1}{\text{The number of days in the year}}, \quad (2)$$

the function f_{time}^k is assumed to be 2π -periodic. The objective here is to determine the functions f_{time}^k and f_{WL}^k minimizing the errors:

$$\varepsilon_{y,t}^k = Q_{y,t}^k - u^k(t, h_t) \quad (3)$$

in the sense of the least squares as well as the TV.

2.3. Backfitting algorithm

Firstly, the backfitting algorithm is applied for finding the functions to minimize the expected square error $E[\varepsilon_{t,y}^k]^2$ for all the observed data. The algorithm iteratively updates smoothing estimates \hat{f}_{time}^k and \hat{f}_{WL}^k of f_{time}^k and f_{WL}^k , respectively. Histograms φ_{time}^k and φ_{WL}^k are defined as:

$$\varphi_{time}^k(l) = \frac{1}{|\Omega_t(l)|} \sum_{t \in \Omega_t(l)} \hat{f}_{time}^k(t), \quad \Omega_t(l) = \left\{ t \mid t \in \left(l\Delta t - \frac{\Delta t}{2}, l\Delta t + \frac{\Delta t}{2} \right] \right\} \quad (4)$$

and

$$\varphi_{WL}^k(l) = \frac{1}{|\Omega_h(l)|} \sum_{h_t \in \Omega_h(l)} \hat{f}_{WL}^k(h_t), \quad \Omega_h(l) = \left\{ h_t \mid h_t \in \left(l\Delta h - \frac{\Delta h}{2}, l\Delta h + \frac{\Delta h}{2} \right] \right\} \quad (5)$$

for integers l with the increments Δt and Δh , respectively. Then, with initial guesses $\hat{f}_{time}^k = \hat{f}_{WL}^k = \mathbf{0}$ for all t and h_t , the histograms are utilized to update the smoothing estimates as:

$$\hat{f}_{time}^k(t) = Q_{y,t}^k - \varphi_{WL}^k(l) - C^k, \quad t \in \left(l\Delta t - \frac{\Delta t}{2}, l\Delta t + \frac{\Delta t}{2} \right] \quad (6)$$

and

$$\hat{f}_{WL}^k(h_t) = Q_{y,t}^k - \varphi_{time}^k(l) - C^k, \quad h_t \in \left(l\Delta h - \frac{\Delta h}{2}, l\Delta h + \frac{\Delta h}{2} \right] \quad (7)$$

where C^k are taken as the averages of all $Q_{y,t}^k$. This algorithm is known to converge under appropriate conditions.

2.4. TVR

After the backfitting algorithm has converged, the TVR is applied to each \hat{f}_{time}^k and \hat{f}_{WL}^k to remove spurious oscillations. The TVR operated for a generic oscillating function f over a domain Ω of x minimizes the functional J of u :

$$J = \int_{\Omega} |\nabla u| d\Omega + \frac{\lambda}{2} \int_{\Omega} |u - f|^2 d\Omega \quad (8)$$

where λ is the scale parameter of the ROF model, and $\nabla = \partial/\partial x$. The Euler-Lagrange equation for minimization of J in (8) is formally written as:

$$\nabla \cdot \left(\frac{\nabla u}{|\nabla u|} \right) + \lambda(f - u) = 0. \quad (9)$$

We attempt to obtain an approximate solution to (9) by numerically solving the initial value problem of the singular diffusion equation:

$$\frac{\partial u}{\partial t} = \nabla \cdot \left(\frac{\nabla u}{|\nabla u|} \right) + \lambda(f - u), \quad u = f \text{ at } t = 0 \quad (10)$$

It is assumed that the values of f are determined at n different points of Ω . Let those points be x_i for $i = 0, 1, \dots, n-1$ such that $x_0 < x_1 < \dots < x_{n-1}$. Applying the standard Galerkin finite element scheme with piecewise linear bases to (10) results in the initial value problem of the ordinary differential equation:

$$\frac{d\mathbf{u}}{dt} = M^{-1}A\boldsymbol{\sigma} + \lambda(\mathbf{f} - \mathbf{u}), \quad \mathbf{u} = \mathbf{f} \text{ at } t = 0 \quad (11)$$

where $\mathbf{u} \in \mathbb{R}^n$ is the vector whose i^{th} entry is \hat{u}_i , which is the approximation of u at x_i , $\mathbf{f} \in \mathbb{R}^n$ is the vector whose i^{th} entry is f at x_i , $\boldsymbol{\sigma} \in \mathbb{R}^{n-1}$ is the vector whose i^{th} entry is the sign of $\hat{u}_{i+1} - \hat{u}_i$, $M \in \mathbb{R}^{n \times n}$ is the mass matrix, and $A \in \mathbb{R}^{n \times (n-1)}$ is the stiffness matrix. Two types of boundary conditions are considered: periodic and Neumann. For the periodic boundary condition, the matrices become:

$$M = \begin{pmatrix} \frac{x_1 - x_{n-1}}{3} & \frac{x_1 - x_0}{6} & 0 & \dots & \dots & 0 & \frac{x_0 - x_{n-1}}{6} \\ \frac{x_1 - x_0}{6} & \frac{x_2 - x_0}{3} & \frac{x_2 - x_1}{6} & \ddots & \ddots & \ddots & 0 \\ 0 & \ddots & \ddots & \ddots & 0 & \ddots & \vdots \\ \vdots & \ddots & \frac{x_i - x_{i-1}}{6} & \frac{x_{i+1} - x_{i-1}}{3} & \frac{x_{i+1} - x_i}{6} & \ddots & \vdots \\ \vdots & \ddots & 0 & \ddots & \ddots & \ddots & 0 \\ 0 & \ddots & \ddots & \ddots & \frac{x_{n-2} - x_{n-3}}{6} & \frac{x_{n-1} - x_{n-3}}{3} & \frac{x_{n-1} - x_{n-2}}{6} \\ \frac{x_0 - x_{n-1}}{6} & 0 & \dots & \dots & 0 & \frac{x_{n-1} - x_{n-2}}{6} & \frac{x_0 - x_{n-2}}{3} \end{pmatrix} \quad (12)$$

and

$$A = \begin{pmatrix} 1 & 0 & \dots & 0 & -1 \\ -1 & \ddots & \ddots & \ddots & 0 \\ 0 & \ddots & 1 & \ddots & \vdots \\ \vdots & \ddots & -1 & \ddots & 0 \\ 0 & \ddots & \ddots & \ddots & 1 \\ 1 & 0 & \dots & 0 & -1 \end{pmatrix} \quad (13)$$

For the Neumann boundary condition, the matrices become:

$$M = \begin{pmatrix} \frac{x_1 - x_0}{6} & \frac{x_1 - x_0}{6} & 0 & \dots & \dots & 0 & 0 \\ \frac{x_1 - x_0}{6} & \frac{x_2 - x_0}{3} & \frac{x_2 - x_1}{6} & \ddots & \ddots & \ddots & 0 \\ 0 & \ddots & \ddots & \ddots & 0 & \ddots & \vdots \\ \vdots & \ddots & \frac{x_i - x_{i-1}}{6} & \frac{x_{i+1} - x_{i-1}}{3} & \frac{x_{i+1} - x_i}{6} & \ddots & \vdots \\ \vdots & \ddots & 0 & \ddots & \ddots & \ddots & 0 \\ 0 & \ddots & \ddots & \ddots & \frac{x_{n-2} - x_{n-3}}{6} & \frac{x_{n-1} - x_{n-3}}{3} & \frac{x_{n-1} - x_{n-2}}{6} \\ 0 & 0 & \dots & \dots & 0 & \frac{x_{n-1} - x_{n-2}}{6} & \frac{x_{n-1} - x_{n-2}}{6} \end{pmatrix} \quad (14)$$

and

$$A = \begin{pmatrix} 1 & 0 & \dots & 0 & 0 \\ -1 & \ddots & \ddots & \ddots & 0 \\ 0 & \ddots & 1 & \ddots & \vdots \\ \vdots & \ddots & -1 & \ddots & 0 \\ 0 & \ddots & \ddots & \ddots & 1 \\ 0 & 0 & \dots & 0 & -1 \end{pmatrix}. \quad (15)$$

3. Results

3.1. Identification of nominal release policies and reconstruction of release discharges

Two five-year subperiods, 2001-2005 and 2007-2011, were extracted from the whole period 2000-2011. Consecutive use of the backfitting algorithm and the TVR identified nominal release policies from the observed release discharges during each of the two subperiods. The increments are chosen as $\Delta t = \frac{2\pi}{365.25}$ (rad) and $\Delta h = 0.01$ (m). Five cases of the scale parameter $\lambda = 10^{-i/2}$ ($i = 0, 1, 2, 3, 4$) are considered. The numerical solution of the initial value problem (10) successfully converges to a steady state for each case of λ . Figures 3 and 4 compare the processes of TVR applied to f_{time}^0 for the Main Canal during the two subperiods 2001-2005 and 2007-2011. Figures 5 and 6 compare the processes of TVR applied to f_{WL}^0 for the Main Canal during the two subperiods. The value of C^0 , which is equal to the average of all release discharges to the Main Canal, is 12.01 and 15.60 for the subperiods 2001-2005 and 2007-2011, respectively. Then, release discharges to the Main Canal are reconstructed with the nominal release policies identified from the observed data during the two subperiods, as shown in Figures 7 and 8. For example, with $\lambda = 10^{-2}$, Figures 3 and 5 indicate that the values of f_{time}^0 and f_{WL}^0 are -8.29 and -0.28 , respectively, if the water level is at SCL (EL 8.14) on January 1st during the subperiod 2001-2005. In that case, the nominal release discharge becomes equal to $f_{time}^0 + f_{WL}^0 + C^0 = -8.29 - 0.28 + 12.01 =$

3.44 (m³/s). Figures 9-13 show the results similarly computed for the Selinsing Canal as in Figure 3 through Figure 8 for the Main Canal. The value of C^1 , which is equal to the average of all release discharges to the Selinsing Canal, is 6.32 and 6.86 for the subperiods 2001-2005 and 2007-2011, respectively.

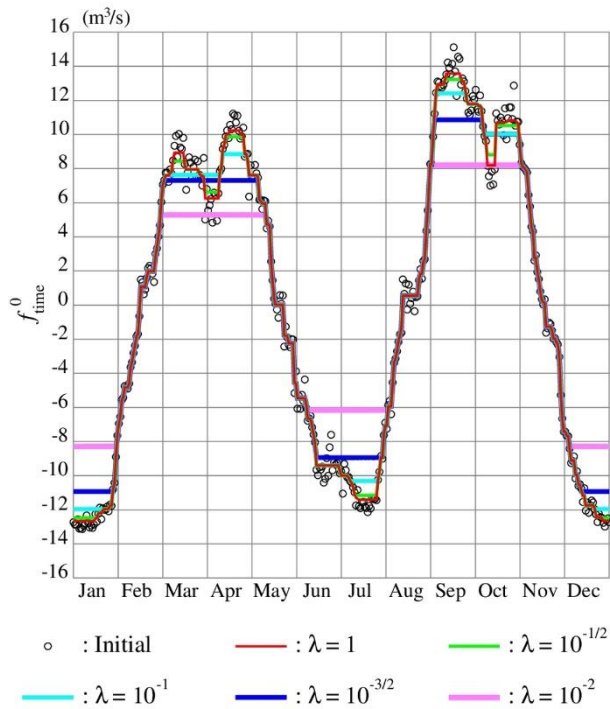


Fig. 3. The process of TVR applied to the function of time for the Main Canal during the subperiod 2001-2005.

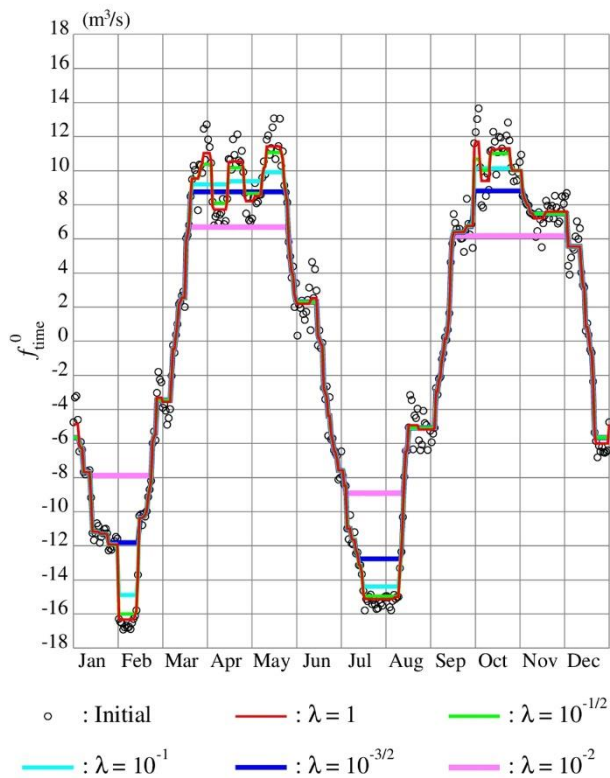


Fig. 4. The process of TVR applied to the function of time for the Main Canal during the subperiod 2007-2011.

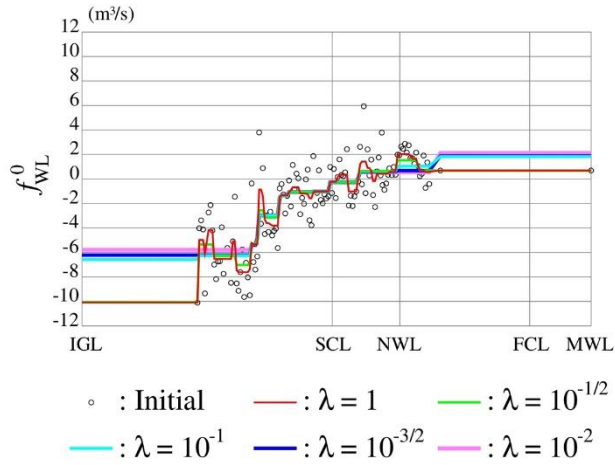


Fig. 5. The process of TVR applied to the function of WL for the Main Canal during the subperiod 2001-2005.

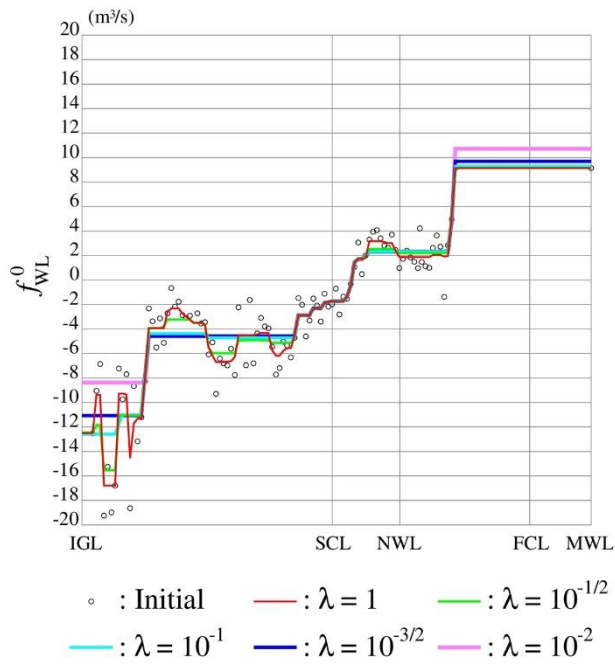


Fig. 6. The process of TVR applied to the function of WL for the Main Canal during the subperiod 2007-2011.

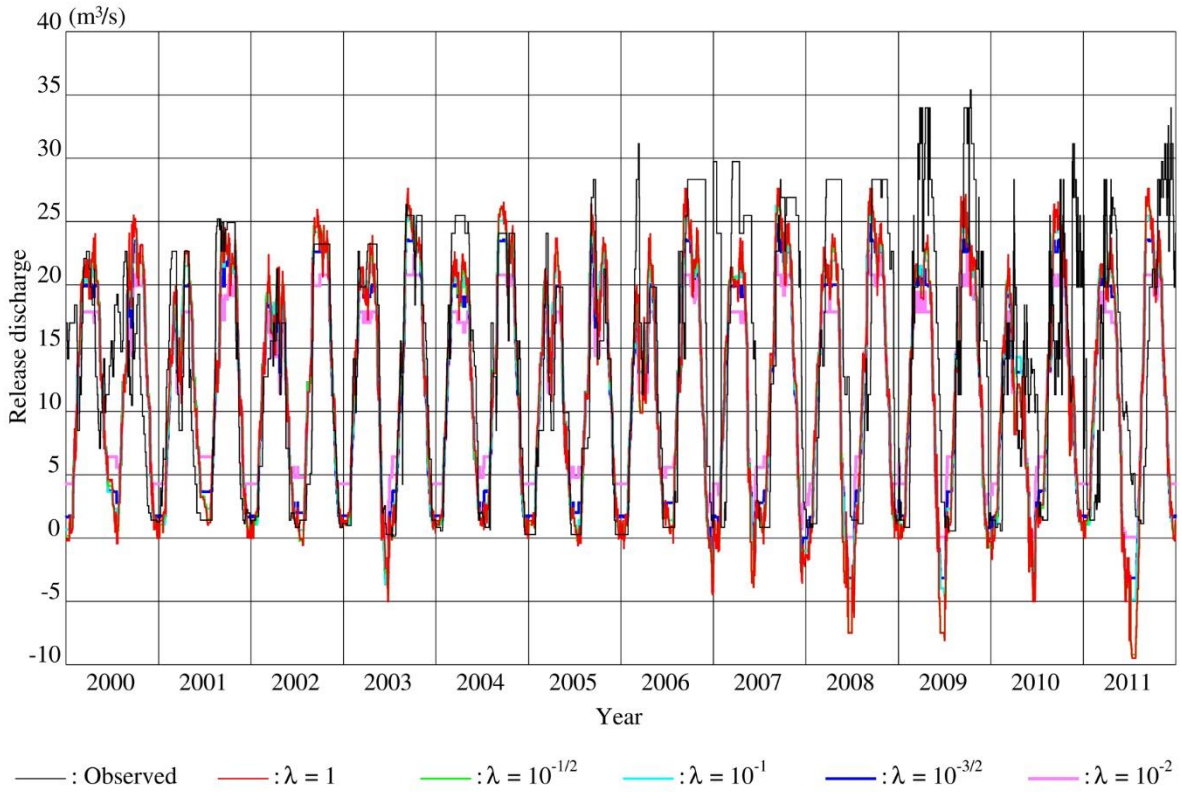


Fig. 7. Reconstructed release discharges to the Main Canal with the 2001-2005 policies.

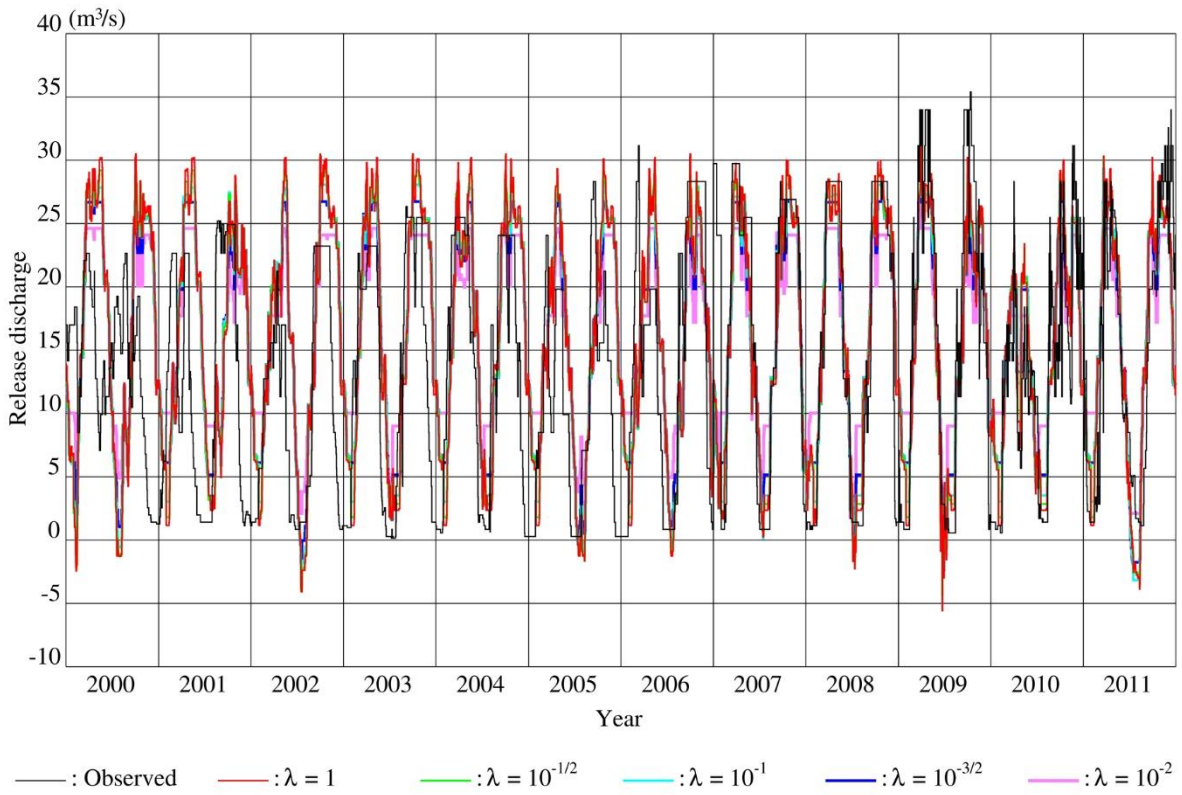


Fig. 8. Reconstructed release discharges to the Main Canal with the 2007-2011 policies.

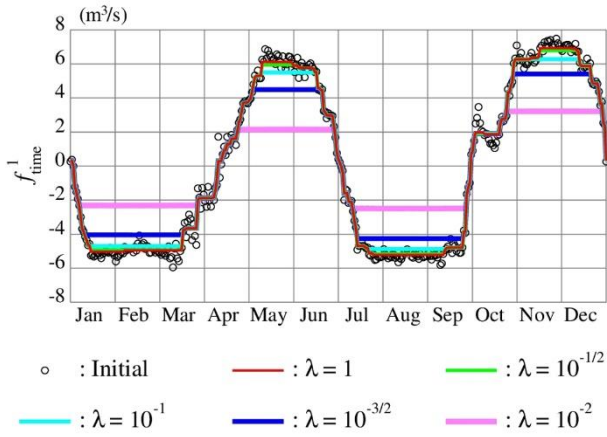


Fig. 9. The process of TVR applied to the function of time for the Selinsing Canal during the subperiod 2001-2005.

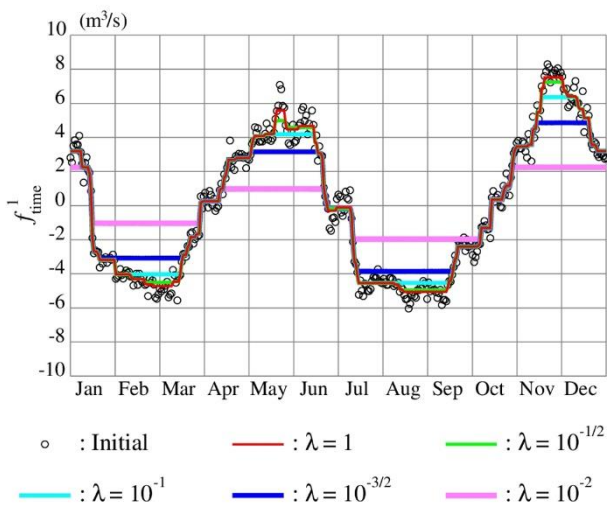


Fig. 10. The process of TVR applied to the function of time for the Selinsing Canal during the subperiod 2007-2011.

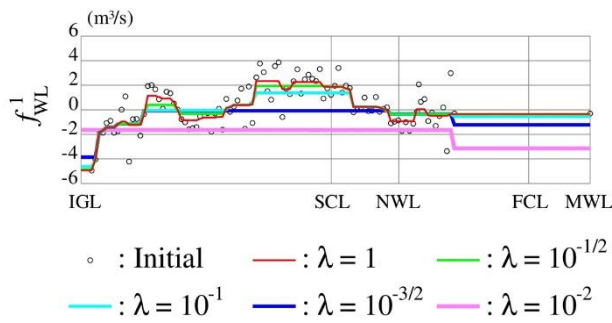


Fig. 11. The process of TVR applied to the function of WL for the Selinsing Canal during the subperiod 2001-2005.

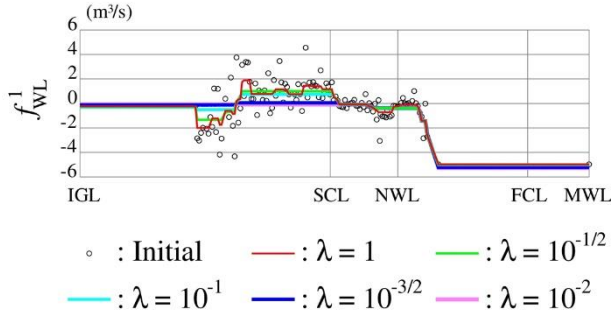


Fig. 12. The process of TVR applied to the function of WL for the Selinsing Canal during the subperiod 2007-2011.

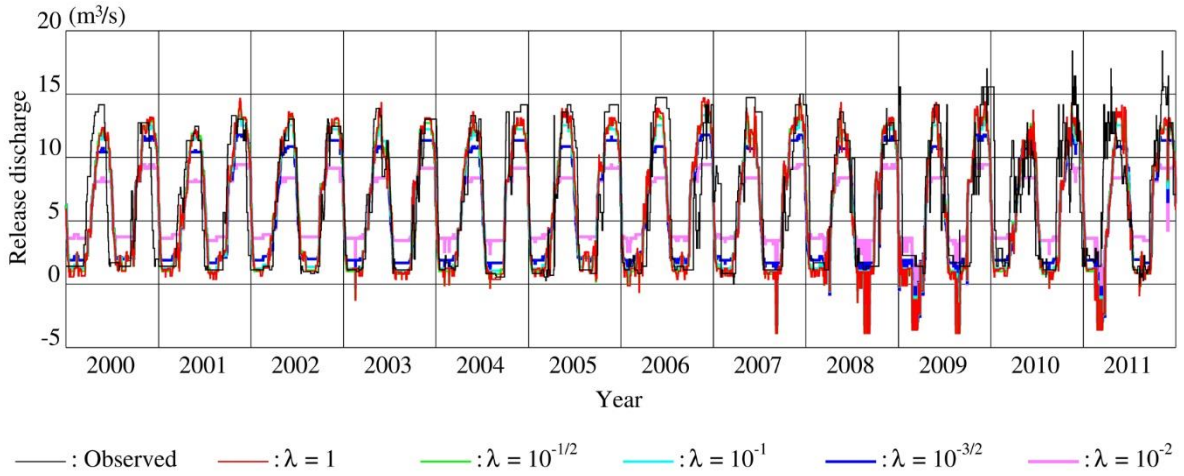


Fig. 13. Reconstructed release discharges to the Selinsing Canal with the 2001-2005 policies.

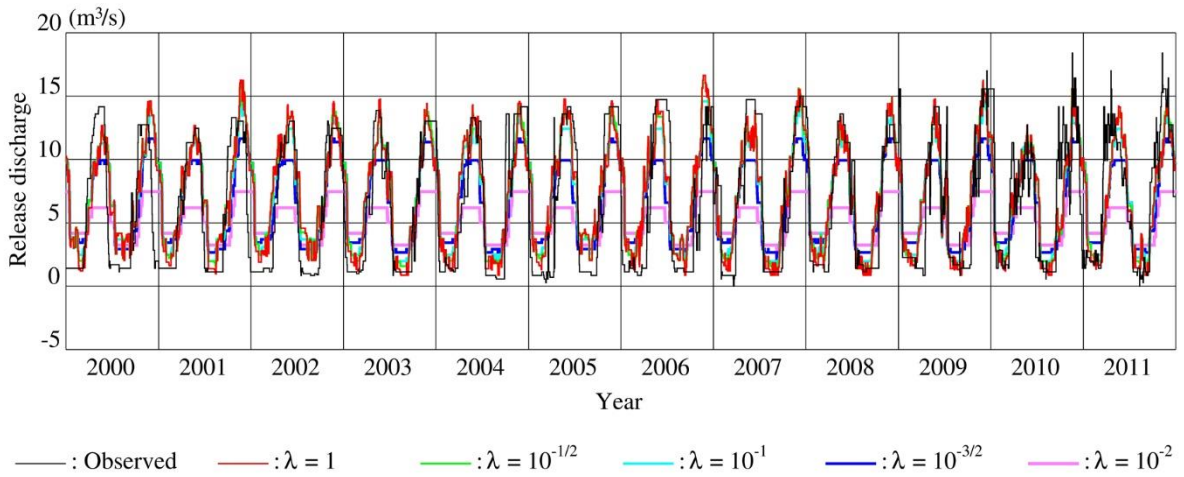


Fig. 14. Reconstructed release discharges to the Selinsing Canal with the 2007-2011 policies.

3.2. Choice of the scale parameter

The daily oscillations in \hat{f}_{time}^k and \hat{f}_{WL}^k are successfully removed with TVR, while the discrepancy of f_{time}^k and f_{WL}^k from them becomes large as the scale parameter λ becomes small. The TV in the reconstructed release discharges tends to decrease for smaller λ . Under the assumption that the release policies are based

on the information of t and h_b the nominal release policies identified by the large-scale parameter $\lambda = 1$, are well representative of t and h_b , and thus, considered the most reasonable and realistic.

4. Discussions

4.1. Comparison of the two subperiods

The comparison between the observed and the reconstructed release discharges during the whole period validates the release policies identified from the data during each of the two subperiods. Significant increases in the peaks and the TV of the observed release discharges in both canals can be seen in 2009-2011. Consequently, the reconstructed release discharges with the 2001-2005 policies barely approximate the observed ones in 2009-2011. This indicates that the operator changed the release policies from the subperiod 2001-2005 to the subperiod 2007-2011.

Referring again to Figure 1, the variable hydrological input, which is under the considerable influence of climate change, is considered the primary cause of changes in the release policies controlling the water balance in the reservoir to satisfy the water demand.

The changes in the functions f_{time}^k from the subperiod 2001-2005 to the subperiod 2007-2011 imply the shifts in the actual irrigation demand's annual patterns, which are susceptible to rapidly developing agronomic practices such as the choice of varieties to adapt the climate change and to meet the increasing food demand. In the Main canal ($k = 0$), the two peaks of early-March through early-May and early-September through late-October shifted to mid-March through late-May and mid-September through early-December, respectively. In the Selinsing canal ($k = 1$), the two peaks of early May through late June and late October through late December shifted to mid-April through mid-June and early-November through mid-January, respectively. As a result, May became the most critical month in the subperiod 2007-2011, having the least rainfall and the overlapping peaks of the release discharges in the two primary irrigation canals. This increasing criticality of May in the water balance of BMR supports the simulation-based prediction by Hamidon et al. (2015). Furthermore, it is noteworthy that the change in rainfall patterns between the two subperiods in the catchment area of BMR is just a symptom of catastrophic regime shifts in the coming decades, according to the recent climatological studies using GCMs (Adib et al. 2020; Adib, Harun 2022; Adib et al. 2022).

The function f_{WL}^0 for the Main canal is mostly monotone increasing with respect to h_b , and its increment was amplified from the subperiod 2001-2005 to the subperiod 2007-2011. The function f_{WL}^1 for the Selinsing canal was small for the higher water levels during the subperiod 2001-2005 but became not so much during the subperiod 2007-2011. In other words, the two primary irrigation canals became more utilized for draining excess water from BMR in the subperiod 2007-2011 than in the subperiod 2001-2005. This allocation of the two primary irrigation canals for the drainage purpose might be attributed to the small capacity of Kurau River, which cannot manage the discharges required for reasonable flood control.

4.2. Comparison with other approaches

The first key feature of the approach developed here is to decompose a release policy into possibly singular functions of a single independent variable with the additive structure, unlike the standard procedure identifying release policies as quite regular functions of multiple independent variables (Turner et al. 2021). As discussed in the previous subsection, the decomposition of release policies illustrates the two aspects of the irrigation demand's annual patterns and the hydraulic structures' functions.

The second key feature is the TVR applied to the decomposed possibly singular functions, breaking through a widespread obsession that policy identification is “to minimize some distance metric between historical releases and modeled ones,” as in Giuliani et al. (2014). This study is the first to succeed in quantitatively treating the indecisive attitude of a reservoir operator as the spurious oscillations to be removed with the TVR. The release policies extracted with the TVRs are the nominal parts. Overgaard (2019) provides mathematical proof to endorse the ROF model in one dimension used in this study for TVR. However, the lack of an established method to choose the best scale parameter λ is a practical limitation of this approach. A follow-up study shall be conducted to validate the λ values with the empirical knowledge of the reservoir operator.

A sophisticated approach is being developed to combine the backfitting algorithm with TVR (Yang, Tan 2018). Nevertheless, our approach, opting for the sequential use of the two procedures, is advantageous because it is not computationally demanding.

5. Conclusions

The consecutive use of the backfitting algorithm and TVR successfully identified the nominal release policies implemented in BMR during each of the two subperiods as the GAMs. The additive structure decomposed the varying parts of the nominal release policies into the two functions. The scale parameter of the TVR controlling the removal of spurious oscillations should be chosen so that the nominal release policies are sensitive to the time and water levels. The results have been utilized to compare the two subperiods, indicating the significant changes in the operator's release policies. The rapidly developing agronomic practices and the insufficient discharge capacity of the Kurau River receiving the water released from the spillways might be seriously burdening the operation of BMR. We have also addressed the situation in another study (Fadhil 2018), so that the reservoir operator is aware of future hydro-meteorological information, and deducing optimal release policies of BMR based on the SDP theory.

Declaration of competing interest

The authors declare that they have no known competing financial interests or personal relationships that could have appeared to influence the work reported in this paper.

Acknowledgments

The authors thank Malaysian authorities, including the Department of Irrigation and Drainage (DID), the Department of Agriculture and Agro-based Industry (DOA), and the National Hydraulic Research Institute of Malaysia (NAHRIM), for the provision of the reservoir management report and spatial and hydro-meteorological data. The Ministry of Higher Education in Iraq and the University of Mosul are acknowledged for providing the scholarship to the first author. This research is funded by Putra Grant No.9406300 from the Universiti Putra Malaysia, Grants-in-Aid for Scientific Research No.16KT0018 and No.19KK0167 from the Japan Society for the Promotion of Science (JSPS), and Bilateral Joint Research Project No. JPJSBP120229922 from JSPS.

References

- Adib M.N.M., Harun S., 2022, Metalearning approach coupled with CMIP6 multi-GCM for future monthly streamflow forecasting, *Journal of Hydrologic Engineering*, 27 (6), DOI: 10.1061/(ASCE)HE.1943-5584.0002176.
- Adib M.N.M., Harun S., Rowshon M.K., 2022, Long-term rainfall projection based on CMIP6 scenarios for Kurau River Basin of rice-growing irrigation scheme, Malaysia, *SN Applied Sciences*, 4 (3), DOI: 10.1007/s42452-022-04952-x.
- Adib M.N.M., Rowshon M.K., Mojid M.A., Habibu I., 2020, Projected streamflow in the Kurau River Basin of Western Malaysia under future climate scenarios, *Scientific Reports*, 10 (1), DOI: 10.1038/s41598-020-65114-w.
- Ahmad A., El-Shafie A., Razali S.F.M., Mohamad Z.S., 2014, Reservoir optimization in water resources: a review, *Water Resources Management*, 28 (11), 3391-3405, DOI: 10.1007/s11269-014-0700-5.
- Alam A.H.M.B., Unami K., Fujihara M., 2018, Holistic water quality dynamics in rural artificial shallow water bodies, *Journal of Environmental Management*, 223, 676-684, DOI: 10.1016/j.jenvman.2018.06.076.
- Anwar T.H.H.B.H.S., 2010, Bukit Merah Lake brief, paper presented at the National seminar on managing lakes and their basin for sustainable use: current status of selected in Malaysia.
- Biemans H., Speelman L.H., Ludwig F., Moors E.J., Wiltshire A.J., Kumar P., Gerten D., Kabat P., 2013, Future water resources for food production in five South Asian river basins and potential for adaptation – A modeling study, *Science of the Total Environment*, 468-469, S117-S131, DOI: 10.1016/j.scitotenv.2013.05.092.
- Breiman L., Friedman J.H., 1985, Estimating optimal transformations for multiple regression and correlation, *Journal of the American Statistical Association*, 80 (391), 580-598, DOI: 10.2307/2288473.
- Chen R., Tsay R.S., 1993, Nonlinear additive ARX models, *Journal of the American Statistical Association*, 88 (423), 955-967, DOI: 10.2307/2290787.
- DID, 2011, Review of the national water resources study (2000-2050) and formulation of national water resources policy: final report, Kuala Lumpur, Kementerian Sumber Asli Dan Alam Sekitar Malaysia, available at <https://www.water.gov.my/jps/resources/PDF/Hydrology%20Publication/Vol2WaterGovernance.pdf> (data access 05.10.2022).
- Dor N., Syafalni S., Abustan I., Rahman M.T.A., Nazri M.A.A., Mostafa R., Mejus L., 2011, Verification of surface-groundwater connectivity in an irrigation canal using geophysical, water balance and stable isotope approaches, *Water Resources Management*, 25 (11), 2837-2853, DOI: 10.1007/s11269-011-9841-y.
- El-Shafie A., El-Shafie A., Mukhlisin M., 2014, New approach: integrated risk-stochastic dynamic model for dam and reservoir optimization, *Water Resources Management*, 28 (8), 2093-2107, DOI: 10.1007/s11269-014-0596-0.
- Fadhil R.M., 2018, Daily operation of Bukit Merah Reservoir with stochastic dynamic programming under the impact of climate change, Ph.D., Universiti Putra Malaysia, 220 pp.
- Fadhil R.M., Rowshon M.K., Ahmad D., Fikri A., Aimrun W., 2017, A stochastic rainfall generator model for simulation of daily rainfall events in Kurau catchment: model testing, *Acta Horticulturae*, 1152, 1-10, DOI: 10.17660/ActaHortic.2017.1152.1.

- Fadhil R.M., Unami K., 2021, A multi-state Markov chain model to assess drought risks in rainfed agriculture: a case study in the Nineveh Plains of Northern Iraq, *Stochastic Environmental Research and Risk Assessment*, 35, 1931-1951, DOI: 10.1007/s00477-021-01991-5.
- Farr T.G., Rosen P.A., Caro E., Crippen R., Duren R., Hensley S., Kobrick M., Paller M., Rodriguez E., Roth L., Seal D., Shaffer S., Shimada J., Umland J., Werner M., Oskin M., Burbank D., Alsdorf D., 2007, The shuttle radar topography mission, *Reviews of Geophysics*, 45 (2), RG2004, DOI: 10.1029/2005RG000183.
- Giuliani M., Herman J.D., Castelletti A., Reed P., 2014, Many-objective reservoir policy identification and refinement to reduce policy inertia and myopia in water management, *Water Resources Research*, 50 (4), 3355-3377, DOI: 10.1002/2013WR014700.
- Hamidon N., Harun S., Malek M.A., Ismail T., Alias N., 2015, Prediction of paddy irrigation requirements by using statistical downscaling and CROPWAT models: a case study from the Kerian Irrigation Scheme in Malaysia, *Jurnal Teknologi*, 76 (1), 281-288. DOI: 10.11113/jtv76.4038.
- Heidari M., Chow V.T., Kokotovic P.V., Meredith D.D., 1971, Discrete differential dynamic programming approach to water resources systems optimization, *Water Resources Research*, 7 (2), 273-282, DOI: 10.1029/WR007i002p00273.
- Ismail W.R., Najib S.A.M., 2011, Sediment and nutrient balance of Bukit Merah Reservoir, Perak (Malaysia), *Lakes and Reservoirs. Science, Policy and Management for Sustainable Use*, 16 (3), 179-184, DOI: 10.1111/j.1440-1770.2011.00453.x.
- Labadie J.W., 2004, Optimal operation of multireservoir systems: state-of-the-art review, *Journal of Water Resources Planning and Management*, 130 (2), 93-111, DOI: 10.1061/(ASCE)0733-9496(2004)130:2(93).
- Lee M.-H., Bae D.-H., 2015, Climate change impact assessment on green and blue water over Asian Monsoon Region, *Water Resources Management*, 29 (7), 2407-2427, DOI: 10.1007/s11269-015-0949-3.
- Mereu S., Susnik J., Trabucco A., Daccache A., Vamvakieridou-Lyroudia L., Renoldi S., Virdis A., Savic D., Assimacopoulos D., 2016, Operational resilience of reservoirs to climate change, agricultural demand, and tourism: A case study from Sardinia, *Science of the Total Environment*, 543, 1028-1038, DOI: 10.1016/j.scitotenv.2015.04.066.
- Nop C., Fadhil R.M., Unami K., 2021, A multi-state Markov chain model for rainfall to be used in optimal operation of rainwater harvesting systems, *Journal of Cleaner Production*, 285, DOI: 10.1016/j.jclepro.2020.124912.
- Osher S., Burger M., Goldfarb D., Xu J., Yin W., 2005, An iterative regularization method for total variation-based image restoration, *Multiscale Modeling and Simulation*, 4 (2), 460-489, DOI: 10.1137/040605412.
- Overgaard N.C., 2019, On the taut string interpretation and other properties of the Rudin-Osher-Fatemi model in one dimension, *Journal of Mathematical Imaging and Vision*, 61 (9), 1276-1300, DOI: 10.1007/s10851-019-00905-z.
- Rani D., Moreira M.M., 2010, Simulation-optimization modeling: a survey and potential application in reservoir systems operation, *Water Resources Management*, 24 (6), 1107-1138, DOI:10.1007/s11269-009-9488-0.
- Rowshon M.K., Kwok C.Y., Lee T.S., 2003a, GIS-based scheduling and monitoring irrigation delivery for rice irrigation system: Part II. Monitoring, *Agricultural Water Management*, 62 (2), 117-126, DOI: 10.1016/S0378-3774(03)00093-3.
- Rowshon M.K., Kwok C.Y., Lee T.S., 2003b, GIS-based scheduling and monitoring of irrigation delivery for rice irrigation system: Part I. Scheduling, *Agricultural Water Management*, 62 (2), 105-116, DOI: 10.1016/S0378-3774(03)00092-1.
- Rudin L.I., Osher S., Fatemi E., 1992, Nonlinear total variation based noise removal algorithms, *Physica D: Nonlinear Phenomena*, 60 (1-4), 259-268, DOI: 10.1016/0167-2789(92)90242-F.
- Tejada-Guibert J.A., Johnson S.A., Stedinger J.R., 1993, Comparison of two approaches for implementing multireservoir operating policies derived using stochastic dynamic programming, *Water Resources Research*, 29 (12), 3969-3980, DOI: 10.1029/93WR02277.
- Tejada-Guibert J.A., Johnson S.A., Stedinger J.R., 1995, The value of hydrologic information in stochastic dynamic programming models of a multireservoir system, *Water Resources Research*, 31 (10), 2571-2579, DOI: 10.1029/95WR02172.
- Turner S.W.D., Steyaert J.C., Condon L., Voisin N., 2021, Water storage and release policies for all large reservoirs of conterminous United States, *Journal of Hydrology*, 603, DOI: 10.1016/j.jhydrol.2021.126843.
- Unami K., Fadhil R.M., Kamal M.R., 2021, Rainfall-runoff models with fractional derivatives applied to Kurau River Basin, Perak, Malaysia, *Basrah Journal of Agricultural Sciences*, 34 (1), 34-40, DOI: 10.37077/25200860.2021.34.sp1.4.

- Unami K., Fadhil R.M., Rowshon M.K., 2019a, Generalized additive models for water balance in Bukit Merah Reservoir, Perak, Malaysia, [in:] The 2019 International Symposium on Nonlinear Theory and Its Applications (NOLTA2019), Kuala Lumpur, Malaysia, 9025.
- Unami K., Mohawesh, O., 2018, A unique value function for an optimal control problem of irrigation water intake from a reservoir harvesting flash floods, *Stochastic Environmental Research and Risk Assessment*, 32 (11), 3169-3182, DOI: 10.1007/s00477-018-1527-z.
- Unami K., Mohawesh O., Fadhil R.M., 2019b, Time periodic optimal policy for operation of a water storage tank using the dynamic programming approach, *Applied Mathematics and Computation*, 353, 418-431, DOI: 10.1016/j.amc.2019.02.005.
- Walęga A., Młyński D., Radecki-Pawlik A., 2020, The influences of meteorological and hydrological factors on the operation and performance of a semi-natural stormwater reservoir, *Meteorology Hydrology and Water Management*, 8 (1), 28-34, DOI: 10.26491/mhwm/111032.
- Yaegashi Y., Yoshioka H., Unami K., Fujihara M., 2018, A singular stochastic control model for sustainable population management of the fish-eating waterfowl *Phalacrocorax carbo*, *Journal of Environmental Management*, 219, 18-27, DOI: 10.1016/j.jenvman.2018.04.099.
- Yakowitz S., 1982, Dynamic programming applications in water resources, *Water Resources Research*, 18 (4), 673-696, DOI: 10.1029/WR018i004p00673.
- Yang T., Tan Z., 2018, Backfitting algorithms for total-variation and empirical-norm penalized additive modelling with high-dimensional data, *Stat*, 7 (1), DOI: 10.1002/sta4.198.

Trends and fluctuations of river ice regimes in the Prypiat Basin, within Ukraine

Liudmyla Gorbachova , Oleksandr Afteniuk, Borys Khrystiuk , Oleksandr Lobodzynskyi

Ukrainian Hydrometeorological Institute

Abstract

Information about the formation, destruction, and duration of river ice regimes is especially important for hydropower, shipping, fisheries, etc. Research into modern trends in river ice regimes and their spatial and temporal fluctuations is essential, especially in a changing climate. This study examines the trends and fluctuations of air temperature and ice regimes based on series of observations in the Prypiat River basin within Ukraine. Air temperature data from 17 meteorological stations and ice data from 29 water gauges were analyzed. A complex analytical approach involving statistical and graphical methods was employed. The Mann-Kendall statistical test, mass curve, residual mass curve, and combined graphs were used in the study. In the Prypiat River basin within Ukraine, observations of mean monthly air temperature, ice occurrence, freeze-up, and their duration are homogeneous (quasi-homogeneous) and stationary (quasi-stationary). The quasi-homogeneous and quasi-stationary characteristics are explained by the presence in the observation series of only increasing and decreasing phases of long-term cyclical fluctuations, which are incomplete. The trends of air temperature and ice regime correspond strongly, indicating the defining role of air temperature in the formation of ice occurrence and freeze-up. Since the end of the 1990s, the warming phase of air temperature in the autumn-winter period determines the appearance of ice and freeze-up later in the year. In March, the warming trend in air temperature, which began after 1988, determines the freeze-up, break-up, and disappearance of ice earlier in the year. Thus, the duration of ice and freeze-up on the rivers has decreased.

Keywords

Ice phenomena, air temperature, Prypiat River, homogeneity, stationarity, cyclic fluctuations, tendencies.

Submitted 7 November 2022, revised 19 May 2023, accepted 30 May 2023

DOI: 10.26491/mhwm/166632

1. Introduction

Information about river ice dynamics has practical importance because ice can affect the operations of various sectors of the economy, as well as the ecological state of waters, and biochemical processes in the aquatic environment and flood plains (Prowse, Bonsal 2004; Allan, Castillo 2007; Beltaos, Burrell 2015; Graf 2020). Interest in research into formation conditions, destruction, and duration of ice on rivers has increased because of climate warming (Magnuson et al. 2000; Smith 2000; Prowse et al. 2007; Strutynska, Grebin 2010; Rokaya et al. 2018; Yang et al. 2020). Magnuson et al. (2000) reported that from 1846 to 1995 in the Northern Hemisphere, freeze dates of ice on lakes and rivers have become later and break-up dates earlier in response to increasing air temperatures of about 1.2°C per 100 years. Yang et al. (2020) reported that, globally, river ice is measurably declining and will continue to decline linearly with projected increases in surface air temperature toward the end of this century. Research into ice dynamics at the regional level is also urgent because the resulting knowledge supports planning for the operation of hydro-power, shipping, fisheries, etc.

The Prypiat River basin within Ukraine is located in the Polissia region, where the mean annual air temperature has increased by about 1.0°C in recent decades (Balabukh, Malytska 2017). Strutynska and Grebin (2010) reported an increase in the mean annual temperature of river water from 0.1 to 0.6°C in the Dniipro River basin. Trends in air temperature and river water temperature directly affect river ice formation,

freeze-up, and duration (Graf 2020; Yang et al. 2020). Accordingly, Gorbachova and Afteniuk (2020) reported an increasing frequency of winters in which ice did not form since the 1970s in the Prypiat River basin within Ukraine.

Assessment of tendencies and fluctuations in time-series of observations can be carried out by various methods. Kundzewicz and Robson (2000) reported that the choice of methods is a critical task because it can influence the results. A complex approach based on the use of an array of tests and methods is recommended to obtain more reliable results (Kundzewicz, Robson 2004; WMO 2009; Gorbachova, Bauzha 2013; Hussain 2019).

This study examines the analysis of trends and fluctuations of air temperature and ice observation series in the Prypiat River basin within Ukraine based on a complex approach using statistical and graphical methods.

2. Study area, data, and methodology

2.1. Study area

The Prypiat River is a large right-hand tributary of the Dnipro River, which flows through parts of Belarus and Ukraine. It originates in the west of Ukrainian Polissia, thence 204 km downstream it crosses the border into the Republic of Belarus, where it flows for more than 500 km along the Polissia lowland. The last 50 km of the Prypiat River flows again into the territory of Ukraine and into the Kyiv reservoir (Dnipro River) (Fig. 1) (Kalinin, Obodovskyi 2003).

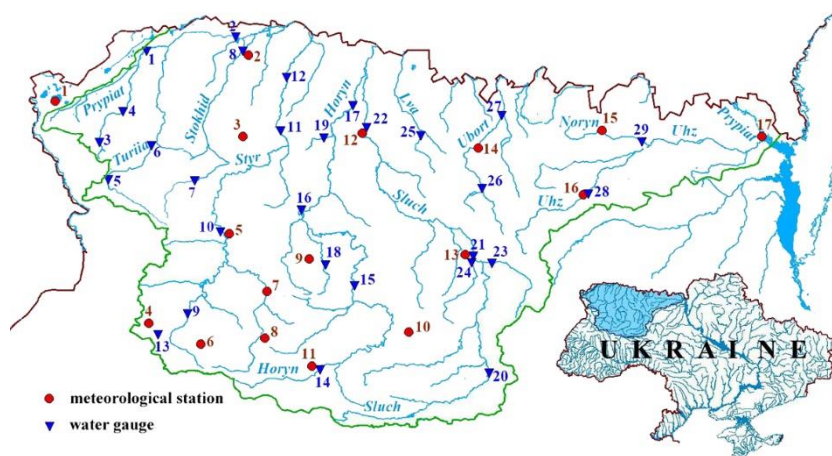


Fig. 1. The location of the Prypiat River basin within Ukraine and the 29 water gauges and 17 meteorological stations within its catchment (the numbering of stations is based on Tables 1 and 2).

The total length of the river is 761 km, and the catchment area is 121,000 km². Within the borders of Ukraine, the length of the river is 254 km, the catchment area is 68,370 km², and it is the greater right-bank part of the Prypiat River basin (Kalinin, Obodovskyi 2003; Vishnevsky 2000). The Ukrainian part of the Prypiat River basin borders the Western Bug River to the south and west, the Dniester and Southern Bug Rivers to the south, and the Dnipro River to the east and southeast. The Prypiat River has 14 right-

bank tributaries, of which the Horyn, Styr, and Uzh rivers are the largest. The right-bank river basin is located in Polissia, which is characterized by lowland relief, wide waterlogged river valleys, a positive moisture balance, and a wide distribution of sod-podzolic and swampy soils. The relief of Polissia is a large plain with altitudes that rarely exceed 150-200 m (Vasylenko 2015).

According to the classification by Köppen (1936), the climate of the Prypyat basin is temperate-continental with warm and humid summers and fairly mild winters. The territory of the basin is mainly under the influence of Atlantic air masses, as well as Arctic air, which brings cooling throughout the year. Warming in winter and hot weather in summer are caused by southern tropical air masses that, although rarely, sometimes reach Polissia. Summer, especially in the second half, is characterized by cool and often rainy weather. Autumn is often rainy, and spring is more prone to unstable weather, which is explained by the change of various air masses, cyclones, and anticyclones.

The warmest month in the basin is July, and the coldest is January. Sometimes there are shifts in heat and cold peaks, respectively, in August and February. The mean temperature in July is 18-19°C, and in January is from -4.5°C to -7°C (Kalinin, Obodovskyi 2003; Strutynska, Grebin 2010).

Cyclones coming from the Atlantic bring with them a significant amount of precipitation, the average annual amount of which fluctuates within significant limits and is 600-700 mm on the right bank. The largest amount of precipitation falls in July-August: in dry years, as little as 350 mm, and in wet years up to 1000 mm or more (Kalinin, Obodovskyi 2003).

Ice phenomena of the Prypiat River in the form of shore ice and grease usually appear in late October-November. Autumn ice drift on the river, on average, begins in the last 10 days of November or early December, but in some years, it is observed near the end of October and is sometimes delayed until mid- or late-December (Strutynska, Grebin 2010).

2.2. Data

Trend analysis of air temperature was based on data from 17 meteorological stations (Fig. 1). Mean monthly air temperatures for November, December, and March were calculated from the earliest observations to 2020, inclusive (Table 1). These data were compiled from the Meteorological Yearbooks published by the Borys Sreznevsky Central Geophysical Observatory (Kyiv, Ukraine). November, December, and March were chosen because, in most cases, in the rivers of the basin ice formation and freeze-up occur in November and December and ice break-up and melting occur in March (Afteniuk 2020). The mean duration of the records is 80 years. The longest record covers 96 years (Novohrad-Volynskiyi stations); the shortest covers 71 years (Olevsk stations).

Ice data from 29 water gauges in the Prypiat River basin were compiled from the Hydrological Yearbooks, also published by the Borys Sreznevsky Central Geophysical Observatory (Fig. 1, Table 2). Data were used from the earliest observations to 2020, inclusive. The mean duration of the records is 78 years. A large majority of records cover more than 70 years. Most observations begin in the 1920s-1930s, with the latest

beginning in 1985. Thus, the longest record has observations for 96 years (Sluch River, Novohrad-Volynskyi city), and the shortest record has observations for 35 years (Ustia River, Kornyn village).

Table 1. List of meteorological stations in the Prypiat River basin within Ukraine.

No.	Name	River sub-basin	Study period / its duration, years
1	Svitiaz	Upper Prypiat	1946-2020 / 75
2	Liubeshiv	Stokhid	1945-2020 / 76
3	Manevichi	Stokhid	1946-2020 / 75
4	Kovel	Styr	1934-1939, 1941-2020 / 86
5	Lutsk	Styr	1925-1932, 1945-2020 / 84
6	Brody	Styr	1945-2020 / 76
7	Dubno	Ikva	1945-2020 / 76
8	Kremenets	Ikva	1947-2020 / 74
9	Rivne	Horyn	1945-2020 / 76
10	Shepetivka	Horyn	1924-1941, 1945-2020 / 94
11	Yampil	Horyn	1937-1942, 1944-2020 / 83
12	Sarny	Sluch	1925-1932, 1940-1941, 1946-2020 / 85
13	Novohrad-Volynskyi	Sluch	1923-1941, 1944-2020 / 96
14	Olevsk	Ubort	1950-2020 / 71
15	Ovruch	Noryn	1944-2020 / 77
16	Korosten	Uzh	1924-1942, 1944-1962, 1976-2000 / 82
17	Chernobyl	Lower Prypiat	1940-1986, 1988-2020 / 80

Note that the longest records of air temperature and ice phenomena have gaps of several years. These gaps are small compared to the total duration of the records and allow us to carry out trend analysis. In addition, the results of such an analysis can be used to determine the probabilistic characteristics of ice phenomena for which information on all observed phenomena is important.

For each water gauge and each winter period (October to April), six data classes were extracted:

- 1) appearance date of ice;
- 2) date of freeze-up;
- 3) break-up date (i.e., melt onset);
- 4) date of ice disappearance;
- 5) duration of continuous freeze-up;
- 6) overall duration of ice.

The date after which the ice lasted for 3 or more days was taken as the appearance date of ice. In cases when icing was interrupted, i.e., the water surface was clear of ice, and the duration of such an interruption was from 1 to 3 days, the period was considered continuous. The ice break-up date was determined by the dates of the beginning of melting. The date of disappearance was defined as the last date when ice was observed. This approach objectively reflects the real situation of ice phenomena on rivers.

2.3. Methodology

Statistical and graphical methods were used to assess trends in air temperature and ice dynamics in the Prypiat River basin in Ukraine. Given the features of the hydrological and meteorological series of observations (non-normal distributions, seasonally and serially correlated), the Pearson method and nonparametric Mann-Kendall test were used (Kundzewicz, Robson 2004; WMO 2009). The trend equation in the time series and the correlation coefficient between variables were determined by the Pearson method. Estimation of statistical significance in trends employed the nonparametric Mann-Kendall test (Mann 1945; Kendall 1975). The calculations were carried out using RStudio Software (version 1.4.1717) (R Core Team 2017). If the statistical characteristics (mean and variance) of time-series do not change over time, then the time series exhibits stationarity (i.e., there is no time trend) (Robson 2002).

Table 2. List of water gauges in the Prypiat River basin within Ukraine.

No	River	Water gauge	Catchment area (km ²)	Study period / its duration, years
1	Prypiat	Richytsa village	2210	1940-1941, 1946-2020 / 75
2	Prypiat	Liubiaz village	6100	1946-2020 / 74
3	Vyzhivka	Ruda village	141	1929-1933, 1945-2020 / 79
4	Vyzhivka	Stara Vyzhivka village	722	1944-2020 / 76
5	Turiia	Yahidne village	502	1939-1941, 1945-2020 / 77
6	Turiia	Kovel city	1480	1923-1934, 1939-1941, 1945-2020 / 87
7	Stokhid	Malynivka village	692	1940-1941, 1945-2020 / 76
8	Stokhid	Liubeshiv village	2970	1923-1933, 1940-1941, 1945-2020 / 86
9	Styr	Shchurovychi village	2020	1939-1941, 1946-2020 / 76
10	Styr	Lutsk city	7200	1923-1933, 1935-1941, 1944-2020 / 92
11	Styr	Kolky village	9050	1946-2020 / 74
12	Styr	Mlynok village	10900	1929-1941, 1946-1956, 1959-2020 / 83
13	Radostavka	Triitsia village	316	1945-2020 / 75
14	Horyn	Yampil village	1400	1936-1941, 1943-2020 / 82
15	Horyn	Ozhenyn village	5860	1939-1941, 1945-2020 / 77
16	Horyn	Derazhne village	9160	1939-1942, 1946-2020 / 77
17	Horyn	Dubrovytsia city	12000	1935-2020 / 85
18	Ustia	Kornyn village	485	1985-2020 / 35
19	Vyrka	Svaryni village	231	1946-2020 / 74
20	Sluch	Hromada village	2480	1926-1927, 1930-1941, 1945-2020 / 87
21	Sluch	Novohrad-Volynskiy city	7460	1924-2020 / 96
22	Sluch	Sarny city	13300	1945-2020 / 75
23	Tnia	Bronyky village	982	1936-1941, 1943, 1945-2020 / 81
24	Smilka	Susly village	632	1939-1941, 1944-2020 / 78
25	Lva	Osnytsk village	276	1946-2020 / 74
26	Ubort	Rudnia-Ivanivska village	776	1927-1941, 1945-2020 / 89
27	Ubort	Perha village	2880	1924-1941, 1946-2020 / 91
28	Uzh	Korosten city	1450	1930-1941, 1944-2020 / 87
29	Noryn	Slovenshchyna village	804	1963-2020 / 57

Graphical analysis has been widely recommended for confirming the results of trend analysis by statistical tests (Kundzewicz, Robson 2000, 2004; WMO 2009; Gorbachova 2016; Şen 2017; Hussain 2019; Onyutha 2021). This approach is especially important when statistical tests do not have unambiguous interpretations, e.g., when only one statistical test is used, or when several statistical tests with the same properties are used (Robson 2002; WMO 2009; Gorbachova, Bauzha 2013).

Graphic methods such as mass curve analysis, double mass analysis, and residual mass curve are the most widely used in these investigations (Gorbachova 2016). Klemeš (1987) and Gorbachova (2016) reported that at the end of the 19th and during the 20th centuries these methods were developed by Rippl (1883), Schoklitch (1923), Novotný (1925), Merriam (1937), Kohler (1949), Weiss and Wilson (1953), Searcy and Hardison (1960); Ehlert (1972). The present investigation employed the mass curve, residual mass curve, and combined graphs. This methodological approach was developed by Gorbachova (2014, 2016) and applied to evaluate river flow trends (Bauzha, Gorbachova 2017; Gorbachova et al. 2018; Zabolotnia et al. 2019; Romanova et al. 2019; Melnyk, Loboda 2020; Zabolotnia et al. 2022), also including ice dynamics. (Gorbachova, Khrystyuk 2012; Gorbachova 2013; Rachmatullina, Grebin 2014).

The mass curve is used to detect changes in hydrometeorological characteristics under the influence of anthropogenic factors and climate change, which can appear on the curve in the form of "jumping," "emissions," or unidirectional deviation. Residual mass curves and combined graphs were used for the assessment of spatiotemporal fluctuations of hydrometeorological characteristics. The residual mass curve supports analysis of trends in hydrometeorological characteristics over time: periods of change, cyclical fluctuations, and their characteristics (phases of increase and decrease, their duration, synchronicity, in-phase). In turn, the synchrony or asynchrony of long-term fluctuations of hydrometeorological characteristics in the different observation series can be defined by combined graphs. Moreover, the residual mass curve analysis of hydrometeorological characteristics supports determining the stationarity of data series, i.e., the sustainability of the mean value of the time series over time. The mean value of the time series is stable in the presence of at least one full closed cycle (increase and decrease phases) of long-time fluctuations. The methodological recommendations for the use of graphic methods are described in detail by Gorbachova et al. (2018).

For graphical analysis of ice dynamics, dates for initial values for their numeric presentation were taken to be the earliest dates of the appearance (or disappearance) of river ice.

3. Results

3.1. Air temperature

Analysis of data from the observation series of mean monthly air temperature for November, December, and March for stationarity with the Mann-Kendall test showed statistically significant trends ($p \leq 0.05$) for all observations in March (Table 3). In November, 8 observation series of the mean monthly air temperature were stationary, and in December, only 4 series were stationary. For a clearer understanding

and confirmation of the results according to the Mann-Kendall statistical test, the study evaluated the homogeneity, stationarity, and fluctuations of the observation series using graphic methods.

The mass curves of the mean monthly air temperature show that all observation series are homogeneous because the curves do not display "jumping," "emissions," or unidirectional deviation (Fig. 2, upper row).

Table 3. Results of testing the air temperature observation series for stationarity according to the Mann-Kendall test in the Prypiat River basin within Ukraine.

No.	Name of the meteorological station	Statistical significance of the trend at a significance level of 5%		
		November	December	March
1	Svitiaz	yes	yes	yes
2	Liubeshiv	yes	yes	yes
3	Manevichi	no	yes	yes
4	Kovel	yes	yes	yes
5	Lutsk	no	yes	yes
6	Brody	yes	yes	yes
7	Dubno	yes	no	yes
8	Kremenets	no	no	yes
9	Rivne	no	no	yes
10	Shepetivka	no	yes	yes
11	Yampil	no	yes	yes
12	Sarny	no	yes	yes
13	Novohrad-Volynskiyi	no	yes	yes
14	Olevsk	yes	no	yes
15	Ovruch	yes	yes	yes
16	Korosten	no	yes	yes
17	Chernobyl	yes	yes	yes

The forms of the residual mass curves indicate that the observation series of the mean monthly air temperature are characterized by cyclical fluctuations of different durations (Fig. 2 bottom row). In November, the series of mean monthly air temperatures have several short complete cycles of fluctuations that lasted from the beginning of observations, i.e., from the beginning of the 1920s until 1978. Their mean duration was 9 years. The long-term cycle of fluctuations began after 1978, namely, the cooling phase was from 1978 to 1999, and the warming phase began after 1999, continuing to the present, and the end of which cannot be predicted.

In December, the cooling phase was from the beginning of the 1920s until 1948. After 1948, two relatively short but well-defined cycles of fluctuations were observed. Their durations were 21 years (1948-1969) and 33 years (1970-2002). The warming phase began after 2002. In March, the mean monthly air temperature series have a clearly defined cooling phase and a warming phase of long-term cyclical fluctuations. The cooling phase started from the beginning of observations and lasted until 1988. The warming phase began after 1988. Cycles of short fluctuations are traced both for the cooling phase and for

the warming phase. However, such short fluctuations have a rather short duration, i.e., 4-6 years on average and a small amplitude.

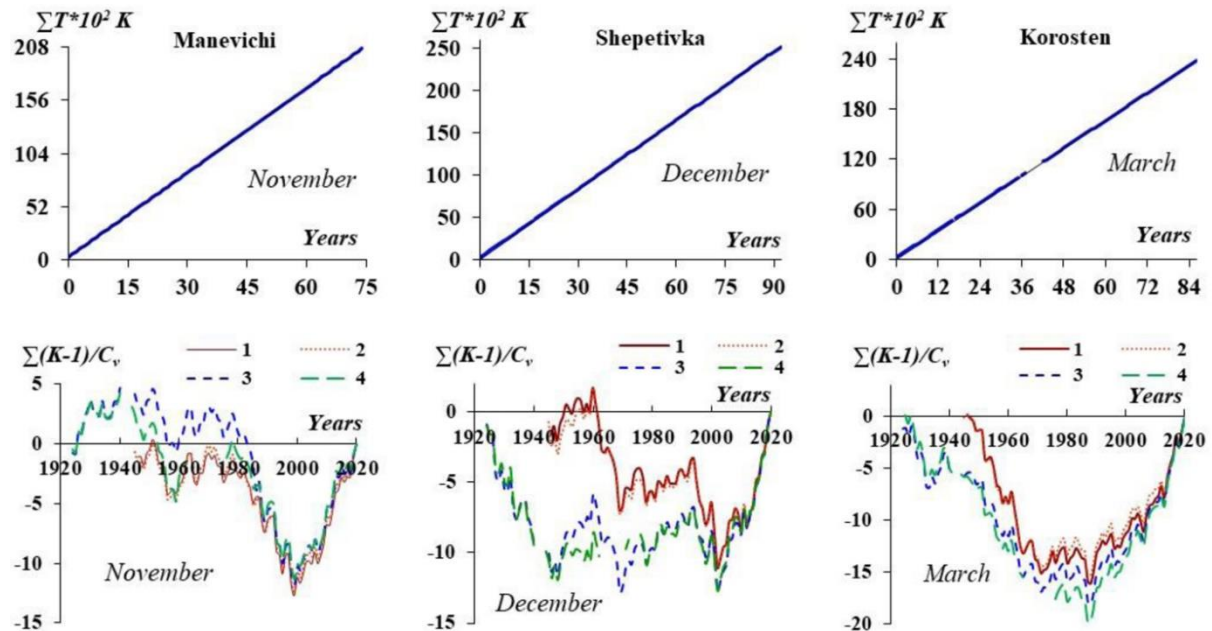


Fig. 2. Mass curves (upper row) and residual mass curves (bottom row) of mean monthly air temperature for November (on the left side), December (in the center), and March (on the right side) for some meteorological stations (1 – Manevichi, 2 – Dubno, 3 – Shepetivka, 4 – Korosten) in the Prypiat River basin (within Ukraine); K = temperature in degrees Kelvin.

The beginning of the cooling phase in the air temperature observation series can be determined clearly only in November. For all other series, the cooling and warming phases are incomplete because the beginning of the observations took place when the cooling phase was already ongoing, and the warming phase is still ongoing. So, for defining constant average values, all observation series are not representative. Nonetheless, the observation series of mean monthly air temperature still have phases of cooling and warming long-term cyclical fluctuations, although they are incomplete. Such a series can be classified as quasi-stationary.

Long-term cyclic fluctuations of the mean monthly air temperature in November, December, and March are characterized by synchronicity and in-phase, indicating homogeneity of air temperature dynamics throughout the Prypiat River basin.

3.2. Ice dynamics

The analysis of ice occurrence and freeze-up observations for stationarity according to the Mann-Kendall test showed that most of the series are non-stationary (Table 4). At the same time, the observation series of ice-appearance date and freeze-up did not have the same trends. Twelve observation series for ice-appearance date and 17 observation series for the date of freeze-up turned out to be stationary.

Mass curves of the ice-appearance date and freeze-up on rivers and their duration show that the cumulative values initially deviate from a straight line, but then change direction and cross the straight line and seem to form a kind of arc (Figs. 3 and 4, upper rows).

Table 4. Results of analyzing the ice-occurrence observation series for stationarity according to the Mann-Kendall test in the Prypiat River basin within Ukraine. Abbreviations: ADI – appearance date of ice, ADF – date of freeze-up, BDF – break-up date of freeze-up, DDI – date of ice disappearance, DF – duration of continuous freeze-up, DI – duration of ice.

No	Water gauge	Statistical significance of the trend					
		Ice phenomena				Duration	
		ADI	ADF	BDF	DDI	DF	DI
1	Prypiat River – Richytsa village	yes	no	yes	yes	yes	yes
2	Prypiat River – Liubiaz village	yes	yes	yes	yes	yes	yes
3	Vyzhivka River – Ruda village	yes	yes	yes	yes	yes	yes
4	Vyzhivka River – Stara Vyzhivka village	yes	yes	yes	no	yes	yes
5	Turiia River – Yahidne village	yes	no	yes	yes	yes	yes
6	Turiia River – Kovel city	yes	yes	yes	yes	yes	yes
7	Stokhid River – Malynivka village	yes	yes	yes	yes	yes	yes
8	Stokhid River – Liubeshiv village	no	no	yes	yes	yes	yes
9	Styr River – Shchurovychi village	yes	no	yes	yes	yes	yes
10	Styr River – Lutsk city	no	no	yes	yes	yes	yes
11	Styr River – Kolky village	yes	no	yes	yes	yes	yes
12	Styr River – Mlynok village	no	no	yes	yes	yes	yes
13	Radostavka River – Triitsia village	yes	yes	yes	yes	yes	yes
14	Horyn River – Yampil village	no	no	yes	yes	yes	yes
15	Horyn River – Ozhenyn village	yes	yes	yes	yes	yes	yes
16	Horyn River – Derazhne village	yes	no	yes	yes	yes	yes
17	Horyn River – Dubrovytsia city	yes	no	yes	yes	yes	yes
18	Ustia River – Kornyn village	no	no	no	no	no	no
19	Vyrka River – Svaryni village	no	yes	yes	yes	yes	yes
20	Sluch River – Hromada village	no	yes	yes	yes	yes	yes
21	Sluch River - Novohrad-Volynskyi city	yes	yes	yes	yes	yes	yes
22	Sluch River – Sarny city	no	no	yes	yes	yes	yes
23	Tnia River – Bronyky village	no	no	yes	yes	yes	yes
24	Smilka River – Susly village	yes	yes	yes	yes	yes	yes
25	Lva River – Osnytsk village	yes	yes	yes	yes	yes	yes
26	Ubort River – Rudnia-Ivanivska village	no	no	yes	yes	yes	yes
27	Ubort River – Perha village	no	no	no	yes	no	yes
28	Uzh River – Korosten city	yes	no	yes	yes	yes	yes
29	Noryn River – Slovenshchyna village	no	no	yes	yes	yes	yes

This type of mass curve indicates the absence of a unidirectional stable tendency in the series of ice dynamics. So, the form of the mass curves shows that the observation series have inflection points, after which the trends change.

The analysis of residual mass curves showed that the observation series for which the ice-appearance date and the freeze-up date occurred in November show a transition from a decreasing phase to an increasing phase in long-term cyclical fluctuations in 1999 (Figs. 3 and 4, bottom row). If the formation of ice and freeze-up on the rivers occurred in December, then such a transition was in 2002. A different trend is characteristic for the break-up date of freeze-up and the ice-disappearance date, i.e., the observations began in the increasing phase, changing into the decreasing phase after 1988. The observation series of the duration of freeze-up and ice occurrence have similar tendencies. Therefore, the presence in the observation series of the phases of increasing and decreasing long-term cyclical fluctuations determines the arc-shaped form of the mass curves of ice phenomena and their duration. It is clear that such observation series are quasi-homogeneous and quasi-stationary.

The analysis of cyclic fluctuations of the mean monthly air temperature in November, December, and March, along with cyclic fluctuations of ice-appearance main phases and their duration shows that air temperature is the main factor affecting ice formation in rivers and determines their long-term tendencies. Thus, the warming phase that began in 1999 for November and 2002 for December, determined the increasing phase of the ice-occurrence dates and freeze-up dates on rivers, i.e., icing and freeze-up are forming on the rivers later in the year. The warming phase for March began after 1988. This causes earlier ice break-up and disappearance on the rivers (decreasing phase). As a result of these dynamics, the duration of ice occurrence and freeze-up on the rivers in the Pripjat River basin has decreased.

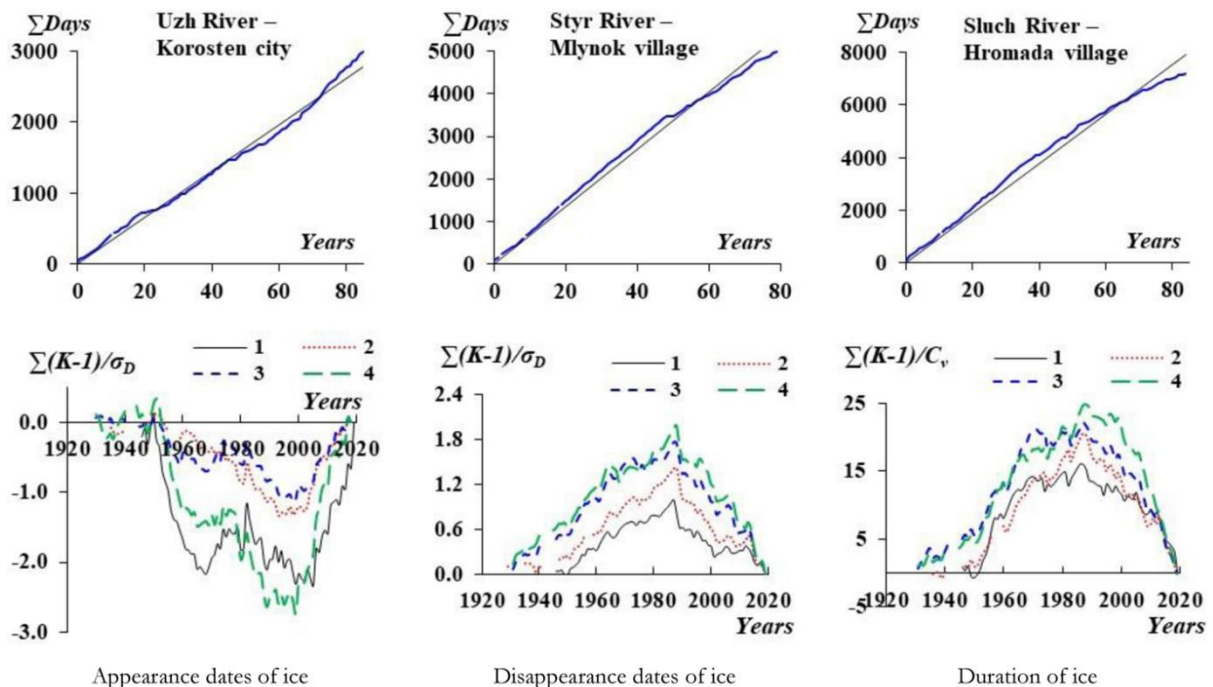


Fig. 3. Some mass curves (upper row) and residual mass curves (bottom row) of the ice-appearance date (on the left side), ice -disappearance date (in the center), and ice duration (on the right side) in the Pripjat River basin within Ukraine: 1 – Pripjat River – Liubiaz village, 2 – Styr River – Mlynok village, 3 – Sluch River – Hromada village, 4 – Uzh River – Korosten city; σ_D = standard deviation of the observation series of the ice appearance and disappearance dates.

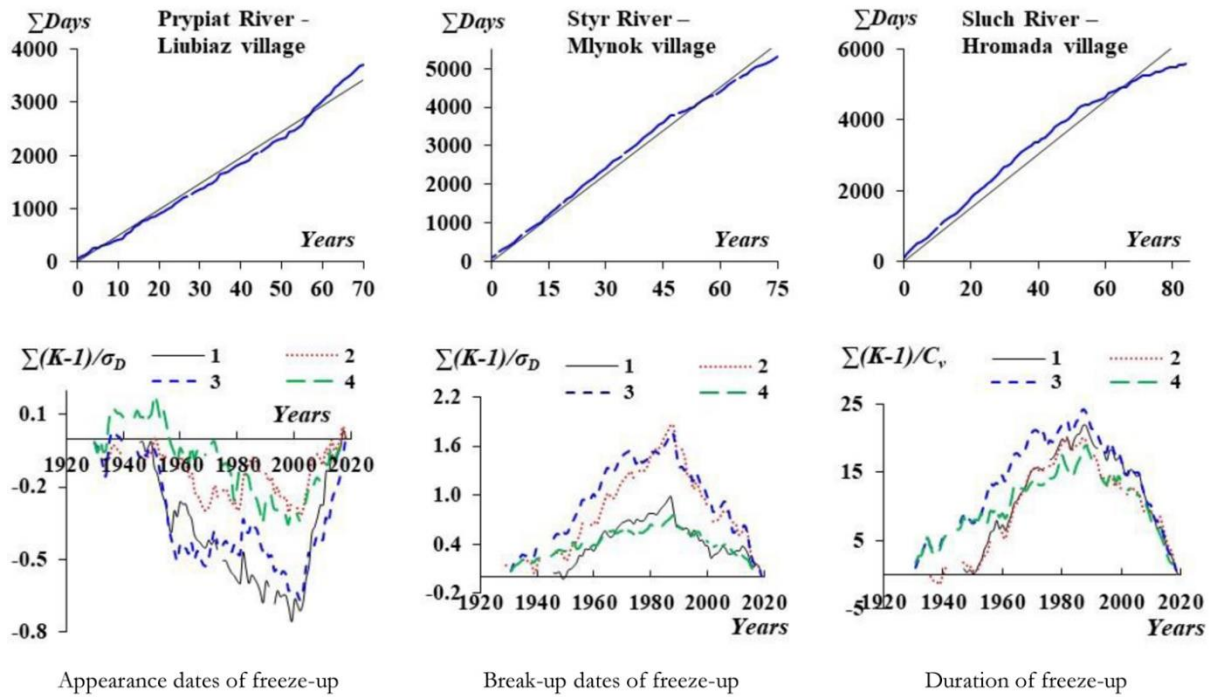


Fig. 4. Mass curves (upper row) and residual mass curves (bottom row) of the dates of freeze-up (on the left side), break-up dates of freeze-up (in the center), and duration of freeze-up (on the right side) in the Prypiat River basin within Ukraine: 1 – Prypiat River – Liubiaz village, 2 – Styr River – Mlynok village, 3 – Sluch River – Hromada village, 4 – Uzh River – Korosten city; σ_D = the standard deviation for the observation series of the freeze-up appearance and break-up dates.

4. Discussion

In different phases of cyclic fluctuations of hydrometeorological characteristics, observed trends have different directions (Pekarova 2003; Gorbachova 2015; Gorbachova et al. 2022). The decreasing phase has hydrometeorological values significantly lower than the values observed in the increasing phase, which causes the differences in mean values for these phases of long-term cyclic fluctuations. As a result, when analyzed by statistical tests, the series of observations that have only decreasing or increasing phases will be classified as non-stationary. This is exactly the result obtained by the Mann-Kendall statistical test for the observation series of the mean monthly air temperature in March, the ice break-up dates, the ice-disappearance dates and ice duration in the Pripyat River basin. At the same time, the cyclic fluctuations of hydrometeorological characteristics are a process of consecutive alternating phases of increase and decrease, which leads to a stationary process in the long term. It is clear that when analyzing a relatively short series of observations, which cover only one complete cycle of fluctuations (increasing and decreasing phases) or only one phase of fluctuations, or a complete cycle with some parts of adjacent phases of fluctuations, difficulties may arise with the interpretation of the research results using only statistical tests. Thus, for the ice-appearance dates and the freeze-up, which have synchronous and in-phase fluctuations (Figs. 3 and 4), according to the Mann-Kendall test, it was found that part of the series are stationary and other parts are non-stationary (Table 4). Therefore, the complex application of statistical and graphic methods supports more reliable results.

5. Conclusions

The research presents the results of trend assessment of air temperature and ice dynamics in the Prypiat River basin within Ukraine. The observation series of the mean monthly air temperatures in November, December, and March are homogeneous. The observation series of the mean monthly air temperature in March, the ice break-up dates, the ice-disappearance dates, and their duration turned out to be quasi-homogeneous and quasi-stationary since they have only an increasing phase and a decreasing phase of long-term cyclic fluctuations. Such series were classified as non-stationary according to the Mann-Kendall statistical test, which is quite understandable because the decreasing and increasing phases have different statistical characteristics. The observation series of the mean monthly air temperature in November and December, as well as the ice-appearance dates and freeze-up dates, turned out to be homogeneous (quasi-homogeneous), and stationary (quasi-stationary). These results support statistical processing of the observations data for the ice dynamics, namely calculating their probabilistic characteristics.

The observation series of air temperature and ice dynamics have synchronous and in-phase cyclic fluctuations, which indicates the homogeneity of the conditions of their formation in the Prypiat River basin within Ukraine. The trends in air temperature determine the trends in ice dynamics. Thus, in November since 1999 and December since 2002, phases of air temperature warming caused ice appearance and freeze-up to occur later in the year. In March after 1988, the warming phase of the air temperature caused ice break-up and disappearance on rivers to occur earlier.

The application of a complex approach based on the use of statistical and graphic methods facilitates a better understanding of the formation processes of ice dynamics on rivers and better-substantiated research results.

References

- Afteniuk O.O., 2020, Dates of appearance of the main phases of the ice regime of rivers in the Pripyat basin (within Ukraine), (in Ukrainian), Proceeding IV All-Ukrainian Plain Air on Natural Sciences, 19 June 2020, Odesa, Ukraine, OSENU, 10-12.
- Allan J.D., Castillo M.M., 2007, Stream Ecology: Structure and Function of Running Waters, 2nd ed., Springer, 450 pp.
- Balabukh V., Malytska L., 2017, Estimation of modern changes in the thermal regime of Ukraine, (in Ukrainian), Geoinformatics, 4 (64), 5-20.
- Bauzha T., Gorbachova L., 2017, The features of the cyclical fluctuations, homogeneity, and stationarity of the average annual flow of the Southern Buh River basin, Annals of Valahia University of Targoviste, Geographical Series, 17 (1), 5-17, DOI: 10.1515/avutgs-2017-0001.
- Beltaos S., Burrell B., 2015, Hydrotechnical advances in Canadian river ice science and engineering during the past 35 years, Canadian Journal of Civil Engineering, 42 (9), 583-591, DOI: 10.1139/cjce-2014-0540.
- Ehlert K.W., 1972, Homogeni tets kontroll av hydrologiska tidsserier, (in Swedish), Nordisk Hydrologisk Konferanse, Sandefjord, 47-59.
- Gorbachova L., 2013, Long-term dynamics of ice phenomena in the basin of the Southern Bug River, (in Ukrainian), Hydrology, Hydrochemistry and Hydroecology, 3 (30), 21-27, available online http://www.library.univ.kiev.ua/ukr/host/viking/db/ftp/univ/ggg/ggg_2013_30 (data access 06.06.2023).
- Gorbachova L., 2014, Methodical approaches the assessment of the homogeneity and stationarity of hydrological observation series, (in Ukrainian), Hydrology, Hydrochemistry and Hydroecology, 5 (32), 22-31.

- Gorbachova L., 2015, The intra-annual streamflow distribution of Ukrainian rivers in different phases of long-term cyclical fluctuations. *Energetika*, 61 (2), 71-80, DOI:10.6001/energetika.v61i2.3134.
- Gorbachova L.O., 2016, Place and role of hydro-genetic analysis among modern research methods runoff, (in Ukrainian), Proceedings of Ukrainian Hydrometeorological Institute, 268, 73-81, available online <https://uhmi.org.ua/pub/np/268/gorbachova.pdf> (data access 06.06.2023).
- Gorbachova L.O., Afteniuk O.O., 2020, Duration of the main phases of the ice regime and their characteristics in the Prypyat River basin (within Ukraine), (in Ukrainian), Collection of scientific works of the International scientific-practical conference "Geological, Hydrological and Biological Diversities of the Polisia" to the 130th anniversary of the birth of the outstanding Polish researcher of Polissya Stanislaw Malkowski and as part of the Water Forum dedicated to the 105th anniversary of NUVGP, October 13, 2020, Rivne, NUVGP, 141-144.
- Gorbachova L., Bauzha T., 2013, Complex analysis of stationarity and homogeneity of flash flood maximum discharges in the Rika River basin, *Energetika*, 59 (3), 167-174. DOI: 10.6001/energetika.v59i3.2708.
- Gorbachova L., Khrystyuk B., 2012, The dynamics and probabilistic characteristics of the ice phenomena of the Danube River and its Kiliysky channel, [in:] *Water Resource and Wetlands*, P. Casretescu, W. Lewis., P. Bretcan (eds.), 319-324, available online <http://www.limnology.ro/water2012/Proceedings/048.pdf> (data access 06.06.2023).
- Gorbachova L., Khrystiuk B., Shpyg V., Pishniak D., 2022, Estimation of tendencies, homogeneity and stationarity of air temperature at the Ukrainian Antarctic Akademik Vernadsky station during 1951-2020, *Geofizicheskiy Zhurnal*, 44 (4), 111-122, DOI: 10.24028/gj.v44i4.264848.
- Gorbachova L., Zabolotnia T., Khrystyuk B., 2018, Homogeneity and stationarity analysis of the snow-rain floods in the Danube basin within Ukraine, *Acta Hydrologica Slovaca*, 19 (1), 35-41.
- Graf R., 2020, Estimation of the dependence of ice phenomena trends on air and water temperature in river, *Water*, 12 (12), 3494, DOI: 10.3390/w12123494.
- Hussain I., 2019, Outlier detection using graphical and nongraphical functional methods in hydrology, *International Journal of Advanced Computer Science and Applications*, 10 (12), DOI: 10.14569/IJACSA.2019.0101259.
- Kalinin M.Yu., Obodovskiy A.G. (eds.), 2003, Monitoring, use and management of water resources of the Pripjat River Basin, (in Russian), Minsk, Belsens, 269 pp.
- Kendall M.G., 1975, Rank Correlation Methods, 4th edition, Charles Griffin, London, 202 pp.
- Klemeš V., 1987, One hundred years of applied storage reservoir theory, *Water Resources Management*, 1 (3), 159-175, DOI: 10.1007/BF00429941.
- Kohler M.A., 1949, On the use of double-mass analysis for testing the consistency of meteorological records and for making required adjustments, *Bulletin of the American Meteorological Society*, 30, 188-189, DOI: 10.1175/1520-0477-30.5.188.
- Köppen W., 1936, The geographical system of the climate, (in German), [in:] *Handbook of Climatology*, W. Köppen, R. Geiger (eds.), Gebrüder Borntraeger, Berlin, 44 pp.
- Kundzewicz Z.W., Robson A. (eds.), 2000, Detecting Trend and Other Changes in Hydrological Data, World Climate Programme Data and Monitoring – WCDMP-45, WMO/TD No. 1013, 158 pp.
- Kundzewicz Z.W., Robson A.J., 2004, Change detection in hydrological records – a review of the methodology, *Hydrological Sciences Journal*, 49 (1), 7-19, DOI: 10.1623/hysj.49.1.7.53993.
- Magnuson J.J., Robertson D., Benson B., Wynne R., Livingstone D., Arai T., Assel R., Barry R., Card V., Kuusisto E., Granin N., Prowse T., Steward K., Vuglinski V., 2000, Historical trends in lake and river ice cover in the Northern Hemisphere, *Science*, 289, 1743-1746, DOI: 10.1126/science.289.5485.1743.
- Mann H.B., 1945, Nonparametric tests against trend, *Econometrica*, 13 (3), 245-259, DOI: 10.2307/1907187.
- Melnyk S., Loboda N., 2020, Trends in monthly, seasonal, and annual fluctuations in flood peaks for the upper Dniester River, *Meteorology Hydrology and Water Management. Research and Operational Applications*, 8 (2), 28-36, DOI: 10.26491/mhwm/126705.
- Merriam C.F., 1937, A comprehensive study of the rainfall on the Susquehanna Valley, *Transactions American Geophysical Union*, 18 (2), 471-476, DOI: 10.1029/TR018i002p00471.

- Novotný, J., 1925, Hydrology, (in Czech), Česká matice technická, Prague.
- Onyutha C., 2021, Graphical-statistical method to explore variability of hydrological time series, *Hydrology Research*, 52 (1), 266-283, DOI: 10.2166/nh.2020.111.
- Pekarova P., Miklánek P., Pekár J., 2003, Spatial and temporal runoff oscillation analysis of the main rivers of the world during the 19th-20th centuries, *Journal of Hydrology*, 274, 62-79, DOI: 10.1016/S0022-1694(02)00397-9.
- Prowse T.D., Bonsal B.R., 2004, Historical trends in river-ice break-up: a review, *Hydrology Research*, 35 (4-5), 281-293, DOI: 10.2166/nh.2004.0021.
- Prowse T., Bonsal B. R., Duguay C. R., Lacroix M. P., 2007, River-ice break-up/freeze-up: a review of climatic drivers, historical trends and future predictions, *Annals of Glaciology*, 46, 443-451, DOI: 10.3189/172756407782871431.
- Rachmatullina E., Grebin V., 2014, Homogeneity analysis of winter regime characteristics for the Southern Bug River basin, (in Russian), *Energetika*, 60 (3), 184-196, DOI: 10.6001/energetika.v60i3.2991.
- R Core Team, 2017, R: A language and environment for statistical computing, R Foundation for Statistical Computing, Vienna, Austria, available online <https://www.r-project.org> (data access 06.06.2023).
- Rippl W., 1883, The capacity of storage reservoirs for water supply, *Proceedings of the Institute of Civil Engineers*, 71, 270-278.
- Robson A.J., 2002, Evidence for trends in UK flooding, *Philosophical Transactions of the Royal Society A*, 360 (1796), 1327-1343, DOI: 10.1098/rsta.2002.1003.
- Rokaya P., Budhathoki S., Lindenschmidt K.-E., 2018, Trends in the timing and magnitude of ice-jam floods in Canada, *Science Report*, 8, 5834, DOI: 10.1038/s41598-018-24057-z.
- Romanova Y., Shakirzanova Z., Ovcharuk V., Todorova O., Medvedieva I., Ivanchenko A., 2019, Temporal variation of water discharges in the lower course of the Danube River across the area from Reni to Izmail under the influence of natural and anthropogenic factors, *Energetika*, 65 (2-3), DOI: 10.6001/energetika.v65i2-3.4108.
- Searcy J.K., Hardison C.H., 1960, Double-mass curves. *Manual of Hydrology: Part 1. General Surface-Water Techniques*, Geological Survey Water-Supply Paper 1541-B, Washington, United States Government Printing Office, 66 pp.
- Şen Z., 2017, Hydrological trend analysis with innovative and over whitening procedures, *Hydrological Sciences Journal*, 62 (2), 294-305, DOI: 10.1080/02626667.2016.1222533.
- Schoklitsch A., 1923, *Graphical Hydraulics*, (in German), B.G. Teubner, Leipzig.
- Smith L.C., 2000, Trends in Russian Arctic river-ice formation and breakup, 1917 to 1994, *Physical Geography*, 21 (1), 46-56, DOI: 10.1080/02723646.2000.10642698.
- Strutynska V.M., Grebin V.V., 2010, *Thermal and ice regimes of the rivers of the Dnipro basin since the second half of the 20th century*, (in Ukrainian), Kyiv, Nika-Center, 196 pp.
- Vasylenko E., 2015, Present spatial changes of time and duration of spring flooding in the Prypiat River catchment (Ukrainian part), *Energetika*, 61 (2), 81-90, DOI: 10.6001/energetika.v61i2.3135.
- Vishnevsky V.I., 2000, *Rivers and reservoirs of Ukraine. Condition and use*, (in Ukrainian), Kyiv, Vipol, 376 pp.
- Weiss L.L., Wilson W.T., 1953, Evaluation of significance of slope changes in double mass curves, *Transactions American Geophysical Union*, 34, 893-896, DOI: 10.1029/TR034i006p00893.
- WMO, 2009, *Guide to hydrological practices. Volume II: Management of water resources and application of hydrological practices*, WMO-No. 168, 6th edition, World Meteorological Organization, Geneva.
- Zabolotnia T., Gorbachova L., Khrystyuk B., 2019, Estimation of the long-term cyclical fluctuations of snow-rain floods in the Danube basin within Ukraine, *Meteorology Hydrology and Water Management*, 7 (2), 3-11, DOI: 10.26491/mhwm/99752.
- Zabolotnia T., Parajka J., Gorbachova L., Széles B., Blöschl G., Aksiuk O., Tong R., Komma J., 2022, Fluctuations of winter floods in small Austrian and Ukrainian catchments, *Hydrology*, 9 (2), 38, DOI: 10.3390/hydrology9020038.
- Yang X., Pavelsky T.M., Allen G.H., 2020, The past and future of global river ice, *Nature*, 577, 69-73, DOI: 10.1038/s41586-019-1848-1.

Assessment of global ionosphere maps in view of ionospheric correction for coastal and inland altimetry: the case for average total electron content

Wojciech Jarmolowski , Paweł Wielgosz , Anna Krypiak-Gregorczyk 

University of Warmia and Mazury in Olsztyn, Faculty of Geodesy, Geospatial and Civil Engineering

Xiaodong Ren 

Wuhan University, School of Geodesy and Geomatics

Abstract

Several low-Earth orbit (LEO) satellites are equipped with dual-frequency altimeters, theoretically scanning the entire ionosphere in the nadir direction. These two frequencies enable the determination of ionospheric delay and, thus, total electron content (TEC) below the satellite orbit. This information helps in altimetric range determination but is limited to sea and ocean areas. Therefore, global and local ionospheric models are needed for ionospheric corrections over coastal regions and lands. At the same time, altimetry-derived TEC is an important source of validation data for global navigation satellite system (GNSS)-TEC models over the oceans, where the number of GNSS stations is limited. This study compares the application of a high-resolution regional GNSS-TEC model determined from Precise Point Positioning and modeled by least-squares collocation (PPPLSC), and global ionosphere maps (GIMs), in the determination of ionospheric corrections along coastal altimetry tracks. The ionospheric delay values from 5 models are then compared with altimetry-derived TEC from 3 satellites, in the region of southeastern Asia, during a time of moderate TEC values and solar conditions.

The reason for the choice of area is that altimetric observations from coastal zones meet difficulties related to atmospheric corrections, e.g., ionospheric correction, which can be affected by the land in the altimeter footprint. For this reason, along with the rapid progress of inland satellite hydrology, we are encouraged to study the consistency of ionospheric delays in coastal regions. The study shows overall discrepancies of 30% of the entire ionospheric delay, which is 2-3 cm even in the case of 35 TEC unit ($\text{TECU} = 10^{16} \text{ el/m}^2$) values. For this reason, in the case of increased solar activity, the GIMs can have even less TEC consistency with the altimetry-derived TEC, resulting from different orbital altitudes, data gaps, and modeling techniques. The GIMs, modeled by low-order spherical harmonics, have particularly low resolution and do not represent well the equatorial ionization anomaly (EIA).

Keywords

Altimetry, ionospheric correction, Global Ionosphere Map.

Submitted 13 December 2022, revised 19 January 2023, accepted 2 March 2023

DOI: 10.26491/mhwm/161815

1. Introduction

Accurate estimation of total electron content (TEC) in the ionosphere has many applications in various domains. Some of these are GNSS positioning, applications for space weather, analysis of various traveling ionospheric disturbances (TID), e.g., co-seismic ionospheric disturbances (CID), or the determination of ionospheric correction for low-Earth orbit (LEO) satellites. This last application is investigated in this study; more precisely, the use of TEC for calculating ionospheric corrections for radar altimetry, where measuring the distance to the Earth requires especially high accuracy. This accuracy is attained partially by very accurate orbits, but a significant number of the corrections, including ionospheric correction, also should not degrade this accuracy (Fu, Cazenave 2001). Although the dual frequency altimeters determine ionospheric delay, the signal is noisy and difficult to use over inland and shallow waters. We need better

ionospheric corrections for coastal regions and for inland altimetry, which is an even more, novel geophysical field. Therefore, in this study, we compare ionospheric delays from dual-frequency altimeters and those calculated from the GIMs, which are modeled from different data densities but cover the entire Earth.

The ionospheric correction for the altimetry-derived range to the ocean can be estimated directly from dual-frequency altimeters, but single-frequency missions require TEC models for this purpose. The dual-frequency altimetry missions determine TEC and ionospheric corrections over the oceans, but leave empty places over land areas. The dual-frequency GNSS observations from ground stations are available only from sparse stations over the oceans, and therefore GNSS-based GIM is worse over the oceans. Thus, altimetry-derived TEC and GNSS-derived TEC are complementary. This means that GIMs from GNSS modeled by different techniques can be validated over the seas by TEC from altimetry, and inversely, GIMs provide ionospheric delay everywhere, including areas where determination from the altimeters is impossible.

There is a large record of studies referring to ionospheric delay acquired from altimetry and ground-based GNSS. Many studies apply these two observational techniques together with other ancillary data like Doppler Orbitography and Radiopositioning Integrated by Satellite (DORIS), GNSS from topside antennas, or occultation GNSS measurements. Some studies combine different observations in the creation of TEC models, both local ones and the GIMs. An example of combined model creation can be found in Alizadeh et al. (2011), who present a GIM modeled by spherical harmonics from the ground-based GNSS, Jason-1 altimetry, and Formosat-3/COSMIC data. The authors discuss, in particular, the effect of including altimetric data in the model. Other combinations of data, but in local ionosphere modeling, can be found in Dettmering et al. (2014), who apply B-spline functions for the interpolation of data derived from terrestrial GPS, space-based GPS, altimetry from three satellites, and very-long-baseline interferometry (VLBI). Tomographic solutions, often a starting point in the creation of 2D GIMs, are additional examples of data combinations in modeling. Tang et al. (2015) solved the problem of data insufficiency in computerized ionospheric tomography (CIT) by integrating ground-based GPS data, occultation data from low Earth orbit (LEO) satellites, satellite altimetry data from Jason-1 and Jason-2, and ionosonde data. The ionospheric delay issues were also investigated recently with respect to sea surface altimetry using the Global Navigation Satellite System Reflectometry (GNSS-R) by Yan et al. (2022), who investigated GIM as the source of ionospheric correction.

The existing studies are also focused on validating various ionosphere models with independent data, which most often comes from altimetry (Ren et al. 2019; Chen et al. 2020; Wielgosz et al. 2021). One of the oldest examples was given by Azpilicueta and Brunini (2009), who analyzed the bias between TEC from the TOPEX/Poseidon mission and GPS-based TEC. The international reference ionosphere (IRI) model was also tested by Yasukevich et al. (2009) with the altimeter-based TEC from TOPEX/Poseidon and Jason-1. The consistency of higher-accuracy, kriging-based GIM, and TEC from Jason-2 altimetry was

analyzed by Hernández-Pajares et al. (2017) using terrestrial GNSS from the stations located on the islands. Regional comparisons of TEC from Jason-1, Jason-2, and TEC based on the Crustal Motion Observation Network of China (CMONOC) were presented by Tseng et al. (2010).

These two sources of TEC, i.e., ground-based GNSS and altimetry, were most commonly interpreted as complementary over the oceans during the past two decades. The DORIS technique is the third useful technique in this area (Li, Parrot 2007). However, data coverage over the oceans available from the individual satellites receiving DORIS signals is sparser than from the single altimetry satellite (Dettmering et al. 2014). This fact could potentially be a reason for the more frequent application of altimetry in the validation of GIMs. The data implemented in the GIMs applied in this study are based on ground GNSS stations, which are mostly in continental areas. The ocean areas in GIMs are supported by GNSS stations on islands, which have sparse distribution. The satellite TEC data most frequently applied in GIM validation are DORIS, distributed over the continents and oceans, and dual-frequency altimetry TEC, available only over the oceans. However, in contrast to DORIS, satellite altimetry is independent of the stations, and therefore it provides continuous observations over entire ocean areas along the satellite footprints. The only problem is the small number of satellites, but currently, 3-4 are usually available, which is useful for validation purposes.

The validation and targeted enhancement of GIMs, with the application of dual-frequency altimetry over the oceans, requires comparison with altimetry in TEC units. On the other hand, applying GIM-based TEC in the calculation of ionospheric corrections for altimetric ranges requires conversion of the data from these two sources to cm. The interpolation of GIM used for the generation of ionospheric delay, which applies to single-frequency altimetry missions, other LEO missions, and inland altimetry, is mandatory if the satellite itself has no capability for determining the ionospheric delay. TOPEX/Poseidon, which originated in 1992, was one of the first dual-frequency altimetry missions. Therefore, ionosphere models could be validated from that time forward. Shortly after 1992, Bilitza et al. (1995) suggested that the International Reference Ionosphere model (IRI) could be used to determine ionospheric corrections for the altimeters onboard Geosat or ERS-1. They also compared IRI results to TOPEX/Poseidon ionospheric delay determinations. Komjathy and Born (1999) have studied the usefulness of ionosphere models based on the combination of GIM and IRI in the generation of ionospheric corrections for altimetry. They found errors in GIMs equivalent to 4 cm of altimetric range delay.

There are also critical applications of ionospheric correction that need accurate GIM models validated and consistent with the other sources of TEC-like dual-frequency altimetry or DORIS. It is critical to understand the errors between the GIMs and altimeters in the context of such applications as ocean-level trends or inland altimetry. The latter challenge is looming, given the upcoming SWOT mission (Biancamaria et al. 2016).

Dettmering and Schwadtke (2022) studied ionospheric delay accuracy in the context of reliable global mean sea level (GMSL). Their comprehensive study of ionospheric delay magnitude and its errors were analyzed from TOPEX and three Jason satellites (1-2-3) together with GIMs, such as NOAA Ionospheric

Climatology (NIC09). In reference to inland altimetry, Fernandes et al. (2014) studied ionospheric corrections together with other atmospheric corrections for altimetry observation of inland waters. They tested GIMs with dual-frequency altimetric determination of the delay, which is poor over inland waters, mainly due to the large footprint of the altimetric radar pulse, and land influence on the signal. The GMSL requires especially accurate atmospheric corrections if we want to assess its trends in the short-time window. Single-frequency altimeters contribute much to this field, but need GIM-based ionospheric delay over areas where ground GNSS stations are sparse. For inland altimetry, the challenge is in determining the correct ranges where the ranging is disturbed by the presence of land. The determination of ionospheric delay from dual-frequency altimeters can be even harder inland. If we want to use GIMs, we must remember that even if GIMs use more continental ground GNSS stations, we can validate them with altimetry only in coastal zones. The comparative study of 5 models and 3 altimeters reported here was performed to provide several numerical results useful for future studies of these demanding applications.

2. Altimetry-derived ionospheric delay vs. that recalculated from Global Ionosphere Maps

Dual-frequency radar altimeters penetrate the ionosphere by first sending an electromagnetic pulse through the atmosphere, and then measuring the received response after the pulse is reflected by the ocean and propagates back to the satellite. The application of two frequencies enables the determination of ionospheric delay of pulse propagation transmitted across the ionosphere below the satellite orbit, an altitude of 1300 km for Jason satellites, and 800 km for Sentinel 3 satellites. Dual-frequency altimeters use shorter wavelengths than GNSS for determining the ionospheric correction. The radar altimeters used for Jason-2, Jason-3, and Sentinel-3 missions transmit pulses alternatively at the K_u -band (around 13.6 GHz), the main frequency for altimeter range measurements, complemented by a C -band frequency (around 5.3 GHz) that is used to correct range delay. The ionospheric correction for the range R is given for the two frequencies by the following equations:

$$ionocorr_{Ku} = \delta f_{Ku}(R_{Ku} - R_C) \quad (1)$$

$$ionocorr_C = \delta f_C(R_{Ku} - R_C)$$

where:

$$\delta f_{Ku} = \frac{f_C^2}{f_{Ku}^2 - f_C^2} \quad (2)$$

$$\delta f_C = \frac{f_{Ku}^2}{f_{Ku}^2 - f_C^2}$$

where f_{Ku} and f_C are respective frequencies (in Hz). The relation between TEC and ionospheric delay for the K_u -band frequency translates to about 2 mm in altitude for each TEC unit. The frequency ranges, ocean behavior, and other factors cause TEC values derived from the altimetric ranging to be character-

ized by significant noise, which affects the output accuracy of filtered TEC, typically by 1-2 TECU. Therefore, the filtering process has always to be applied. Because of the random character of the noise, a filter based on the moving average is often applied in practice (Hernández-Pajares et al. 2017). The window size of the moving average determines the spatial resolution of the ionospheric correction along the orbital footprint in the spectral sense, i.e., the longer the window, the longer-wavelengths of the signal can be kept. The average filtering of ionospheric delay measured along three selected tracks from three satellites is shown in Figure 1. The window size is here 80 s, which is equivalent to a ~ 465 km footprint at sea level or ~ 575 km at orbital altitude. Such filtered ionospheric delays are applicable in the computation of corrected altimetric ranges.

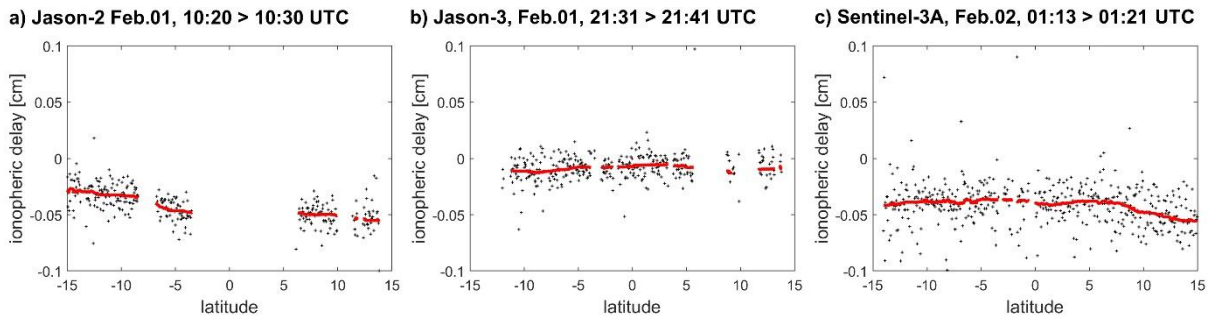


Fig. 1. Selected tracks of altimetry-derived Ku -band ionospheric delay determination (black) and its smoothing by moving average with 80 s window (red).

The delay of pulse propagation induced by the ionosphere is proportional to TEC. Since ionization in the upper part of the atmosphere is primarily caused by solar ultraviolet radiation, spatial and temporal variability in the ionospheric correction is linked to solar conditions. The ionospheric corrections $ionocorrGIM_{Ku}$ and $ionocorrGIM_C$ can be obtained from the GIM by using the first-order expansion of the refraction index (Dettmering et al. 2011):

$$ionocorrGIM_{Ku} = -40300 \frac{TEC}{f_{Ku}^2} \quad (3)$$

$$ionocorrGIM_C = -40300 \frac{TEC}{f_C^2}$$

where f_{Ku} and f_C are respective frequencies (in Hz), and TEC is expressed in electrons/m². Since the relationship between TEC and ionospheric delay is proportional, the sources of GIM-altimetry inconsistency that come from the GIMs are the interpolation of the GIM, the spatiotemporal resolution of the GIM, and its quality depending on the data and methods used. The additional bias between the GIM TEC and altimetry-derived TEC can originate from the orbital altitudes of altimetric satellites, which are different from GNSS satellite altitudes. The shapes of vertical electron density profiles have a variety of interpretations in the literature, differing much between day and night, and therefore it is not easy to derive the top-side TEC above the altimetric orbits from the models. Wielgosz et al. (2021) determined that even though

adding model-derived plasmaspheric TEC does not change the standard deviation of TEC differences between the GIMs and altimetry by much, the systematic error between these two sources can reach 2 TECU, which together with filtering errors (Fig. 1) can contribute to ionospheric delay differences derived from these two techniques.

The local model was developed by the authors of this study using point TEC determination from Precise Point Positioning (PPP) (Li et al. 2013; Jarmolowski et al. 2019). The grid values were then interpolated spatially in separate epochs by least-squares collocation (LSC), and the model with spatial resolution of $1^\circ \times 1^\circ$ and temporal resolution of 5 min. was designated PPPLSC. The other TEC models used in the study come from IGS associate analysis centers, and contribute to the official IGS GIM, or are unique in terms of spatiotemporal resolution or modeling method, like UQRG. The UQRG global model, based on ordinary kriging, usually performs better compared with altimetry from the other models (Roma-Dollase et al. 2018; Wielgosz et al. 2021). CODG and IGSG global models based on spherical harmonics are official and popular models contributing to IGS. The JPLG model is embedded in altimetry data as a background model for dual-frequency altimetry-based delays. In this work, the altimetry trajectory samples and GIM grids are selected in the equatorial area between latitudes 15°N and 15°S , and between longitudes 90°E and 150°E (Fig. 2).

The standard spatial resolution of GIM grids is 5° in longitude and 2.5° in latitude. Temporal resolutions vary by the model. The JPLG and IGSG models have 2-hour resolution, CODG has a 1-hour interval, and UQRG has a time interval of 15 min., whereas the authors' model PPPLSC working version was used with 5 min. resolution. However, the spatial resolution of the grids doesn't mean that the model includes these spatial details of the TEC signal, which correspond to grid node separation. This drawback refers, in particular, to models created based on mathematical base functions, when lower orders of these functions are applied (e.g., spherical harmonics). In referring to lower orders, we mean the orders that correspond to resolution much lower than the grid resolution. Therefore the choice of modeling method is very important. The stochastic methods are more robust, as they avoid loss of resolution in the places where the data are dense, and do not cut the higher-order TEC details contrary to low-order spherical basis functions. The GIMs are typically based on GNSS data from various numbers of ground stations. The number of these stations is usually >200 , but separated stations in regions of sparse data are always included, as a priority. The authors' model PPPLSC, based on GPS data, has applied LSC, which is equivalent to simple kriging in the interpolation (Krypiak-Gregorczyk et al. 2017). The other model assessed in this study, which is interpolated by a stochastic technique, is UQRG from the Polytechnic University of Catalunya, and it applies ordinary kriging to GPS ground data (Orús et al. 2005). The JPLG model from Jet Propulsion Laboratory uses a set of horizontal basis function coefficients (Komjathy et al. 2005) for the interpolation of ground GPS/GLONASS data. The CODG model created by The Center for Orbit Determination in Europe also uses GPS/GLONASS data and interpolation by spherical harmonics expansion up to

degree and order 15 (Schaer et al. 1996). IGS GIM is a combination of different GIMs (Hernández-Pajares et al. 2009). Figure 2 depicts a selected epoch of local grids extracted from 4 of 5 GIMs discussed in this work, because JPLG data were interpolated along the satellite track directly in the altimetry L2 data.

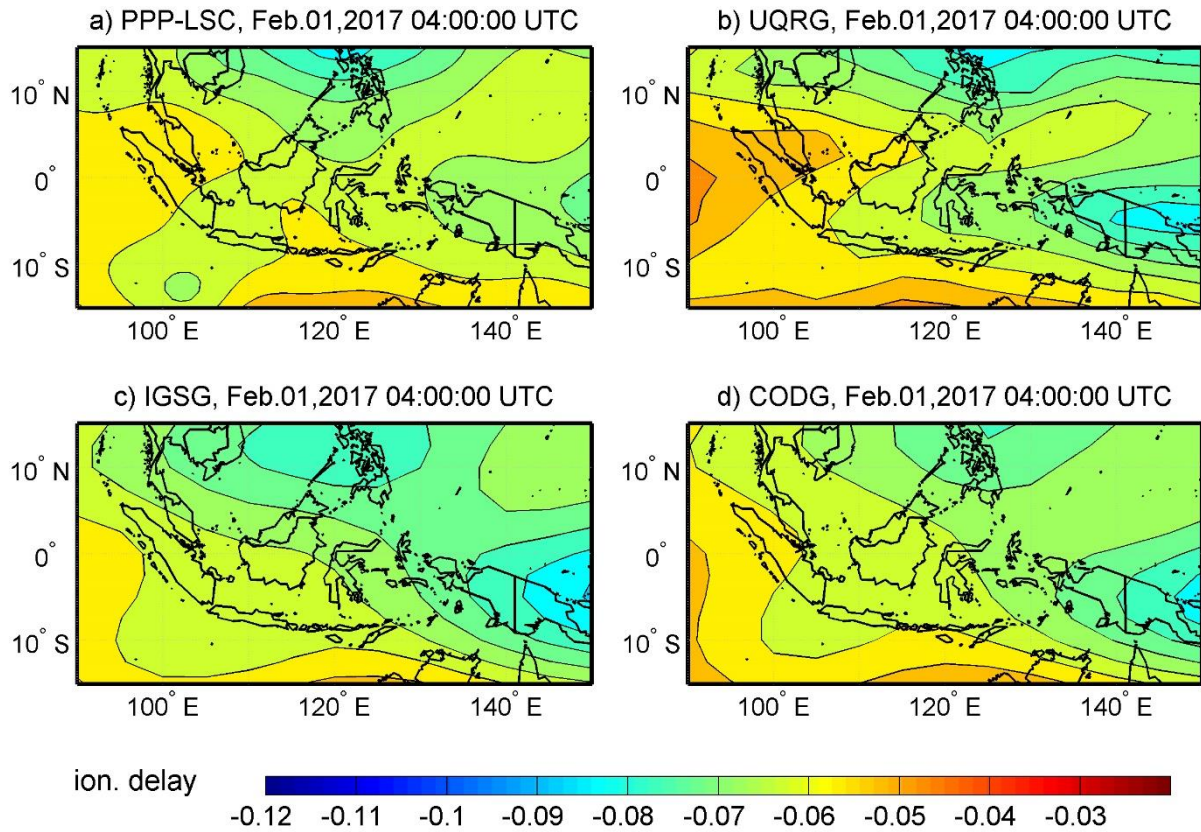


Fig. 2. The contours of GIMs in an example epoch, in cm of K_u -band ionospheric delay.

The altimetry data selected for the study (Jason-2, Jason-3, and Sentinel-3A) include observations between February 1st and 5th, 2017. The area of the analysis is located in the EIA region, which is challenging in the modeling, especially from the sparse data. However, the period selected does not include enhanced solar activity (solar radio flux at F10.7 was dropping slowly from 77 s.f.u.), and TEC magnitudes are moderate. The length of the coastline, together with equatorial TEC properties, makes this region interesting for coastal studies of ionospheric corrections. Additional occurrence of large Mean Dynamic Topography (MDT) variability can make the observations from this area interesting for studies related to atmospheric corrections.

3. Review of GIMs in the coastal region where Equatorial Ionization Anomaly (EIA) occurs, with respect to ionospheric correction

The assessment of the ionospheric corrections from the altimeters and GIMs starts from the comparative assessment of this quantity along the selected trajectories of 3 altimetric satellites. The TEC values at the time and place of the selected tracks (low latitudes in 2017) are typically between 20-40 TECU, which is 4 times smaller than typical values, e.g., in the year 2002 (TEC in 2002 locally reached 150 TECU and solar

radio flux at F10.7 varied from 140 to 260 s.f.u.). This means that the ionospheric correction values, as well as differences between their estimates from different sources, can be larger than the ones determined in this study. Therefore, this study refers to average conditions in terms of TEC and ionospheric delay size.

First, five profiles of satellite tracks having the largest differences between altimetry-derived ionospheric corrections and those interpolated and calculated from the GIMs are analyzed. Figures 3-5 show along-track ionospheric corrections from the altimetry and the five selected TEC models. The ionospheric corrections from dual-frequency altimeters placed onboard three satellites are filtered by the median filter with an 80 s window, and then compared with the corrections calculated from the GIMs. As noted, JPLG GIM is available as a standard GIM model for Ku-band and C-band ionospheric corrections in the Level 2 altimetry data, and therefore we took its values directly from the altimetry data files. The surface flags available in L2 altimetry data are used to indicate the occurrence of the land, but they indicate only coastal land in the case of S3A, as the data come from a marine data set, where land is excluded (Fig. 5b-f, right). The flags indicate the locations of the land in Figures 3-5. The left sub-figures in Figures 3-5 (b-f) present TEC interpolated along the track from the PPPLSC model to review its proportional relation with ionospheric correction. The right sub-figures in Figures 3-5 (b-f) show the size of the ionospheric delay that affects range measurements. It should be pointed out that TEC here values reach only 40 TECU, but can reach or exceed 100 TECU in more active solar phases.

Figures 3b-f present ionospheric delays reaching 7-8 cm in the case of the largest TEC values (30-40 TECU). The black curves representing altimetry-derived delays are the most detailed, as they were not modeled, but only filtered. Thus, altimetry-derived ionospheric delays include the largest amount of the signal at the high-frequencies, unavailable in the case of GIMs. This finding also means that the filtering of altimetry-derived ionospheric delays by the moving average with an 80 s window still preserves more high frequencies than GIM models. This is true if we are aware that this window spans 400-500 km, whereas the GIMs are based on very sparse data in the oceans. Therefore, even stochastic modeling, although it can be more accurate in the least-squares sense, cannot extend the resolution. Additionally, the true resolution represented by spherical harmonics of degree 15 is much worse than 1000 km. Knowing the nature of stochastic modeling methods, like different types of kriging, we can expect more local details from PPPLSC and UQRG models than from JPLG, CODG, and IGSG, but rather in continental or coastal areas. This is confirmed especially in Figures 3d and 3f, where TEC from different models differs more along the Jason-2 tracks. The altimetry-derived delays have more composed curvatures along these trajectories, and PPPLSC and UQRG follow these curves, but the remaining three models (JPLG, CODG, and IGSG) do not follow these shapes and are flatter. Surprisingly, JPLG ionospheric delay is the most divergent from the altimetric one, which suggests that it is not the best choice as a supplement for altimetry; the values diverge in the coastal regions by as much as 3 cm. Such differences are larger than the total ionospheric correction at some higher latitudes or at some other time of the day. In the case of lower TEC

values (around 20 TECU), the differences between different sources of ionospheric delay reach nearly 2 cm (Fig. 3c and 3e), which is almost half of the ionospheric delay itself.

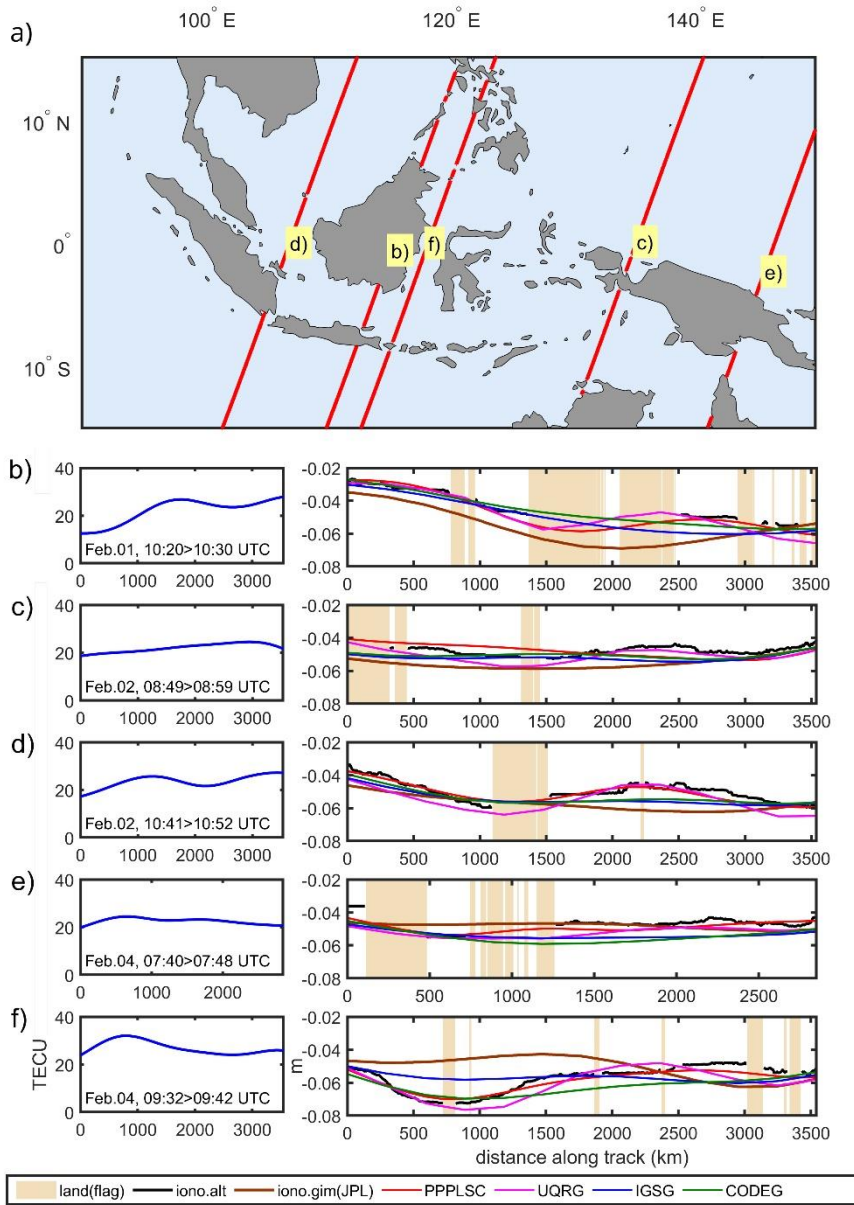


Fig. 3. a) Selected tracks of Jason-2 having the largest analyzed differences between K_u -band ionospheric corrections from altimetry and GIMs. b-f) Along-track TEC values interpolated from the PPPLSC model (left). Ionospheric corrections for K_u -band along selected passes (right) from filtered dual-frequency altimetry (black), JPLG GIM available in altimetric L2 datasets (brown) and interpolated from PPPLSC (red), UQRG (magenta), IGSG (blue) and CODG (green). Light brown bars show land derived from surface flags.

The case of Jason-3 (Fig. 4) confirms the smoothness and lower order of spatial details of JPLG, CODG, and IGSG with respect to altimetry-derived delays, as well as more fitted shapes of the stochastic-based models (Fig. 4d and 4f). This fit is assessed based on the altimetry-derived delay, which includes the highest frequencies of the signal. The worst correspondence of JPLG with altimetry-derived delays is also

again noticeable (Fig. 4e and 4f). The altimetry-based ionospheric delay from Jason-3 is even more divergent from the values interpolated from all the selected models, which can indicate some bias; this bias will also be confirmed in Section 4. The differences between the altimetry and GIMs in ionospheric delay units reach 2-3 cm, and it should be recalled that we are not working with the highest TEC values.

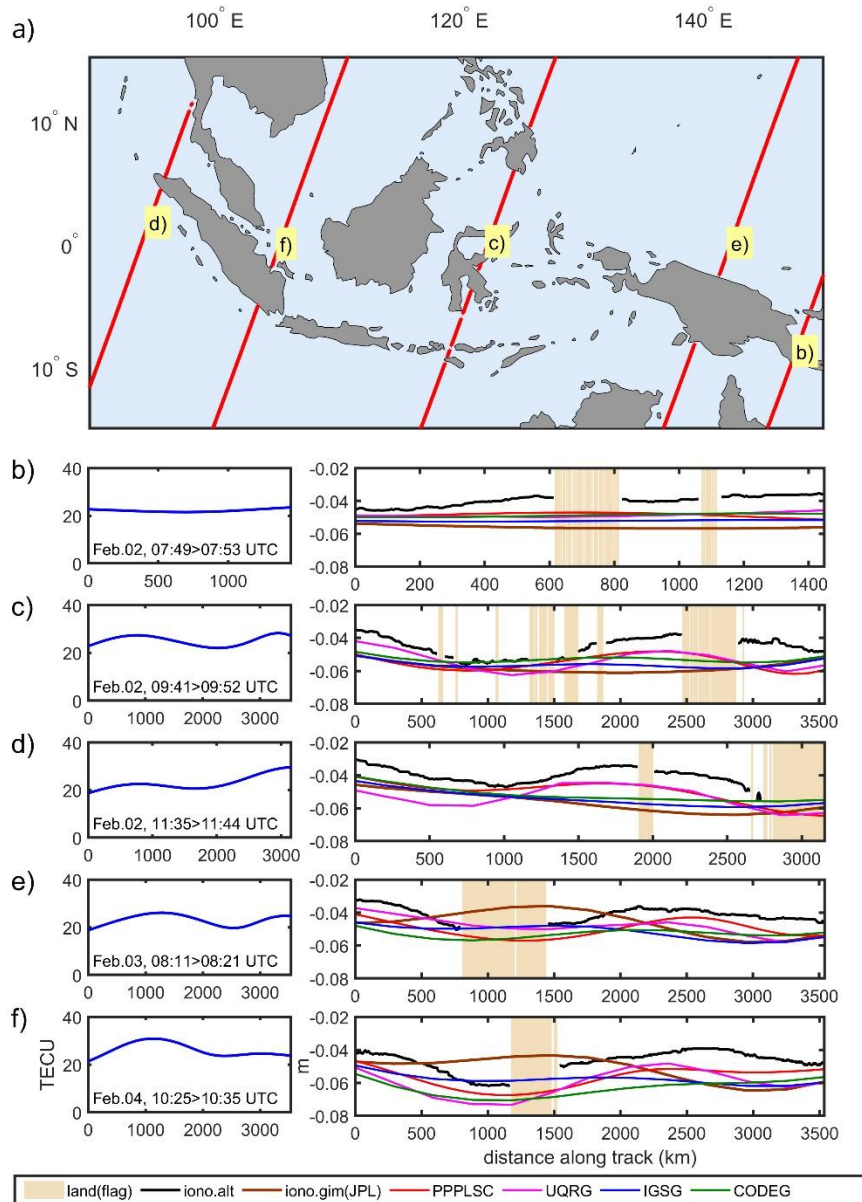


Fig. 4. The same as in Fig. 3 but for the Jason-3 satellite.

The selected Sentinel-3A trajectories represent slightly lower levels of TEC, and this turned out to be helpful in the assessment of GIMs under conditions of calmer TEC behavior. Contrary to Figures 3-4, Figures 5b and 5e indicate better correspondence of the JPLG model with dual-frequency altimeter measurements along the selected tracks. Figures 5c-d and 5f show TEC values below 20 TECU, when the delay is small. These examples are very useful in the analysis because they prove that harmonic modeling can be effective only under conditions of lower TEC variability. From previous observations (Figures 3-4), where

we have a more pronounced EIA crest and better performance of stochastic models, it can be concluded that GIMs based on the spherical basis functions need more harmonic degrees in the EIA regions.

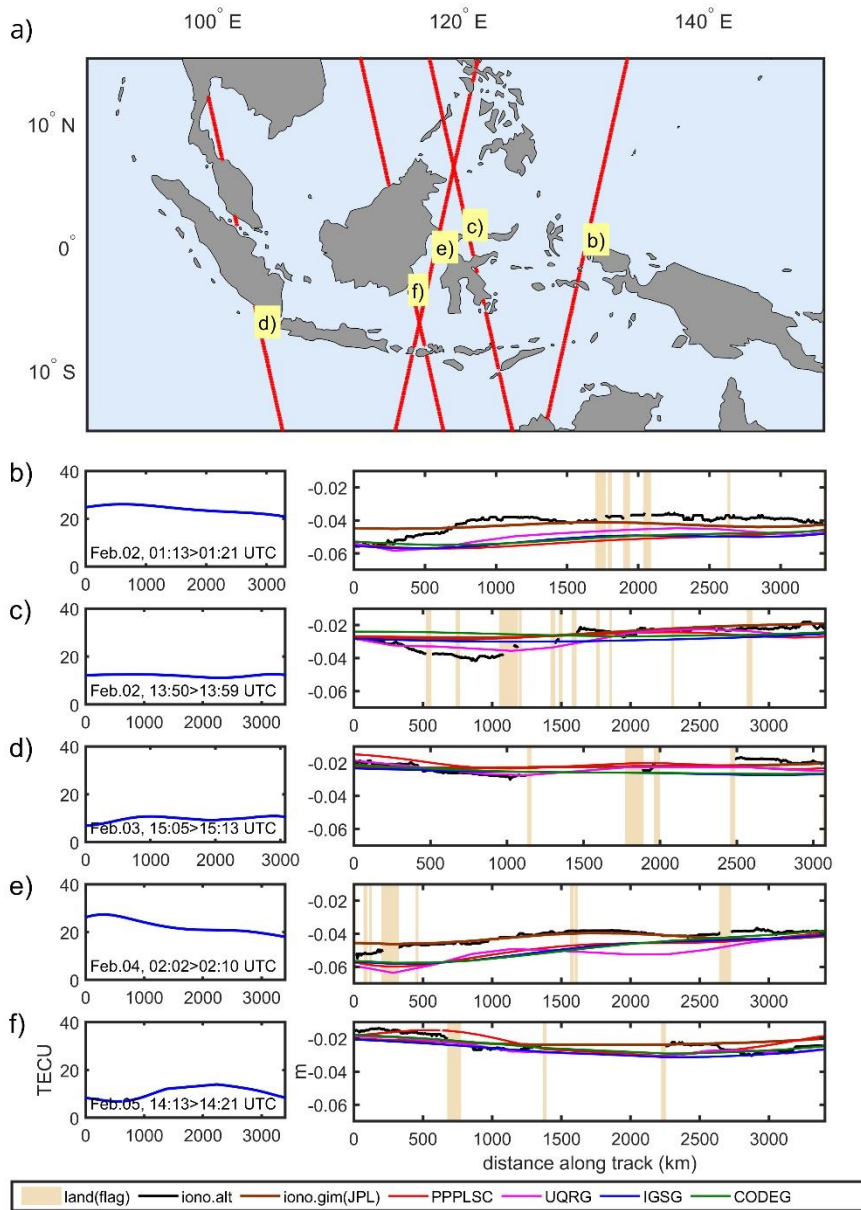


Fig. 5. The same as in Fig. 3 but for the Sentinel-3A satellite. Light brown bars show land derived from surface flags, but only in coastal regions for S3A, because marine data with excluded land is used.

4. Ionospheric correction from altimetry vs. that from GIMs – results in EIA coastal regions

All the available along-track satellite footprints for 5 days in the selected coastal area are summarized in this section to measure the scale of discrepancies between different types of ionosphere models and different altimeters. The statistical values are calculated under conditions of moderate TEC with respect to the phase of the solar cycle, but the most variable with respect to the latitude, as located in the EIA region. The differences between ionospheric delay from 3 altimetry satellites and that interpolated along the

tracks from 5 TEC models are calculated. Then minima, maxima, standard deviation, and RMS of differences are calculated for all models and satellites (Table 1). However, the graphics are limited only to TEC models having extreme differences (UQRG and JPLG) and the local author's model PPPLSC (Fig. 6-8) to avoid figures showing comparable values. Overall, the ionospheric delay differences between altimetry and GIMs, and also between the GIMs themselves, reach 2-3 cm in the case of TEC at ~ 30 TECU. The study is performed in the region of EIA, and therefore the size of ionospheric corrections, as well as differences between different models, would be smaller at higher latitudes. On the other hand, TEC values can reach 100 TECU in times of stronger solar activity or ionospheric storms, and the discrepancies can be much larger than 3 cm. For this reason, the improvement of GIM accuracy for ionospheric delay calculation in altimetry is still an open challenge. We have to remember that there is an increased need for the application of GIMs in the coastal region, as the ionospheric correction can be affected by land in the altimeter footprint (Andersen, Scharroo 2011).

Figures 6-8 present the comparisons of ionospheric delay along the tracks of 3 satellites and for 3 out of 5 models, and their basic statistical value, RMS. Two of these GIMs indicate extreme statistics (best and worst RMS), whereas the third plotted model is the author's PPPLSC. Five days of observations, taken for the comparisons and calculated RMS, confirm previous findings related to GIM included in altimetric Level 2 products (JPLG). Figures 6-7 show worse fits of Jason-2 and Jason-3 with the JPL model and better consistency with PPPLSC and UQRG. A different result can be found in Figure 8, where JPLG performs similarly to the other two models. However, we note that Sentinel-3A passes over the selected region on the selected days were at a time of lower and much less variable TEC. The suggestion is that low-order harmonics of JPLG are determined with good accuracy, and the deficiency in higher-order terms limits the real total resolution of the JPLG model in terms of high-order details.

Table 1 presents 6 statistical values referring to the 5-day comparison of ionospheric delays from the altimetry and GIMs. At the beginning, we note that means and medians do not exceed 3 mm for Jason-2 and 5 mm for Sentinel-3A, and this refers to all TEC models. Thus, the systematic bias between GIMs and these two satellites does not exceed 2.5 TECU in the selected region. However, the means and medians in comparison of GIMs with Jason-3 approach 9 mm, which is close to 4.5 TECU. Nevertheless, the mean and median of differences between Jason-3 and PPPLSC is 5.5 mm, which means that it is possible to be closer with mean value to Jason-3, namely <3 TECU. Overall, the lowest standard deviations and RMS are found in the comparison between UQRG and PPPLSC, but this is valid for Jason-2 and Jason-3, where a more significant influence of EIA has been found along the altimetric tracks. The indication is that this region needs more than 15 spherical harmonic degrees in the interpolation of TEC in the EIA region or the application of stochastic techniques. The comparison with Sentinel-3A is likely to confirm this, as the RMS and standard deviations are very comparable for all TEC models in the case of comparison with this satellite, contrary to Jason satellites, where EIA is more evident. Referring to maxima and minima in comparison with Sentinel-3A, we see that although they decreased with respect to the comparison with Jason-2 and Jason-3, their values still reach or even exceed 2 cm. On the other hand, the normal

distribution of the residuals, which is most frequently observed in the statistics, can suggest multiplying the standard deviation at least by 2, to obtain a representative size of the errors at a 95% confidence level. This would give approximately 2 cm errors between the altimetry and GIMs, when the ionospheric delay for the K_u -band would be 6 cm, equivalent to 30 TECU. This is one-third of the ionosphere correction for the altimetry.

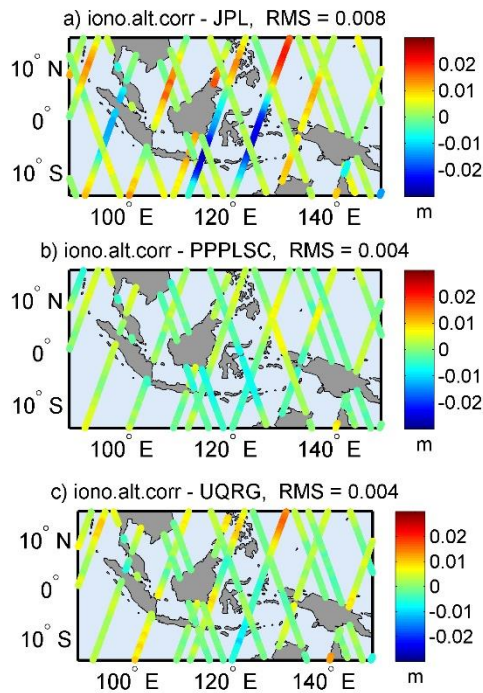


Fig. 6. Differences of ionospheric corrections between Jason-2 altimetry-derived (K_u -band) and the corrections interpolated from 3 selected GIMs (JPL, PPPLSC, and UQRG).

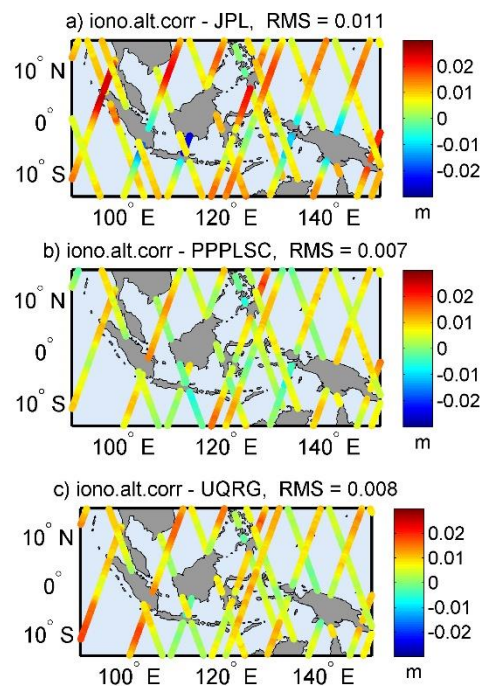


Fig. 7. The same as in Figure 6 but for the Jason-3 satellite.

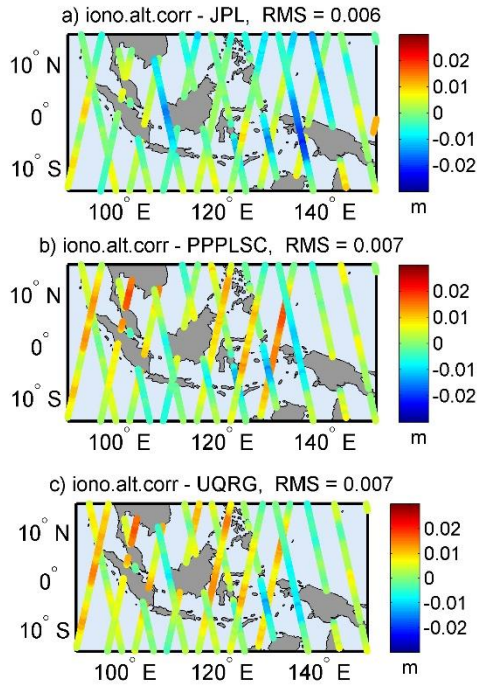


Fig. 8. The same as in Figure 6 but for the Sentinel-3A satellite.

Table 1. All statistical values from the comparison of ionospheric corrections from 3 altimeters and 5 GIMs (meters).

Jason-2	Min.	Max.	Mean	Median	St. Dev.	RMS
JPL	-0.0270	0.0214	0.0020	0.0028	0.0079	0.0082
PPPLSC	-0.0085	0.0096	0.0000	-0.0003	0.0035	0.0035
UQRG	-0.0113	0.0171	0.0013	0.0010	0.0041	0.0043
IGSG	-0.0148	0.0165	0.0026	0.0023	0.0051	0.0057
CODG	-0.0083	0.0145	0.0020	0.0009	0.0043	0.0048
Jason-3						
JPL	-0.0256	0.0263	0.0082	0.0083	0.0072	0.0109
PPPLSC	-0.0080	0.0205	0.0055	0.0055	0.0045	0.0071
UQRG	-0.0060	0.0190	0.0071	0.0068	0.0044	0.0084
IGSG	-0.0138	0.0228	0.0089	0.0085	0.0054	0.0104
CODG	-0.0065	0.0215	0.0078	0.0068	0.0051	0.0093
Sentinel-3A						
JPL	-0.0218	0.0121	-0.0013	-0.0004	0.0059	0.0060
PPPLSC	-0.0159	0.0184	0.0028	0.0030	0.0063	0.0069
UQRG	-0.0150	0.0179	0.0034	0.0037	0.0057	0.0066
IGSG	-0.0147	0.0192	0.0044	0.0048	0.0061	0.0075
CODG	-0.0166	0.0205	0.0032	0.0034	0.0061	0.0069

5. Conclusions

The ionospheric correction filtered from dual-frequency altimetry retains more high-resolution information about the ionosphere along the satellite track than can be interpolated from the GIM. The reasons are (1) the sparse distribution of ground GNSS over the ocean, and (2) modeling with spherical basis functions, e.g., spherical harmonics. This study indicates that low-order spherical basis functions generate unacceptably large errors, which, when used for inland altimetry, can adversely affect the equatorial regions

more than stochastic modeling of these delays. Therefore, the profiles of ionospheric delays interpolated from the models based on stochastic techniques (PPPLSC, UQRG) have shapes most comparable to altimetry-derived delays in the close vicinity of EIA. The stochastic modeling techniques can provide advantages in real resolution and accuracy, especially in regions of denser data, like continental and coastal regions. Together with the difference in real spatial resolution between the altimetric observation of K_{ir} -band ionospheric delay, and interpolation of this delay from the GIM, we observe significant discrepancies between these two sources, up to 30% of the entire ionospheric correction. Namely, the differences between ionosphere corrections from different sources reach 2-3 cm in the case of TEC, ~ 30 -35 TECU. The magnitude of TEC was moderate there at that time of the solar cycle, but the data were selected from the EIA region. Therefore, ionosphere corrections and differences between the models can be larger in the case of stronger solar activity with greater TEC. We can also expect correspondingly larger discrepancies in ionospheric delay acquired from different data sources.

Knowing that ionospheric delay from the GIMs can be subject to errors of several cm, the selection of GIM complementary to dual-frequency altimetry requires special care in coastal areas. Coastal and inland altimetry, along with the ionosphere corrections, can be extremely hard to assess from dual-frequency altimeters, especially over inland waters. Inland altimetry should undergo extensive progress in the coming years, when the planned SWOT mission, with the next generation of altimeter, will be a substantial milestone in the field. The GIMs are better over land because inland regions usually have dense GNSS station coverage. Nevertheless, the bias between the GIM and altimetry has to be eliminated, along with that from the modeling errors. The removal of the plasmaspheric TEC from the GIMs is also crucial, as there are some additional electrons to remove, especially above the 800 km orbit of Sentinel satellites.

The generally recommended actions for gaining more consistency between dual-frequency altimetry and GIMs, and assuring, say, compatibility at the level of 6 mm for the K_{ir} -band (3 TECU), are constant employment of new GNSS ground stations and all other available data in GIM creation. The selection of the data must include a range of satellite data: DORIS, topside TEC from POD, occultation data, and also altimetry because ground data will never be sufficiently dense in the open ocean. It is also important to keep some data unused for validation purposes. The best validation data would be of high accuracy, and redundant at the specified location, so that their removal does not affect the models. Being aware of the unavoidable data gaps, the modeling techniques must be carefully selected, and implementation of stochastic techniques is advised, at least in combination with spherical basis functions. Another recommendation worth consideration follows from the validation of GIM models by the satellite altimetry tracks. Namely, the fitting of a GIM model into altimetry-derived TEC could be considered, to obtain a coincident reference level suitable for altimetry and other applications. A similar solution was extensively used in geodesy for the gravimetric geoid models, which were fitted to independent geometric geoid values coming from leveling and GNSS positioning. By these means, the continuous surface from the GIM can achieve the reference level compatible with TEC measured by the altimeter.

Acknowledgments

The study is supported by grant no. UMO-2017/27/B/ST10/02219 from the Polish National Center of Science. The authors wish to thank two anonymous reviewers and also the editor for very useful comments, which substantially enhanced the study.

References

- Andersen O.B., Scharroo R., 2011, Range and geophysical corrections in coastal regions: and implications for mean sea surface determination, [in:] Coastal Altimetry, S. Vignudelli, A. Kostianoy, P. Cipollini, J. Benveniste (eds.), Springer, Berlin, Heidelberg, 103-145, DOI: 10.1007/978-3-642-12796-0_5.
- Alizadeh M.M., Schuh H., Todorova S., Schmidt M., 2011, Global ionosphere maps of VTEC from GNSS, satellite altimetry, and formosat-3/COSMIC data, *Journal of Geodesy*, 85, 975-987, DOI: . 10.1007/s00190-011-0449-z.
- Azpilicueta F., Brunini C., 2009, Analysis of the bias between TOPEX and GPS vTEC determinations, *Journal of Geodesy*, 83, 121-127, DOI: 10.1007/s00190-008-0244-7.
- Biancamaria S., Lettenmaier D.P., Pavelsky T.M., 2016, The SWOT mission and its capabilities for land hydrology, *Surveys in Geophysics*, 37, 307-337, DOI: 10.1007/s10712-015-9346-y.
- Bilitza D., Koblinsky C., Beckley B., Zia S., Williamson R., 1995, Using IRI for the computation of ionospheric corrections for altimeter data analysis, *Advances in Space Research* 15(2), 113-119, DOI: 10.1016/S0273-1177(99)80032-5.
- Chen P., Liu H., Ma Y., Zheng N., 2020, Accuracy and consistency of different global ionospheric maps released by IGS ionosphere associate analysis centers, *Advances in Space Research*, 65 (1), 163-174, DOI: 10.1016/j.asr.2019.09.042.
- Dettmering D., Limberger M., Schmidt M., 2014, Using DORIS measurements for modeling the vertical total electron content of the Earth's ionosphere, *Journal of Geodesy*, 88, 1131-1143, DOI: 10.1007/s00190-014-0748-2.
- Dettmering D., Schwatke C., 2022, Ionospheric corrections for satellite altimetry – impact on global mean sea level trends, *Earth and Space Science*, 9 (4), DOI: 10.1029/2021EA002098.
- Fernandes M., Lázaro C., Nunes A., Scharroo, R., 2014, Atmospheric corrections for altimetry studies over inland water, *Remote Sensing*, 6 (6), 4952-4997, DOI: 10.3390/rs6064952.
- Fu L., Cazenave A., 2001, *Satellite altimetry and earth sciences: a handbook of techniques and applications*, San Diego: Academic Press, 460 pp.
- Hernández-Pajares M., Juan J., Sanz J., Orus R., García-Rigo A., Feltens J., Komjathy A., Schaer S., Krankowski A., 2009, The IGS VTEC maps: a reliable source of ionospheric information since 1998, *Journal of Geodesy*, 83 (3-4), 263-275, DOI: 10.1007/s00190-008-0266-1.
- Hernández-Pajares M., Roma-Dollase D., Krankowski A., García-Rigo A., Orús-Pérez R., 2017, Methodology and consistency of slant and vertical assessments for ionospheric electron content models, *Journal of Geodesy*, 91, 1405-1414, DOI: 10.1007/s00190-017-1032-z.
- Jarmolowski W., Ren X., Wielgosz P., Krypiak-Gregorczyk A., 2019, On the advantage of stochastic methods in the modeling of ionospheric total electron content: South-East Asia case study, *Measurement Science and Technology*, 30 (4), DOI: 10.1088/1361-6501/ab0268.
- Komjathy A., Born G.H., 1999, GPS-based ionospheric corrections for single frequency radar altimetry, *Journal of Atmospheric and Solar-Terrestrial Physics*, 61 (16), 1197-1203, DOI: 10.1016/S1364-6826(99)00051-6.
- Komjathy A., Sparks L., Wilson B.D., Mannucci A.J., 2005, Automated daily processing of more than 1000 ground-based GPS receivers for studying intense ionospheric storms, *Radio Science*, 40 (6), DOI: 10.1029/2005RS003279.
- Krypiak-Gregorczyk A., Wielgosz P., Jarmolowski W., 2017, A new TEC interpolation method based on the least squares collocation for high accuracy regional ionospheric maps, *Measurement Science and Technology*, 28 (4), DOI: 10.1088/1361-6501/aa58ae.
- Li F., Parrot M., 2007, Study of the TEC data obtained from the DORIS stations in relation to seismic activity, *Annals of Geophysics*, 50 (1), 39-50, DOI: 10.4401/ag-3086.

- Li X.X., Ge M.R., Zhang H.P., Wickert J., 2013, A method for improving uncalibrated phase delay estimation and ambiguity fixing in real-time precise point positioning, *Journal of Geodesy*, 87, 405-416, DOI: 10.1007/s00190-013-0611-x.
- Orús R., Hernández-Pajares M., Juan J., Sanz J., 2005, Improvement of global ionospheric VTEC maps by using kriging interpolation technique, *Journal of Atmospheric and Solar-Terrestrial Physics*, 67 (16), 1598-1609, DOI: 10.1016/j.jastp.2005.07.017.
- Roma-Dollase, D., Hernández-Pajares M., Krankowski A., Kotulak K., Ghoddousi-Fard R., Yuan Y., Li Z., Zhang H., Shi C., Wang C., Feltens J., Vergados P., Komjathy A., Schaer S., Garcis-Rigo A., Gomez-Cama J., 2018, Consistency of seven different GNSS global ionospheric mapping techniques during one solar cycle, *Journal of Geodesy*, 92, 691-706, DOI: 10.1007/s00190-017-1088-9.
- Ren X., Chen J., Li X., Zhang X., Freeshah M., 2019, Performance evaluation of real-time global ionospheric maps provided by different IGS analysis centers, *GPS Solutions*, 23, DOI: 10.1007/s10291-019-0904-5.
- Schaer S., Beutler G., Rothacher M., Springer T.A., 1996, Daily global ionosphere maps based on GPS carrier phase data routinely produced by the CODE Analysis Center, [in:] *Proceedings of the IGS AC workshop*, Silver Spring, MD, USA, 181-192, available online at <https://mediatum.ub.tum.de/doc/1365743/254480.pdf>.
- Tang J., Yao Y., Zhang L., Kong J., 2015, Tomographic reconstruction of ionospheric electron density during the storm of 5-6 August 2011 using multi-source data, *Scientific Reports*, 5, DOI: 10.1038/srep13042.
- Tseng K.H., Shum C.K., Yi Y., Dai C., Lee H., Bilitza D., Komjathy A., Kuo C.Y., Ping J., Schmidt M., 2010, Regional validation of Jason-2 dual-frequency ionosphere delays, *Marine Geodesy*, 33, 272-284, DOI: 10.1080/01490419.2010.487801.
- Wielgosz, P., Milanowska, B., Krypiak-Gregorczyk A., Jarmolowski W., 2021, Validation of GNSS-derived global ionosphere maps for different solar activity levels: case studies for years 2014 and 2018, *GPS Solutions*, 25, DOI: 10.1007/s10291-021-01142-x.
- Yan Z., Zheng W., Wu F., Wang C., Zhu H., Xu A., 2022, Correction of atmospheric delay error of airborne and spaceborne GNSS-R sea surface altimetry, *Frontiers in Earth Science*, 10, DOI: 10.3389/feart.2022.730551.
- Yasukevich Y.V., Afraimovich É.L., Palamarchuk K.S., Tatarinov P.V., 2009, Testing of the international reference ionosphere model using the data of dual-frequency satellite altimeters “Topex”/”Poseidon” and “Jason-1”, *Radiophysics and Quantum Electronics*, 52 (5-6), DOI: 10.1007/s11141-009-9137-8.

Assessing the impact of climate change on discharge in the Horyn River basin by analyzing precipitation and temperature data

Oleksandr Lobodzynskyi, Yevheniia Vasylenko, Olha Koshkina, Yurii Nabyvanets

Ukrainian Hydrometeorological Institute, State Emergency Service of Ukraine, National Academy of Sciences of Ukraine

Abstract

It is important to investigate the hydrological consequences of current climate change. Hydrological responses to climate warming and wetter conditions include changes in discharge (frequency, amplitude, and volume). This paper describes current climate change and its impact on hydrological flow within the Horyn River basin. Daily air temperature and precipitation data obtained from the 17 meteorological stations located in and nearby the Horyn River basin, in combination with hydrological data (such as daily water discharges obtained from 9 water gauges), were used for the analysis of climate variability and its hydrological consequences. Analyses of meteorological variables and water discharges are crucial for the assessment of long-term changes in the river regime. Thiessen polygons were used to determine the area of influence of assigned specific meteorological stations, which affect the river's catchments within the Horyn River basin. As a result of the trend analysis, it was observed that discharge within the Horyn River basin decreased over time. These results were congruent with the trends of precipitation data and air temperature data of the stations determined by the Thiessen polygons and basin boundaries. To understand current changes in the daily flow in the basin, changes in air temperature and precipitation for the period 1991-2020 were compared with the period of the climatic norm (1961-1990). A similar analysis was done for daily water discharges. Increasing air temperature and decreasing precipitation in the current period led to a significant decrease in discharges in the Horyn River basin, especially during the spring flood period.

Keywords

Climate change, precipitation, hydrograph, air temperature, Thiessen polygons, Horyn River basin, water discharges.

Submitted 23 January 2023, revised 12 April 2023, accepted 17 April 2023

DOI: 10.26491/mhwm/163286

1. Introduction

Climate change has multiple environmental and economic effects; among them are impacts on water resources and, accordingly, the water supply for drinking and economic needs (agriculture, industries, etc.). By altering major aspects of hydrological regimes, climate change will pose additional challenges to water management. The warming climate is likely to lead to diminished water resources, thus making it difficult to maintain good ecological status in surface waters as prescribed by the Water Framework Directive.

Identifying the variability in water-flow features under current climatic conditions is necessary for (1) solving many scientific and practical issues of rational water resources use; (2) increasing the operational efficiency of water management facilities; and (3) monitoring polluted regions of Ukraine. Therefore, research into the dynamics of river discharges in different regions under the impact of climate change is one of the most urgent tasks for Ukrainian hydrologists.

The first scientific publication to address changes in the hydrological regime of waterbodies under the influence of climate change appeared in the 1980s (Nemec, Schaake 1982; Bultot et al. 1988; Fiering, Rogers 1989; Peterson, Keller 1990). Today, research into climate change impacts on water resources and stream-

flow regimes is the focus of many scientists from various countries around the world. Leaders in the quantity of published scientific works are scientists from the USA and Canada (Schindler 2001; Whitfield 2001; Javelle et al. 2002; Barnett et al. 2004; Diemann, Eltahir 2005; Hodgkins, Dudley 2006; Schnorbus et al. 2022). They have considered the impacts of climate change on water balance characteristics, water resources, and discharge within individual river basins and countries as a whole, including the response of flow fluctuations to climate change scenarios.

This area of research is also well-represented by scientists from Europe, in particular from France (Kastendeuch 2007; Planton, Terrey 2007), Germany (Middelkoop et al. 2001; Menzel et al. 2002), Poland (Kuchar et al. 2014; Malinowski, Skoczko 2018), Hungary (Nováky, Bálint 2011), Czech Republic (Řenzničková et al. 2007), Slovakia (Kohnová et al. 2019), Spain (Brunet et al. 2007), Italy (Confortola et al. 2013), and Scandinavian countries (Rodhe 1981; Krasovskaia, Gottschalk 2002; Andréasson et al. 2004; Phil Graham et al. 2007). Additional leading roles in research of hydrological characteristic changes under the influence of climate fluctuation are played by scientists from China, Japan, India, and other Asian countries (Islam et al. 2005; Devkota, Gyawali 2015; Nazari et al. 2016; Liu, Xu 2017; Dahri et al. 2021; Khatri, Pandey 2021; Al-Munqedhi et al. 2022; Grover et al. 2022; Xiang et al. 2022).

Unfortunately, in contrast to other countries, studies of the current hydrological regimes of rivers in Ukraine under the influence of climate change have not been conducted properly. The studies are pretty much incomplete and unsystematic; in most cases, only general characteristics of changes in selected hydrological parameters have been recorded.

In Ukraine, research into climate change impacts on the hydrological regimes of Ukrainian rivers is conducted by the scientists of National Taras Shevchenko University (Strutynska 2008; Chornomoretz, Hrebin 2010; Hrebin 2010). The probable changes in water resources in Ukraine under global warming conditions have been estimated by scientists of Odesa State Environmental University E. Hopchenko and N. Loboda (Loboda 2005; Hopchenko et al. 2010).

In the present study, the Horyn River basin was selected to represent the current changes in discharge (daily discharges) as well as changes in meteorological factors that influence discharge, such as air temperature and precipitation.

2. The study area

The Horyn River is located in the Pripyat River sub-basin of the Dnipro River Basin District; it is the largest right-bank tributary of the Pripyat River, passing through the territories of Ukraine and Belarus Republic (Fig. 1). The Horyn River is 659 km long, with a drainage basin of 27,791 km². The maximum width is 80 m, and the maximum depth is 16 m. The source of the Horyn River is in the Ternopil Oblast of Ukraine, south of the city of Kremenets, and north of the administrative center of Ternopil Oblast, city of Ternopil. From there, the river flows north in a series of s-shaped bends through the Ukrainian oblasts of Khmelnytskyi and Rivne. Then the river flows northeast into the Belarusian oblast of Brest, where it finally confluences with the Pripyat River.

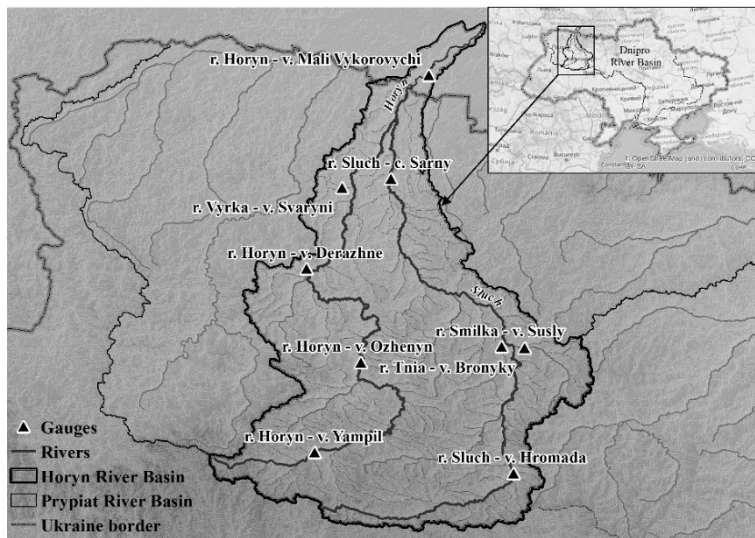


Fig. 1. Location of the Horyn River basin and associated water gauges.

The source of the Horyn River is within the Kremenets Upland: the river flows at first through the Volyn Upland, mostly in a narrow valley with high, steep slopes; later on, the river flows through the Polisia Lowland in an extensive swampy floodplain, marked by channels and old riverbeds. Finally, on the lower section, it passes through the Pinsk swamps.

The main tributaries of the Horyn River are the rivers Sluch (catchment area 13,800 km²), Vilia (catchment area 1,815 km²), Stubla (catchment area 1,350 km²), and Ustyia (catchment area 762 km²).

The river is nourished mainly by snow but with significant percentages of rain and groundwater.

Intra-annual flow is characterized by high spring floods, a summer low-flow period interrupted by short-term rain-induced floods, with rising water levels in autumn and winter.

The upper reaches of the river are used as a source of hydropower and for fishing. In general, the water resources of the basin are used for industrial, household, and agricultural water supply. The Horyn River is regulated by numerous reservoirs and ponds.

The Khmelnytska Nuclear Power Plant (NPP) is located in the upper section of the Horyn River. The NPP utilizes water from the Horyn River for cooling and reduces peak flood values, leaving only minimal runoff in the channel (Pripyat Basin Water Management Authority 2022).

3. Methodology and data

Data from nine water gauges (one of them is in Belarus) with 60 years of observations have been used to study changes in the water regime in the rivers of the Horyn River basin. Also, data from 17 meteorological stations (two in Belarus) has been used to study changes in air temperature and precipitation. The duration of meteorological observations is 60 years.

The location of water gauges and meteorological stations in the Horyn River catchment is shown in Figures 1 and 2.

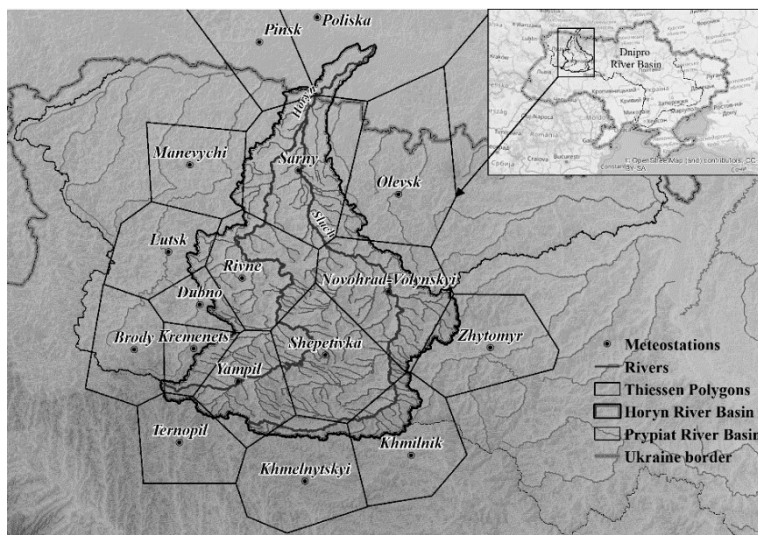


Fig. 2. Thiessen Polygons and location of the meteorological stations.

To analyze the climate change impact on the water regime, influence areas in the river's catchments (i.e., the areas assigned to each specific meteorological station) were delineated within the Horyn River basin, assessed by using ArcGIS.

The first step in analyzing climate change impacts on the water regime is to estimate the meteorological characteristics (precipitation, temperature, etc.) and their distribution within the river's catchments. The network of meteorological stations provides values of climatic characteristics at specific points, so it was necessary to extrapolate the point values of meteorological parameters (daily precipitation and air temperature) over areas within specific catchments. Methods for converting point meteorological values at different meteorological stations into an average value over a catchment include arithmetical means, Thiessen polygons, the Isohyetal method, etc.

The Thiessen polygon method is a commonly used method for weighting observations from meteorological stations according to the area. This method is also called the weighted mean method and is considered the most important in engineering practice. The Thiessen method cannot account for topographical distributions of the parameters, but because the Horyn River basin lacks significant elevation differences, this method can be used.

The Thiessen polygons established the influence areas of specific meteorological stations relative to a separate catchment (Voronoi 1908; Thiessen 1911; Brassel, Reif 1979; Boots 1980, 1986). The weights of the meteorological stations are computed by their relative areas, which are estimated with the Thiessen polygon network. The polygons are formed by the perpendicular bisectors of the lines joining nearby stations. The area of each polygon is used to weigh the meteorological values of the station in the center of the polygon.

According to this method, the weight coefficients (k) are defined in order to obtain average precipitation and air temperature values for the studied catchments attributed to specific water gauges.

ArcGIS tools were used to divide the catchment into separate influence areas (weights) of each meteorological station within the gauged catchments (ArcToolbox > Analysis Tools > Proximity > Create Thiessen Polygons). The influence areas of each meteorological station on the water gauges within the Thiessen polygon were calculated according to the formula:

$$k = f_i/F \quad (1)$$

where, f_i = the influence area of the meteorological station that was calculated within the catchment area of the water gauges; F = the total catchment area of the water gauge.

The sum of the weight coefficients for each water gauge catchment should be equal to 1 (Table 1).

Table 1. The weight coefficients of the meteorological stations for water gauge catchments within the Horyn River basin.

Meteorological stations	Water gauges								
	r. Horyn v. Yampil	r. Horyn v. Ozhenyn	r. Horyn v. Derazhne	r. Horyn v. Mali Vykorovychi	r. Vyrka v. Svaryni	r. Sluch v. Hromada	r. Sluch c. Sarny	r. Tria v. Bronyky	r. Smilka v. Susly
Brody	0.010	0.002	0.001	0.001					
Dubno		0.029	0.054	0.019					
Zhytomyr				0.014			0.027	0.363	
Kremenets	0.254	0.118	0.075	0.026					
Lutsk			0.032	0.011					
Manevychi				0.003	0.028				
Novohrad-Volynskyi				0.176			0.354	0.637	0.533
Olevsk				0.013			0.026		
Rivne		0.055	0.326	0.159			0.026		
Sarny				0.187	0.972		0.130		
Ternopil	0.086	0.021	0.013	0.004					
Khmelnyskyi				0.021		0.230	0.042		
Khmilnik				0.046		0.396	0.092		
Shepetivka		0.296	0.196	0.203		0.239	0.272		0.467
Yampil	0.651	0.480	0.303	0.120		0.135	0.031		
Sum	1	1	1	1	1	1	1	1	1

The next step was to calculate the amount of precipitation and air temperature based on the weighting coefficients for each water gauge catchment within the Horyn River basin, according to the formula:

$$P = P_1 \cdot k_1 + P_2 \cdot k_2 + \dots + P_n \cdot k_n \quad (2)$$

where: $P_1, P_2 \dots P_n$ = the precipitation amount or air temperature at the separate observation points (mm or °C); $k_1, k_2 \dots k_n$ = values of the weighting coefficients at the separate observation point.

To assess the impact of climate change on discharge in the Horyn River basin, the residual mass curves were used to reveal regularities in the cyclical fluctuations of the runoff from the catchment. Correspondingly, with combined chronological graphs, the trend of changes in the long-term dynamics was identified. Trend analysis is one of the most commonly used tools for tracing changes in hydrological time series, such as water discharges, and for meteorological data, such as precipitation and air temperature.

Residual mass curves were used for identifying patterns in the cyclical fluctuations of the hydrometeorological characteristics. For comparing results, the graphs of the long-term dynamics (combined chronological graphs) and the residual mass curves were created in the modulus coefficients (K_i) according to the following equation:

$$K_i = A_i / \bar{A} \quad (3)$$

where: A_i – the value of i -element of the series; \bar{A} – the arithmetical mean of the series (Koshkina, Gorbachova 2013).

To exclude scale effects, the residual mass curves were expressed as normalized deviations for comparison. The expression for the residual mass curves in modular coefficients assumes the following form:

$$\frac{\sum_1^n (K_i - 1)}{C_v} = f(i) \quad (4)$$

where: $f(i)$ – the ordinates for these curves; K_i – the modulus coefficients; C_v – the coefficient of variation.

The coefficient of variation (C_v) is a statistical measure of the dispersion of data points in a data series around the mean. The coefficient of variation represents the ratio of the standard deviation to the mean, and it is a useful statistic for comparing the degree of variation from one data series to another. C_v was calculated according to the following equation:

$$C_v = \sqrt{\frac{(K_i - 1)^2}{n}} \quad (5)$$

where n = the number of members in the series. s

Therefore, the residual mass curve represents the cumulative sum of the modular coefficients' deviations from the mean annual values of the series for each A_i year.

The period for which the integral curve section slopes upward with respect to the horizontal line corresponds to the positive phase (increasing tendency) of fluctuations in the hydrometeorological characteristics. The period for which the integral curve section slopes downward with respect to the horizontal line corresponds to the negative phase (decreasing tendency) (Melnyk, Loboda 2020).

To identify changes in daily water discharges, air temperature, and precipitation in the Horyn River basin caused by climate change, two periods were selected: 1961-1990 and 1991-2020. The period from 1961 to 1990 has been adopted as a standard reference period for long-term climate change assessments, as recommended by WMO (WMO 2017).

4. Results

The residual mass curves and combined chronological graphs of runoff fluctuations at the water gauges of the Horyn River basin for the 1961-2020 period were constructed. The analysis of residual mass curves showed the synchronicity of discharge fluctuations at all water gauges. The low water phase has been observed since the 2000s at all water gauges. The trend line in the combined chronological graphs also indicates a decrease in discharge in the basin in the current period (Fig. 3).

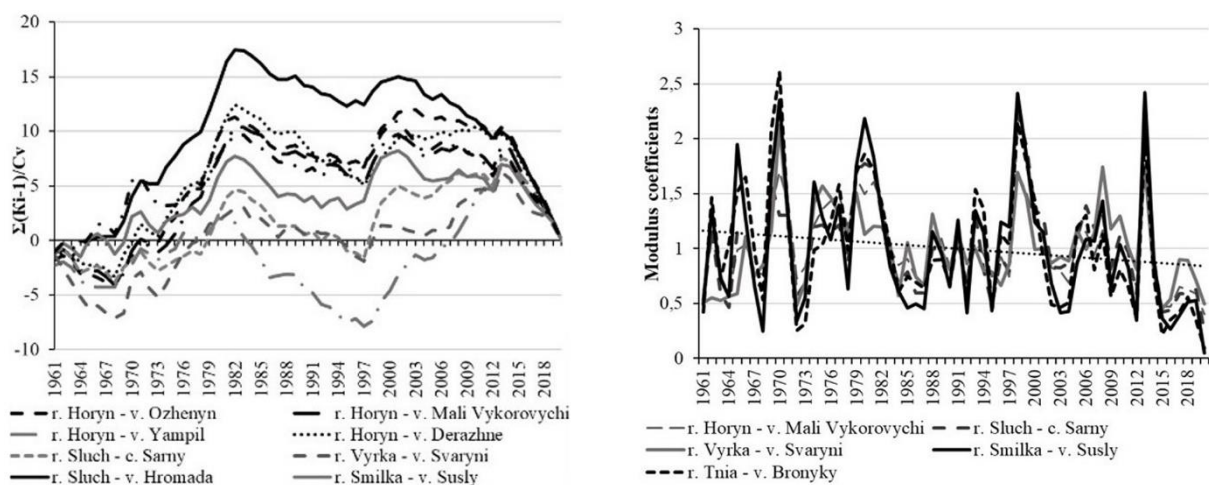


Fig. 3. The residual mass curves and the combined chronological graphs of the mean annual water discharges at water gauges in the Horyn River basin.

The decrease in air temperature can be clearly traced through 1988 according to the residual mass curves of long-term air temperature fluctuations; the current warming period is apparent, beginning in 1998.

The averaged combined chronological graph of air temperature fluctuations is characterized by an upward trend in the Horyn River basin (Fig. 4).

The analysis of long-term fluctuations of the annual precipitation showed that they are synchronous. Thus, there was an increase in precipitation before the 1980s, but precipitation has been decreasing since 2013 within the basin. Short-term phases of decrease or increase of precipitation with small-amplitude fluctuations have been observed in the Horyn River basin during the period of the 1980s-2000s. This conclusion is proved by the pattern in precipitation absolute values on the averaged combined chronological graph (Fig. 5).

The complex residual mass curves were developed to show the dependence of discharge changes (mean annual water discharges) on meteorological factors (mean annual air temperature and annual precipitation) (Fig. 6). The graphs clearly show the synphase discharge and precipitation fluctuations, as well as their

asynphase to fluctuations of the air temperature. Such trends were observed in all water gauges within the Horyn River basin.

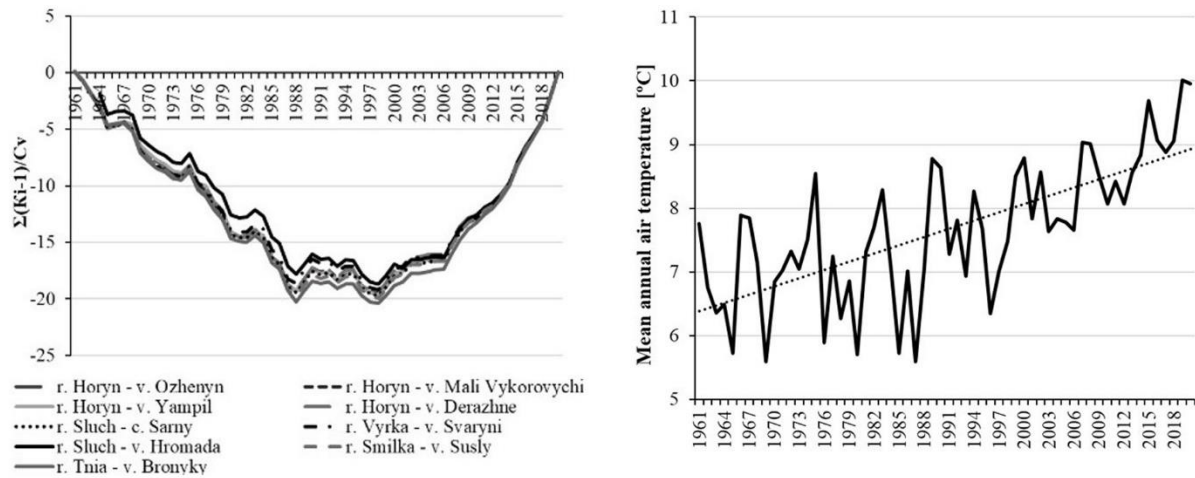


Fig. 4. The residual mass curves and the combined chronological graphs of the mean annual air temperature at water gauges in the Horyn River basin.

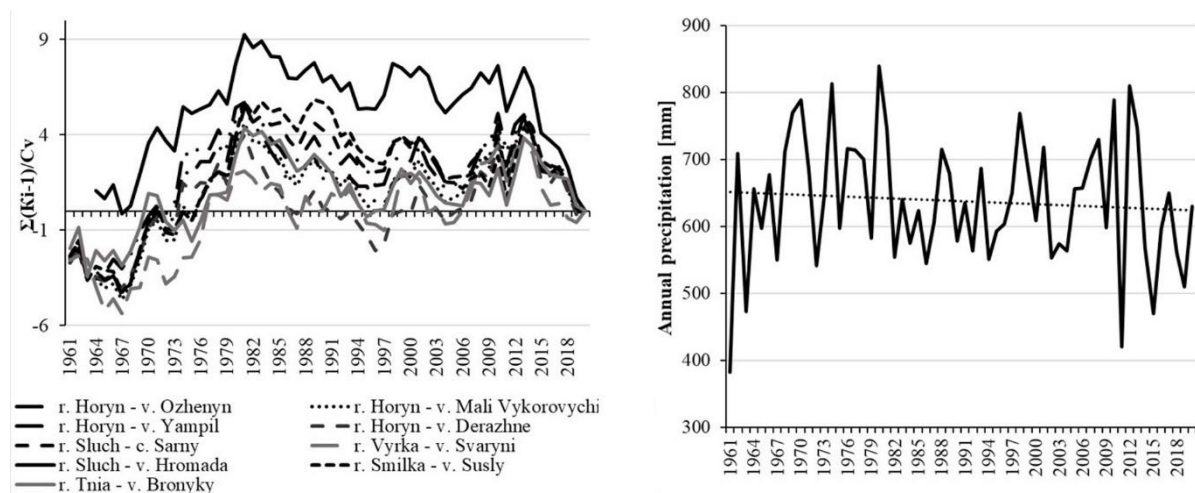


Fig. 5. The residual mass curves and combined chronological graphs of the annual precipitation at water gauges in the Horyn River basin.

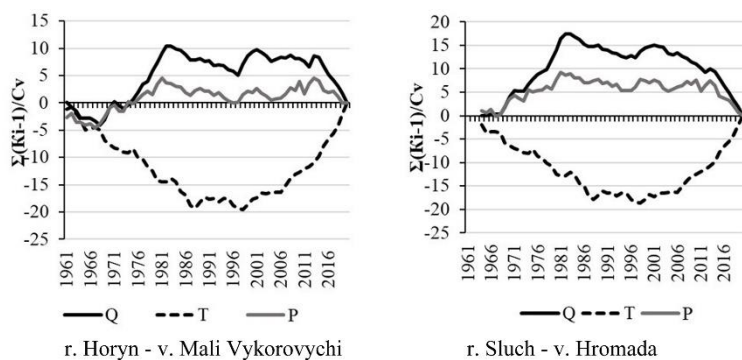


Fig. 6. The combined residual mass curves of the mean annual water discharges (Q), the mean annual air temperature (T), and the annual precipitation (P) at water gauges in the Horyn River basin.

Combined graphs of the long-term mean monthly air temperature and precipitation and averaged hydrographs of the mean daily water discharges for two periods for all nine water gauges in the Horyn River basin were plotted to determine the changes in the discharge in the current period (1991-2020) in comparison with the period of the climatic norm (1961-1990) using precipitation and temperature analysis (Fig. 7).

Discharge

The analysis of discharge hydrographs for the periods 1961-1990 and 1991-2020 showed that flows have significantly decreased in the current period in the Horyn River basin (Fig. 7). Such changes are especially observed in the spring period, when the shape of the discharge hydrographs changed toward a flatter profile, without such high peak water discharges as in the period of the climatic norm. Thus, water discharges in the Horyn River basin decreased on average by 21% in spring, 15% in summer, and 13% in autumn. The most significant decrease in discharge compared to the period of climatic norm was observed in April, when it decreased on average by 30% within the basin. March and May are characterized by an average decrease in water discharges of 14%. The largest decrease in water content in the summer period occurred in July (by 22%). As for the autumn season, the largest decrease in water runoff (by 17%) in the Horyn River basin was observed in September and the least (by 8%) in October. In contrast to other seasons, water discharges in the winter period increased by an average of 8% within the basin. However, such changes are not observed throughout the season. Thus, the water discharges decreased by 12% in December, whereas the discharge in January and February increased by 10% and 24% compared to the period of the climatic norm (Fig. 7).

Precipitation

A decrease of precipitation by 8-9% was noted in winter, spring, and summer from 1991 to 2020 in the Horyn River basin (Fig. 7). Thus, precipitation in the winter period mostly decreased in January (by 14%), and the least in February (by 5%). Spring precipitation decreased by 27% on average in April in the Horyn River basin and increased by 11% in March. In summer, there is also less precipitation in the basin compared to the climatic norm. The largest changes were in June, when precipitation in the current period decreased by 12%, and the smallest changes were observed in July (by 6%). Precipitation increased in autumn by 4% compared to the climatic norm. For the autumn months, the greatest increase in precipitation was in October (by 6%), while the smallest was in September (by 2%).

Air temperature

Air temperature has been increasing throughout the year during the current period, ranging from 0.6°C (autumn) to 1.6°C (winter). For the study area, January has experienced the greatest warming in the current period (by 2.3°C), while October has warmed the least (by 0.5°C). The greatest temperature increase in spring and summer (by 1.8°C) was observed in March and July (Fig. 7).

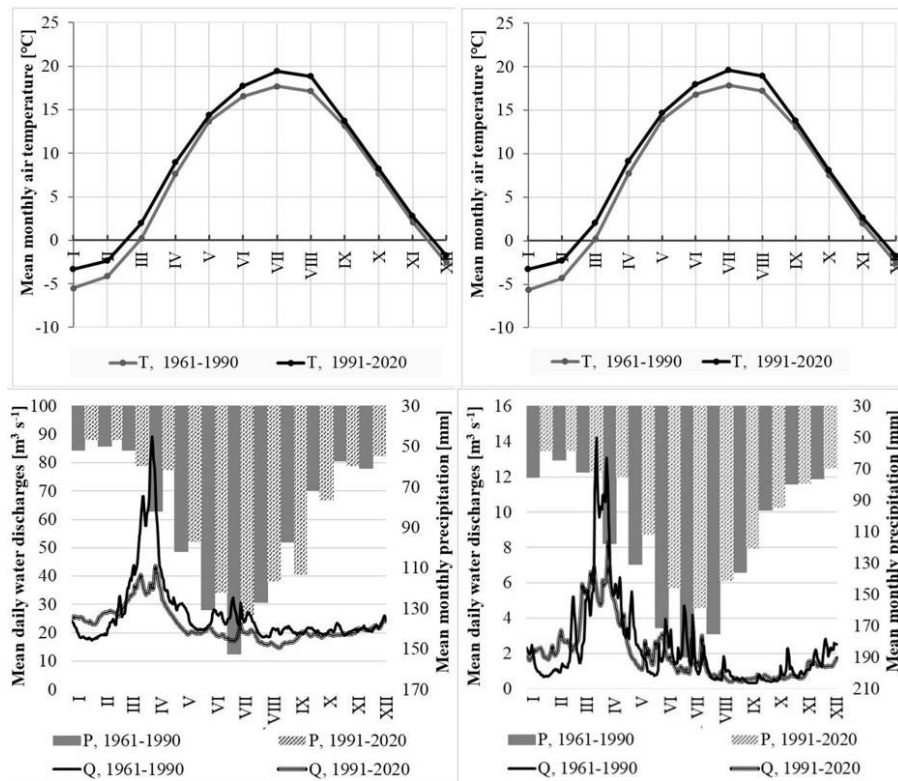


Fig. 7. Combined graphs of long-term mean monthly air temperature (T) and precipitation (P) and mean annual daily discharge (Q) hydrographs for two periods (1961-1990 and 1991-2020) at water gauges in the Horyn River basin.

In summary, within the Horyn River basin, the discharge decreased by 13%; the precipitation by 6%; and the annual average air temperature increased by 1.3°C in comparison with the WMO climatic norm (1961-1990).

The analysis of combined graphs of air temperature and precipitation and discharge hydrographs in rivers of the Horyn River basin has shown that the water discharges of spring floods significantly decreased with the simultaneous increase of water discharges in the winter low-water period over the past thirty years. We assume that such a decrease in the spring flood in the Horyn River basin could be explained by the increasing air temperature throughout the basin, especially during the winter period. This led to decreases in the soil freezing depth, causing, in combination with frequent thaws in winter, decreases in water equivalents of the snow cover. Our findings are supported by other studies (Hrebin, Vasylenko 2012).

Despite the precipitation increases in the autumn period, the decrease of discharge in this period probably can be explained by the air temperature increasing, which leads to increased evaporation from the water surface and increased infiltration processes in autumn.

The discharge decrease in summer, as observed in the current period (1991-2020) in the Horyn River basin, is attributable to increasing air temperature and a decrease in the precipitation that forms rain floods in this period.

5. Conclusion

The analysis of daily air temperature and precipitation reflects the negative impact of climate change on the discharge in the Horyn River basin over the past 30 years. Thus, since the 2000s, there has been a transition from the high- to low-water phase of the hydrological cycle for all rivers of the basin, which continues to the present.

Since the end of the 1990s, the air temperature increase was noted at all water gauges of the Horyn River basin. Since the 2010s, there has been a clear decrease in precipitation in the basin.

Despite the fact that over the past 30 years, precipitation has increased in March, the flow of the spring period has decreased by almost half. This phenomenon can be attributed to increasing air temperature in the winter period, frequent thaws, and, consequently, to the decrease in the water equivalent of snow cover, which plays a major role in nourishment of the rivers of the basin and forms the greater part of the annual runoff during the spring flood period. On the other hand, these factors have led to increasing discharge during the winter low-water period.

The influence of climatic factors on the water runoff of the summer and autumn periods also caused decreased water storage during these seasons in the current period.

These findings should be useful for the rational management and appropriate use of water resources under climate change conditions in the Horyn River basin, as well as for updating the regulations of the Khmelnytska NPP exploitation, which is located within the studied basin. The approaches used in this paper can be applied to the study of other river basins with similar conditions of flow formation.

References

- Al-Munqedhi B.M., El-Sheikh M.A., Alfarhan A.H., Alkahtani A.M., Arif I.A., Rajagopal R., Alharth S.T., 2022, Climate change and hydrological regime in arid lands: Impacts of dams on the plant diversity, vegetation structure and soil in Saudi Arabia, *Saudi Journal of Biological Sciences*, 29 (5), 3194-3206, DOI: 10.1016/j.sjbs.2022.01.043.
- Andréasson J., Bergström S., Carlsson B., Phil Graham L., Lindström G., 2004, Hydrological change – climate change: impact simulations for Sweden, *AMBIO: A Journal of the Human Environment*, 33 (4), 228-234, DOI: 10.1579/0044-7447-33.4.228.
- Barnett T., Malone R., Pennell W., 2004, The effects of climate change on water resources in the west: introduction and overview, *Climate Change*, 62 (1-3), 1-11.
- Boots B.N., 1980, Weighting Thiessen polygons, *Economic Geography*, 56 (3), 248-259, DOI: 10.2307/142716.
- Boots B.N., 1986, Voronoi (Thiessen) Polygons, *Geo Books*, Norwich, UK, 51 pp.
- Brassel K.E., Reif D., 1979, A procedure to generate Thiessen polygons, *Geographical Analysis*, 11 (3), 289-303, DOI: 10.1111/j.1538-4632.1979.tb00695.x.
- Brunet M., Jones P., Sigro J., Saladie O., Aguilar E., Moberg A., Della-Marta P.M., Lister D., Walther A., Lopez D., 2007, Temporal and spatial temperature variability and change over Spain during 1850-2005, *Journal of Geophysical Research: Atmospheres*, 112 (D12), DOI: 10.1029/2006JD008249.
- Bultot F., Coppens A., Dupriez A., Gellens D., Meulenberghs F., 1988, Repercussions of a CO₂ doubling on the water cycle and on the water balance. A case study for Belgium, *Journal of Hydrology*, 99 (3-4), 45-56, DOI: 10.1016/0022-1694(88)90057-1.

- Chornomoretz Yu.O., Hrebin V.V., 2010, Intra yearly distribution of individual elements of the water balance of the Desna River Basin (within Ukraine and their long-term fluctuations), *Hydrology, Hydrochemistry and Hydroecology*, 18, 98-106, (in Ukrainian).
- Confortola G., Soncini A., Bocchiola D., 2013, Climate change will affect hydrological regimes in the Alps. A case study in Italy, *Journal of Alpine Research*, 101-3, DOI: 10.4000/rga.2176.
- Dahri Z.H., Ludwig F., Moors E., Ahmad S., Ahmad B., Ahmad S., Riaz M., Kabat P., 2021, Climate change and hydrological regime of the high-altitude Indus basin under extreme climate scenarios, *Science of the Total Environment*, 768, DOI: 10.1016/j.scitotenv.2020.144467.
- Devkota L.P., Gyawali D.R., 2015, Impacts of climate change on hydrological regime and water resources management of the Koshi River Basin, Nepal, *Journal of Hydrology: Regional Studies*, 4, 502-515, DOI: 10.1016/j.ejrh.2015.06.023.
- Diemann J., Eltahir E., 2005, Sensitivity of regional hydrology to climate changes, with application to the Illinois River basin, *Water Resources Research*, 41 (7), DOI: 10.1029/2004WR003893.
- Fiering M., Rogers P., 1989, *Climate change and water resources planning under uncertainty*, U.S. Army Engineer Institute for Water Resources, Fort Belvoir, VA.
- Grover S., Tayal S., Sharma R., Beldring S., 2022, Effect of changes in climate variables on hydrological regime of Chenab basin, western Himalaya, *Journal of Water and Climate Change*, 13 (1), 357-371, DOI: 10.2166/wcc.2021.003.
- Hodgkins G.A., Dudley R.W., 2006, Changes in the timing of winter-spring stream flows in eastern North America, 1913-2002, *Geophysical Research Letters*, 33 (6), DOI 10.1029/2005GL025593.
- Hopchenko E.D., Ovcharuk V.A., Shakirzanova J.R., 2010, The researches of the influence of modern climate changes on the characteristics of maximum spring flood runoff in the Prypiat River Basin, *Hydrology, Hydrochemistry and Hydroecology*, 3 (20), 50-59, (in Ukrainian).
- Hrebin V.V., 2010, *The modern water regime of rivers in Ukraine (landscape- hydrologic analysis)*, Kyiv: Nika-Centr, 316 pp., (in Ukrainian).
- Hrebin V.V., Vasylenko E.V., 2012, The analysis of current changes of the spring flood forming factors on the rivers in the Prypiat river basin (within Ukraine), *Physical Geography and Geomorphology*, 2 (66), 161-167.
- Islam M.S., Aramaki T., Hanaki K., 2005, Development and application of an integrated water balance model to study the sensitivity of the Tokyo metropolitan area water availability scenario to climatic changes, *Water Resources Management*, 19 (4), 423-445, DOI: 10.1007/s11269-005-3277-1.
- Javelle P., Taha Ouarda B.M.J., Bobée B., 2002, Spring flood analysis using the flood-duration-frequency approach: application to the provinces of Quebec and Ontario, Canada, *Hydrological Processes*, 17 (18), 3717-3736, DOI: 10.1002/hyp.1349.
- Kastendeuch P., 2007, Pressure gradient force, atmospheric circulation and climate in Western Europe (1899-2002), *International Journal of Climatology*, 27 (15), 2055-2067, DOI: 10.1002/joc.1504.
- Khatri D., Pandey V.P., 2021, Climate Change Impact on the Hydrological Characteristics of Tamor River Basin in Nepal Based on CMIP6 Models, [in:] *Proceedings of 10th IOE Graduate Conference*, 10, 532-539.
- Kohnová S., Rončák P., Hlavčová K., Szolgay J., Rutkowska A., 2019, Future impacts of land use and climate change on extreme runoff values in selected catchments of Slovakia, *Meteorology, Hydrology and Water Management*, 7 (1), 47-55, DOI: 10.26491/mhwm/97254.
- Koshkina O.V., Gorbachova L.O., 2013, Hydro-genetic research method of the main factors of the spring flood in the Desna River Basin, [in:] *11th Annual International Conference of Young Scientists on Energy Issues*, Cyseni, Kaunas, Lithuanian Energy Institute, IX618-IX631.
- Krasovskaia I., Gottschalk L., 2002, River flow regimes in a changing climate, *Hydrological Sciences Journal*, 47 (4), 597-609, DOI: 10.1080/02626660209492962.
- Kuchar L., Szalińska W., Iwański S., Jelonek L., 2014, A modeling framework to assess the impact of climate change on river runoff, *Meteorology, Hydrology and Water Management*, 2 (2), 49-63, DOI: 10.26491/mhwm/36671.

- Liu L., Xu Z.X., 2017, Hydrological implications of climate change on river basin water cycle: case studies of the Yangtze River and Yellow River basins, China, *Applied Ecology and Environmental Research*, 15 (4), 683-704, DOI: 10.15666/aeer/1504_683704.
- Loboda N.S., 2005, Calculations and generalization of the annual runoff characteristics of the rivers in Ukraine in the conditions of anthropogenic influence, Odessa: Ekologia, 208 pp., (in Russian).
- Malinowski L., Skoczko I., 2018, Impacts of climate change on hydrological regime and water resources management of the Narew River in Poland, *Journal of Ecological Engineering*, 19 (4), 167-175, DOI: 10.12911/22998993/91672.
- Melnyk S., Loboda N., 2020, Trends in monthly, seasonal, and annual fluctuations in flood peaks for the upper Dniester River, *Meteorology, Hydrology and Water Management*, 8 (2), 28-36, DOI: 10.26491/mhwm/126705.
- Menzel L., Niehoff D., Bürger G., Bronstert A., 2002, Climate change impacts on river flooding: A modelling study of three meso-scale catchments, *Climatic Change: Implications for the Hydrological Cycle and for Water Management*, 10, 249-269, DOI: 10.1007/0-306-47983-4_14.
- Middelkoop H., Daamen K., Gellens D., Grabs W., Kwadijk J.C.J., Lang H., Parmet B.W.A.H., Schädler B., Schulla J., Wilke K., 2001, Impact of climate change on hydrological regimes and water resources management in the Rhine basin, *Climatic Change*, 49, 105-128, DOI: 10.1023/A:1010784727448.
- Nazari P., Kardavany H., Farajirad P., Abdolreza A., 2016, Assessment of runoff changes under climate change scenarios in the dam basin of Ekbatan, Hamedan Iran, *Journal of Climatology and Weather Forecasting*, 4, DOI: 10.4172/2332-2594.1000172.
- Nemec I., Schaake I., 1982, Sensitivity of water resources systems to climate variation, *Hydrological Sciences Journal*, 27 (3), 46-52, DOI: 10.1080/02626668209491113.
- Nováky B., Bálint G., 2013, Shifts and modification of the hydrological regime under climate change in Hungary, [in:] *Climate Change*, B.R. Singh (ed), IntechOpen, DOI: 10.5772/54768.
- Peterson D., Keller A., 1990, Irrigation, [in:] *Climate Change and US Water Resources*, John Wiley, New York, 269-306.
- Phil Graham L., Hagemann S., Jaun S., Beniston M., 2007, On interpreting hydrological change from regional climate models, *Climate Change*, 81, 97-122, DOI: 10.1007/s10584-006-9217-0.
- Planton S., Terray L., 2007, Detection et attribution à l'échelle régionale: Le cas la France, *La Météorologie*, 58, 25-29, DOI: 10.4267/2042/18205.
- Pripyat Basin Water Management Authority, 2022, Water Resources, available online at https://buvrzt.gov.ua/vodni_resyrsy.html (data access 18.04.2023).
- Řenzničková L., Brázdil R., Tolasz R., 2007, Meteorological singularities in the Czech Republic in the period 1961-2002, *Theoretical and Applied Climatology*, 88 (3-4), 179-192, DOI: 10.1007/s00704-006-0253-5.
- Rodhe A., 1981, Spring flood: meltwater or groundwater? *Nordic Hydrology*, 12, 21-30.
- Schindler D., 2001, The cumulative effects of climate warming and other human stresses on Canadian freshwaters in the new millennium, *Canadian Journal of Fisheries and Aquatic Sciences*, 58 (1), 18-29, DOI: 10.1007/978-1-4615-1493-0_11.
- Schnorbus M., Werner A., Bennett K., 2022, Impacts of climate change in three hydrologic regimes in British Columbia, Canada, *Hydrological Processes*, 28 (3), 1170-1189. DOI: 10.1002/hyp.9661.
- Strutynska V.M., 2008, Dynamics of the ice regime characteristics in rivers of the Dnipro River Basin on the background of modern climate changes, *Hydrology, Hydrochemistry and Hydroecology*, 14, 116-122, (in Ukrainian).
- Thiessen A.H., 1911, Precipitation averages for large areas, *Monthly Weather Review*, 39 (7), 1082-1084, DOI: 10.1175/1520-0493(1911)39<1082b:PAFLA>2.0.CO;2.
- Voronoi G., 1908, Nouvelles applications des parametres continus a la theorie des formes quadratiques, deuxieme memoire, recherches sur les paralleloedres primitifs, *Journal fur die Reine and Angewandte Mathematik*, 134, 198-287, DOI: 10.1515/crll.1908.134.198.
- Whitfield P., 2001, Linked hydrologic and climate variations in British Columbia and Yukon, *Environmental Monitoring and Assessment*, 67 (1-2), 217-238, DOI: 10.1023/A:1006438723879.

WMO, 2017, Guidelines on the Calculation of Climate Normals, WMO-No. 1203, World Meteorological Organization, Geneva, Switzerland.

Xiang Y., Wang Y., Chen Y., Zhang Q., 2022, Impact of climate change on the hydrological regime of the Yarkant River Basin, China: An assessment using three SSP scenarios of CMIP6 GCMs, *Remote Sensing*, 14 (115), DOI: 10.3390/rs14010115.

Non-homogeneity of hydrometric data and estimating the rating curve

Teresa Jakubczyk , Wiesław Szulczewski

Wrocław University of Environmental and Life Sciences

Abstract

One of the main tasks of contemporary hydrology is to plot the best possible rating curve, which has numerous applications in practical hydrological problems. The quality of the curve depends to a significant degree on the precision of hydrometric measurements and the precision in determining the relationship between discharge and the stage (water level). In this study, we engage the multidimensional problem of non-homogeneity of hydrometric data. The distances between a given point of measurement and the given cross-section proved to be highly diverse. Hence, we propose data transformation so that every measurement can be treated as taken in a given cross-section. The transformation allows partial homogenization of measurement data. An automatic non-linear method for estimating the rating curve is also proposed. The method has been tested on selected representatives of mountain, submontane, and lowland rivers of the Oder River catchment basin (Lower Silesia, Poland). Cross-sections selected for analysis were: Łąki on the Barycz River, Łądek Zdrój on the Biała Łądecka River, Jelenia Góra on the Bóbr River, Jakuszyce on the Kamienna River, and Łozy on the Kwisa River.

Keywords

Rating curve, non-homogeneity of data sets, hydrometric measurements, hydrology, measurements, and data.

Submitted 15 November 2022, revised 31 March 2023, accepted 16 June 2023

DOI: 10.26491/mhwm/168142

1. Introduction

Estimating the most precise possible rating curve is one of the main and most difficult tasks facing contemporary hydrology. The problem is of fundamental importance for the prediction of flood events, rational use of water resources, the design of hydro-technical structures, where extreme flow rates are accepted as the design standard (Ozga-Zieliński et al. 2014), and the determination of flood-threatened zones based on maximum flows and the corresponding stages (Radczuk et al. 2001). The rating curve is also the basis for the determination of hydrological criteria (Egelson 1978), i.e., seasonal average and extreme flows and time series for estimating the response of the catchment basin at high and low water

stages. A correctly plotted rating curve can also be a reference for estimating maximum annual flows (Szulczewski et al. 2018).

The problem of precise estimating of the rating curve has been addressed previously in numerous publications and monographs. The uncertainty of rating curves arises from two sources (Westerberg, McMillan 2015). First are the hydrometric measurements from which the curve is plotted. The accuracy of measurements is extremely important for estimating a good rating curve, and errors in river flow data are far from negligible (Di Baldassarre, Montanari 2009). The second source, usually more important, is precision in the determination of the relationship between the discharge and the stage. Errors resulting from both of those sources have been analyzed with various methods in numerous studies. Lang et al. (2010) propose the use of Bayesian methods in combination with the Markov Chain Monte Carlo (MCMC) process for analyzing the problem. In that study, as background for advanced analysis, historical measurements were analyzed to identify errors resulting from inaccurate measurements and changes in the cross-section of channels. The advanced analyses were conducted on a suitably reduced data set. We can, therefore, consider partial homogenization of the analyzed data. Conclusions following the study by Lang et al. (2010) indicate that a lack of analysis of errors in rating curves can result in inaccuracies in the estimation of curves. The extrapolation itself is already burdened with inaccuracy. Reitan and Petersen-Overleir (2009), using similar methods, propose the estimation of a segment curve which provides better accuracy for those flow regimes at which measurements are seldom taken.

Interpreting the rating curve, especially in the case of estimating flood risk, should account for potential errors of estimation (Singh, Strupczewski 2002; Haque et al. 2014).

The goodness of fit of rating curves can be tested with a variety of indicators. A comparison of eleven such indicators is presented in the paper by Krause et al. (2005). The authors demonstrate that the most frequently applied indicators of fit may not give the best results, and even high values do not necessarily mean a good-fitting curve.

The rating curve is a non-linear function $H = f(Q)$ describing the relation between the stage H and the discharge Q . It is plotted based on hydrometric measurements, which, due to their level of precision, can be one of the sources of its uncertainty (Domeneghetti et al. 2012). The curve can be plotted and

described with the use of various formulae and methods. Frequently applied formulae include, e.g., the Chezy and Manning formulae, which relate the mean water flow rate in a profile with tangent stress in a wetted perimeter (Strupczewski 1996; Fenton, Keller 2001). Those formulae work well in the case of monotonic flow in an open channel. A study by Leonard et al. (2000) indicates that such an approach can be successfully applied in the case of rivers with variable sections. Direct application of the Chezy and Manning formulae, however, can be tedious due to the number of parameters. In addition, some of the variables are determined separately for channel water and flood areas, and others in a descriptive manner (Szkutnicki et al. 2007). Incorrect interpretation of any of the parameters results in an erroneous evaluation of the flow value.

A more universal formula is the Harlacher formula (Byczkowski 1999) which relates the stage of water directly with the volume of flow at the given cross-section. In addition, the Harlacher formula describes the opposite relationship, $Q = f(H)$, which simplifies calculations and the interpretation of results. This formula is expressed as:

$$Q = \alpha (H - B)^n$$

where α and n are parameters, and B is the state of zero flow (Szkutnicki et al. 2007). The constant B can be determined from the cross-section of the bottom or the longitudinal profile of the watercourse, or with graphical and graphical analytical methods (Dębski (1955); Byczkowski (1999)). In practice, however, it is most often assumed that $B = 0$. With that assumption, the rating curve equation has the following form:

$$Q = aH^b \tag{1}$$

where a and b are parameters. The literature (Dębski 1955; Szkutnicki et al. 2007) proposes the determination of parameters a and b through the linearization of Eq. 1 by using a logarithmic model. A rating curve based directly on parameters determined in this manner is easy to interpret, and its shape is uniquely described by the shape of the channel profile (Ozga-Zieliński et al. 2014). The logarithmic curve, however, does not provide the required accuracy because of widely scattered data. A comparison of the logarithmic method of rating curve determination with historical methods based on fitting quadratic and cubic polynomials to the data is presented by Sivapragasam and Muttil (2005). Their study indicates that

the results obtained with conventional methods can be improved by means of the alternative approaches to the problem that they propose. Sivapragasam and Muttill (2005) determined the stage-discharge relationship using the SVM (Support Vector Machine) and ANN (Artificial Neural Network) methods. Those methods, however, given their complexity, are still difficult to apply in operational use. Another alternative method for estimating the rating curve is proposed by Dottori et al. (2009). It is based on a parabolic differential equation relating the lowering of the water level in the channel to local and convective acceleration in the stream. The proposed method gives very good results and allows the extrapolation of the curve in cases when there is a lack of measurements in the high discharge zone.

All of the studies mentioned above were conducted on hydrometric data collected during multi-year measurement series. In most cases, there is no information as to whether the data had been transformed in any way before the analyses. One can assume, therefore, that they did not constitute homogeneous sets. Non-homogeneity of measurement data can have numerous causes. It can result from a change of the measurement site, as in the case described above, but also, e.g., from a change in the method of data acquisition, movement of the water gauge to another location, change of ordinate "0" of the water gauge, or from other anthropogenic and natural factors (Ozga-Zielińska, Brzeziński 1994). The problem of non-homogeneity was also noted by Szulczewski and Jakubowski (2018). Those authors indicate that a more accurate analysis of data sets can be performed by assuming a priori their non-homogeneity and applying a mix of two different probability distributions for their description.

The objective of this paper is to propose a method for homogenizing a set of hydrometric measurements based on the location of measurements.

2. Data and methods

The analyses were conducted on measurement data provided by the Institute of Meteorology and Water Management, State Research Institute. The hydrometric data obtained related to rivers and cross-sections that were selected as representative of mountain, submontane, and lowland rivers. Table 1 is a compilation of information on the selected cross-sections. The selected stations are marked in Figure 1. The hydrometric measurements included such features of the watercourse as the water stage H [cm], discharge Q [m³/s], average and maximum velocity V_{avg} and V_{max} [m/s], area of wetted cross-section F [m²]. The

discharge is calculated from the measured average flow rate. The data tables also include information on the distance from the water gauge [m] and the direction relative to it from which the measurement was taken.

Table 1. Selected representatives of river types. H = water stage, Q = discharge, F = area of wetted cross-section, V_{avg} = average flow velocity, V_{max} = maximum flow velocity.

	1	2	3	4	5
river	Barycz	Biała Łądecka	Bóbr	Kamienna	Kwisa
cross-section	Łąki	Łądek Zdrój	Jelenia Góra	Jakuszyce	Łozy
river type	lowland	mountain	submontane	mountain	submontane
measurement period	1969-2013	1952-2016	1948-2016	1972-2016	1954-2017
interval H [cm]	70-493	20-178	70-303	14-84	102-554
interval Q [m ³ s ⁻¹]	0.25-121.23	0.575-58.5	1.93-236.2	0.03-4.34	1.12-193
interval F [m ²]	0.67-158.2	1.78-29.2	6.2-90.61	0.23-706	5.37-184.2
interval V_{avg} [ms ⁻¹]	0.19-0.77	0.142-2.055	0.11-2.23	0.09-1.52	0.12-1.55
interval V_{max} [ms ⁻¹]	0.26-1.34	0.312-3.154	0.19-7.7	0.1-2.47	0.29-3.51
interval distance from the water gauge (m)	0-120	0-1000	0-5000	0-100	0-700

Based on data from the individual water gauge profiles, rating curves were plotted per Eq. 1. Parameters a and b were calculated with a non-linear regression model. The goodness of fit of the curves to the data sets was described with the Nash-Sutcliffe index:

$$NSE = 1 - \frac{\sum_{n=1}^N (Q_m^n - Q_o^n)^2}{\sum_{n=1}^N (Q_m^n - \overline{Q_o})^2}$$

where Q_m means the theoretical value of discharge volume calculated from Eq. 1, Q_o is a value observed in measurements, and $\overline{Q_o}$ is the mean value from the measurements. The value $NSE = 1$ indicates ideal fitting of the curve to the hydrometric data. An NSE value below zero indicates that the mean value of the observed time series would have been a better predictor than the model (Krause et al. 2005).

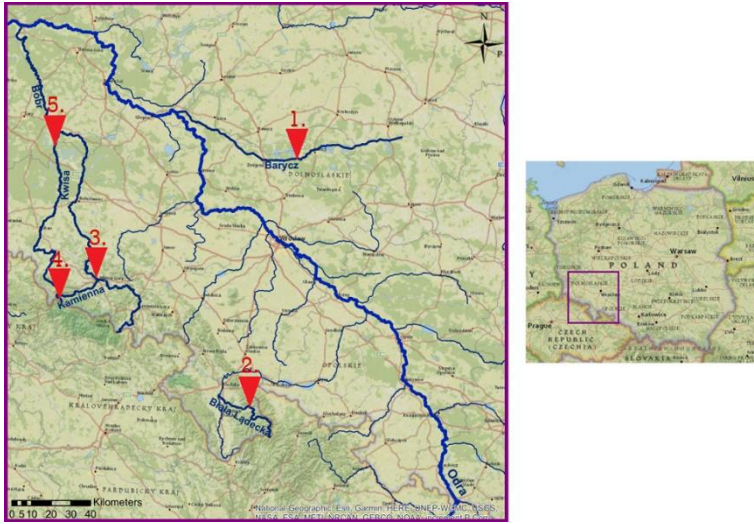


Fig. 1. The region analyzed shown on the map of Poland. Locations of cross-sections selected for analysis: 1 – Barycz, Łąki; 2 – Biała Łądecka, Łądek Zdrój; 3 – Bóbr, Jelenia Góra; 4 – Kamienna, Jakuszyce; 5 – Kwisa, Łozy. Source: National Geographic ESRI Garmin Map.

Referring to the study by Krause et al. (2005), the index NSE was compared with two other measures of the goodness of fit. One of them, proposed by the authors of the cited study, is the modified form of that index, called the relative index NSE_{rel} . It is characterized as follows:

$$NSE = 1 - \frac{\sum_{n=1}^N \left(\frac{Q_m^n - Q_o^n}{Q_o^n} \right)^2}{\sum_{n=1}^N \left(\frac{Q_m^n - Q_o^n}{Q_o} \right)^2}$$

where the symbols and the interpretation of the resulting value are the same as in the case of the classic NSE . The other measure is the relative mean error of fit η_{rel} , defined as:

$$\eta_{rel} = \frac{1}{N} \sum_{n=1}^N \frac{|Q_m^n - Q_o^n|}{Q_o^n}$$

Low values of coefficient η_{rel} indicate a good fit of the rating curve to the data set.

Significant sources of non-homogeneity of data sets include, e.g., the place where the measurement was taken and the method with which it was made (Bartnik, Jokiel 1997). The literature provides numerous comparisons of methods of measurement with the use of the current meter and, acoustic Doppler current profiler (ADCP; Delcroix et al. 1992; Hayes et al. 2012; Chauhan et al. 2014), and detailed descriptions of those methods (Gore, Banning 2017), but there is no model that would permit homogenizing data in relation to the method of measurement. Figure 2 presents hydrometric data limited to measurements taken at medium and low stages at selected cross-sections, with the method of measurement indicated. In a majority of cases, except for the measurements taken on the Barycz River (a lowland river), one can observe a distinction between the appearance of the two groups related to the method with which the measurements were taken. Due to the substantial non-homogeneity of the data resulting from the methods of measurement, we decided to use only the results from current meter measurements for this study. Data acquired with the current meter method are abundantly represented at each of the given cross-sections. In addition, at high stages on the mountain rivers, the measurements are taken with that method only, therefore, the acquired information is used for the approximation of the rating curve describing high water stages. For this study, we also decided to use all of the measurements (both historical and the latest) to increase the number of observations. The method was conducted on other, smaller data sets from short periods of time to satisfy the assumption that the river shape was constant, as it would not be over long periods of time (Domeneghetti et al. 2012). The distances between a given point of measurement and the given cross-section proved to be highly diverse. Approximately 50% of the measurements were taken exactly in the given cross-section, but the other measurements were taken at a smaller or larger distance (from several to several hundred meters) from the given cross-section, both upstream and downstream. This variation in distances of hydrometric measurements from the given cross-sections motivated the construction of a transformation allowing partial homogenization of measurement data. The transformation was based on the assumption of constant discharge in time at a given measurement, irrespective of the point at which it was taken. When the velocities are measured away from the given cross-section, and the discharge is calculated based on their values, the stage values are taken from the water gauge profile. Upon application of the transformation, stages that would appear on the cross-section at such discharges were assigned to the discharges from measurements taken away from the given cross-section. Since the discharge is constant, for the transformation, the changes in the river geometry were left

out. The first step of the transformation was the estimation of the rating curve for the data acquired in the given cross-section, $O_0 = a_0 H_0^{b_0}$. That relation was treated as the reference. Its parameters a_0 and b_0 were used for correct transformation of measurements taken outside of the given cross-section.

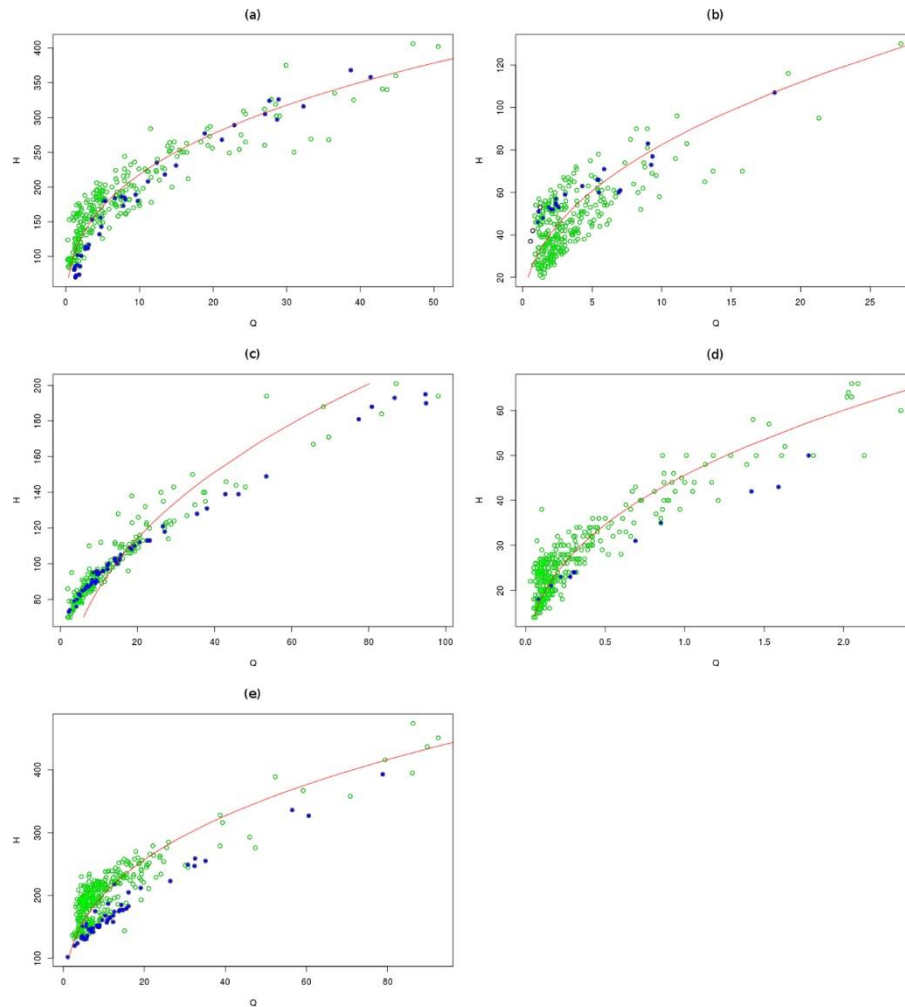


Fig. 2. Hydrometric data for medium and low stages from selected cross-sections. Green: data acquired by current meter; blue: data acquired by ADCP; open dots: data acquired with other methods; (a) Barycz, Łąki; (b) Biała Łądecka, Łądek Zdrój; (c) Bobr, Jelenia Góra; (d) Kamienna, Jakuszyce; (e) Kwisa, Łozy.

The data corresponding to the measurements taken outside of the given cross-section were divided into two groups, one acquired downstream and the other upstream from the cross-section. The rating curve $Q_1 = a_1 H_1^{b_1}$ was estimated for each group separately. Based on the assumption of constant discharge Q , we obtain:

$$H_1 = \left(\frac{a_0}{a_1} H_0^{b_0} \right) \quad (2)$$

where the index 0 denotes the group of measurements taken in the given cross-section, and the index 1 indicates measurements outside of the profile.

Next, the two groups were transformed separately to the given cross-section per Formula 5. For the transformed data, a new rating curve was plotted, using the non-linear least squares method. The fit of the curve to the data set was described by the indices NSE , NSE_{rel} , and η_{rel} in conformance with 2, 3, and 4.

3. Results and discussion

Table 2 presents the values of the parameters of fit (NSE , NSE_{rel} , and η_{rel}) for the data, both before and after the transformation. In most of the cases analyzed, the rating curve was a slightly better fit to the data after the application of the transformation than before it. However, the differences in most of the parameters are $<1\%$, and, therefore, can be treated as negligible. A greater difference in the parameter η_{rel} in favor of no transformation ($>3\%$) was observed for the water gauge Łąki on the Barycz River.

According to Krause et al. (2005), however, the measures of fit can be doubtful, and consequently, small differences in the values of the parameter may be insignificant. Thus, we conclude that in the cases analyzed, transformation of the measurement data did not improve the fit of data to the rating curve.

Figures 3-7 present the relationship $Q = f(H)$ for the selected representatives of mountain, submontane, and lowland rivers. A difference was observed in the layout of points representing measurements on a plane. In the low stages zone, the scatter of measurement points decreased after the transformation. This result is of great importance in the plotting of the rating curve, as it allows a single description for all measurements from that zone. The transformation also had an impact on the zone of high stages. Because of the difficulties involved in taking measurements at high water stages, that group is never well

represented, and therefore even a slight shift of data causes a big difference in the shape of the rating curve, and consequently, either an overestimation or underestimation of the discharge. Parts (a) and (b) of each of the figures illustrate data before and after the transformation, respectively, with the fitted rating curves. In the right bottom corner of every graph, there is an enlarged area of low water stages. Blue indicates measurements taken in the water gauge profile, i.e., those that were not transformed. Part (c) is a comparison of the fitting of the rating curve before and after the transformation. Green is used for the curve corresponding to non-modified data. Red is used for the curve fitted to the data after the transformation. This makes it easier to notice the differences in the shapes of the curves.

Table 2. Measures of rating curve fitting error.

river		Barycz	Biała Łądecka	Bóbr	Kamienna	Kwisa
water gauge		Łąki	Łądek Zdrój	Jelenia Góra	Jakuszyce	Łozy
NSE	before	0.9416	0.8534	0.9552	0.9126	0.9442
	after	0.9461	0.8655	0.9649	0.9147	0.9469
NSE_{rel}	before	0.9477	0.8495	0.9564	0.91	0.9526
	after	0.9437	0.8607	0.9672	0.9162	0.9518
η_{rel}	before	0.4722	0.4966	0.4387	0.4776	0.3233
	after	0.5063	0.4526	0.3626	0.4651	0.3276

In the case of the water gauge Łąki on the lowland Barycz River, the transformation had only a slight effect on the distribution of the data and the fitting of the rating curve. The values of the indices NSE and NSE_{rel} differ at the level of thousandths (<1%) in favor of the transformation, and the relative error η_{rel} points in favor of no transformation. Differences of this magnitude are insignificant. The differences in the shapes of the curves can be observed in Figure 3c. The curve fitted to the data after the transformation indicates a possibility of somewhat higher stages for high discharge volumes. In the zone of low stages, the rating curve after the transformation is slightly more flattened relative to the initial curve.

Significant changes in the fitting of rating curves to the data after the transformation can be observed in the next two cases analyzed. Figure 4 presents the effect of transformation of data from the water gauge Łądek Zdrój on the Biała Łądecka River. In the zone of low-water stages, a relatively large number of measurements were taken exactly in the water gauge profile, and hence for low discharge volumes, the

difference between the curves before and after the transformation is small. In the zone of high-water stages, in which measuring strictly at the water gauge is often impossible, one can observe a notable difference in the shapes of the curves. No transformation of the data can result in a big underestimation of the level of the high water stage. In addition, the indices NSE , NSE_{rel} , and η_{rel} imply a difference in the goodness of fit in favor of the curve plotted with the transformed data. Similar observations can be made in the case of the water gauge station Jelenia Góra on the Bóbr River (Fig. 5). Also, in this case, all of the parameters indicate a better fit of the curve after the transformation of the measured data. The rating curve for the zone of high-water stages for the data before the transformation is overestimated relative to the curve for the transformed data. In addition, one can note how important it is to take measurements directly in the water gauge profile at low-water stages. The rating curves for data before and after the transformation are divergent also in the zone of low-water stages, i.e., in the zone where the relatively largest number of measurements are made.

In the case of the water gauge station Jakuszyce on the Kamienna River (Fig. 6), we can observe a nearly perfect coincidence of the curves before and after the transformation. This attribute results from the precision of the measurements; only a few of them were taken outside of the water gauge profile. The small difference in the goodness of fit of the curves described by the index η_{rel} results from a slight shift of the measurements taken outside of the water gauge profile in the zone of low-water stages.

In the case of the water gauge station Łoży on the Kwisa River (Fig. 7), the parameters indicate an almost identical level of goodness of fit of the curves to the data sets. Although the majority of the measurements were taken outside of the water gauge profile, the curves differ slightly only in the zone of high-water stages.

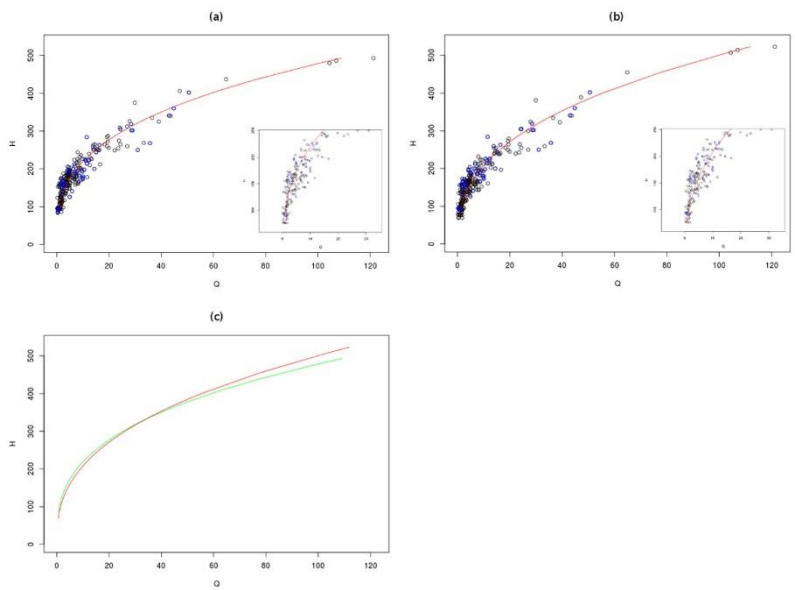


Fig. 3. Rating curve for the Barycz River at water gauge station Łąki; (a) before transformation, (b) after transformation, (c) comparison of rating curves before (green) and after (red) transformation.

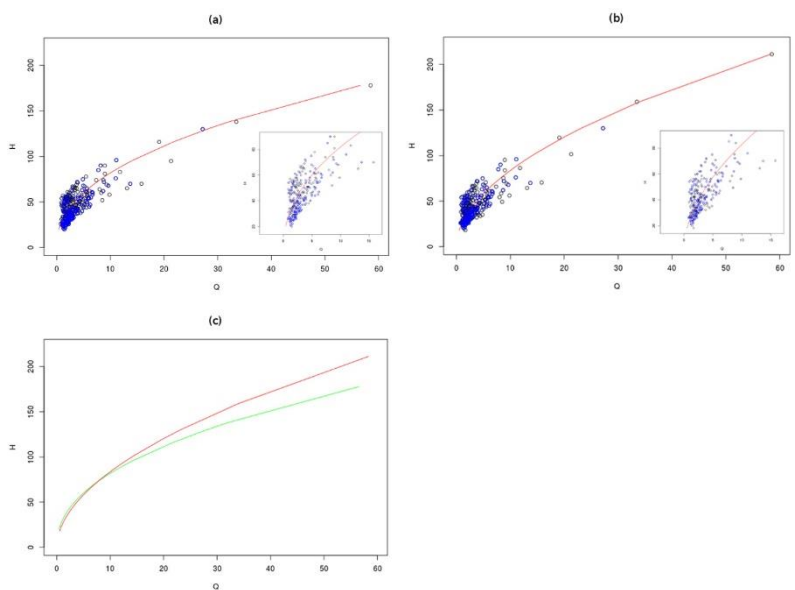


Fig. 4. Rating curve for the Biala Łądecka River at water gauge station Łądek Zdrój; (a) before transformation, (b) after transformation, (c) comparison of rating curves before (green) and after (red) transformation.

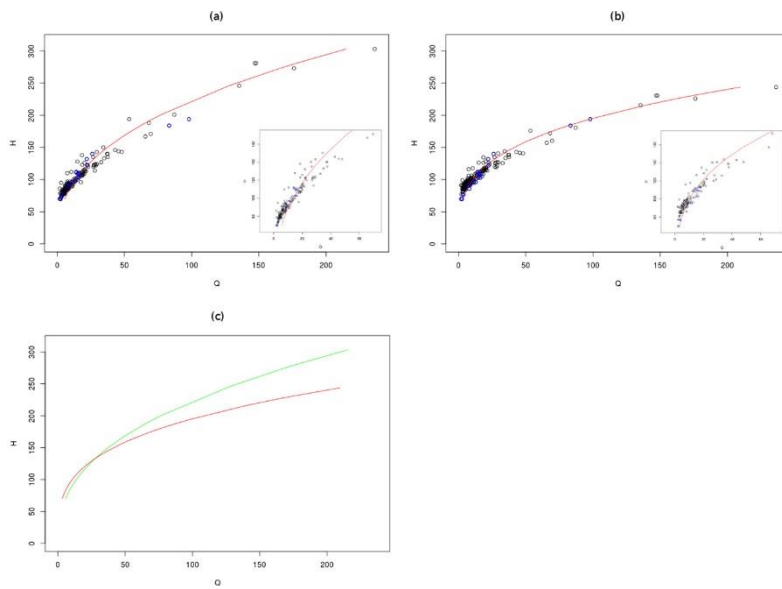


Fig. 5. Rating curve for the Bóbr River at water gauge station Jelenia Góra; (a) before transformation, (b) after transformation, (c) comparison of rating curves before (green) and after (red) transformation.

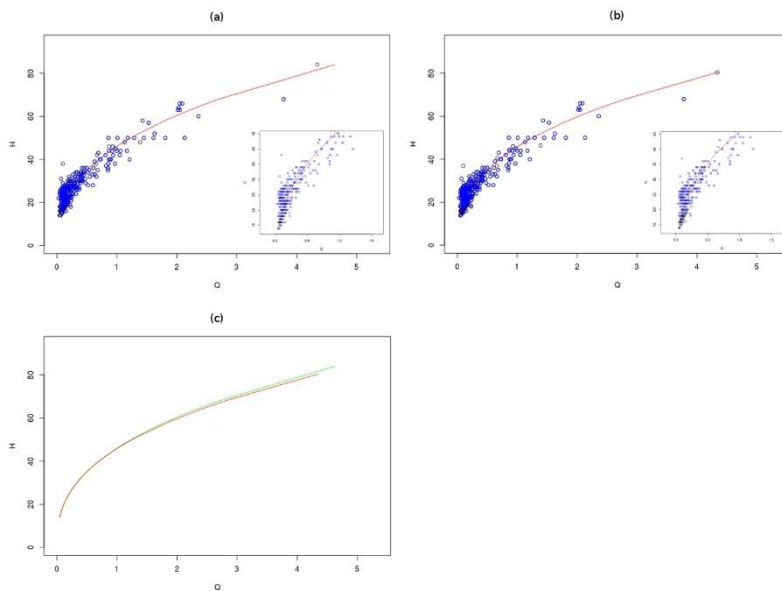


Fig. 6. Rating curve for the Kamienna River at water gauge station Jakuszyce; (a) before transformation, (b) after transformation, (c) comparison of rating curves before (green) and after (red) transformation.

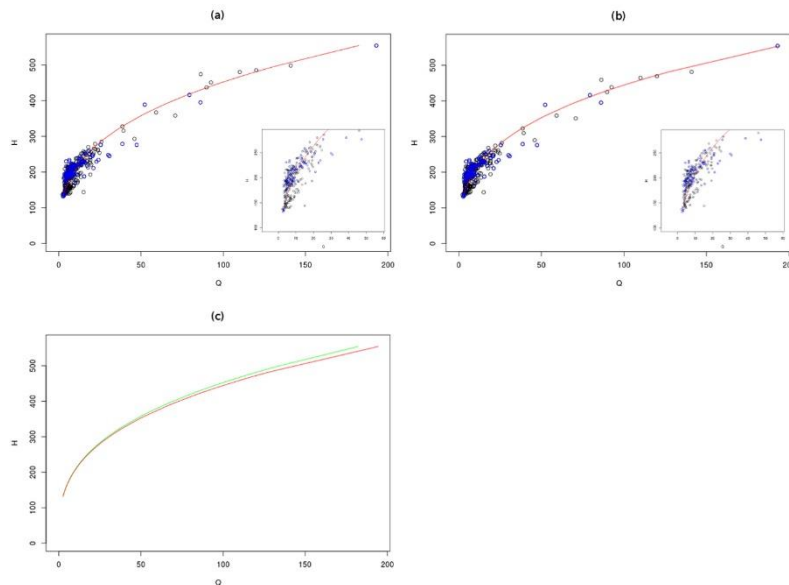


Fig. 7. Rating curve for the Kwisá River at water gauge station Łozy; (a) before transformation, (b) after transformation, (c) comparison of rating curves before (green) and after (red) transformation.

4. Conclusions

The differences between the rating curves for the transformed and untransformed data are greater for rivers on which hydrometric measurements were taken at various and large distances from the water gauge profile. The type of watercourse is also important; measurements from the mountain and submontane rivers, characterized by a greater range of both medium and high flow velocities (as per Table 1) and large variations of cross-section, even over short distances, are more sensitive to the application of the transformation. This means that, especially in the case of rivers of this type, the most accurate rating curve can be obtained by taking hydrometric measurements directly in the water gauge profile.

With automated tools and analytical methods, one can relatively easily fit a curve to a selected data set. The problem appears when a data set is not homogeneous, as then it is not possible to treat all of its elements in the same way. The proposed transformation homogenizes the hydrometric data relative to the place of measurement.

The pre- and post-transformation rating curves fit the data similarly. Small differences in the values of the indices NSE , NSE_{rel} , and η_{rel} can be considered negligible. The similar values indicate that the proposed method fits the rating curve to the data set well, and the transformation does not affect the quality of this fit. The transformation, however, has an impact on the distribution of measurement points both in the zone of low-water stages and in that of high stages. The differences affect the inference and the prediction of discharge rates. Precise determination of the stage-discharge relationship is very important for accurate evaluation of the behavior of catchment basins under various hydrological conditions.

The transformation eliminates one of the sources of inhomogeneity in the hydrometric data, which permits analyses of a partially homogeneous data set. Striving to homogenize data sets at successive levels, for example, to adjust for the measurement method, may consequently lead to simplification of the methods and interpretation of the results of the analyses.

The natural characteristics of watercourses, such as overgrowing, which are not included in the transformation, deserve special attention. These phenomena can have significant impacts on the precise determination of rating curves, especially in lowland rivers.

References

- Bartnik A., Jokiel P., 1997, Zmiany odpływu na obszarze Polski w latach 1971-1990 w świetle analiz jednorodności szeregów przepływu rzek, *Wiadomości Instytutu Meteorologii i Gospodarki Wodnej*, XX (XLI), 4.
- Byczkowski A., 1999, *Hydrologia*, Wydawnictwo SGGW, Warszawa.
- Chauhan M.S., Kumar V., Dikshit P.K.S., Dwivedi S.B., 2014, Comparison of discharge data using ADCP and current meter, *International Journal of Advances in Earth Sciences*, 3 (2), 81-86.
- Delcroix T., Masia F., Eldin G., 1992, Comparison of profiling current meter and shipboard ADCP measurement in the western equatorial Pacific, *Journal of Atmospheric and Oceanic Technology*, 9 (6), 867-871, DOI: 10.1175/1520-0426(1992)009<0867:COPCMA>2.0.CO;2.
- Dębski K., 1955, *Hydrologia kontynentalna. Hydrometria*, Wydawnictwo Komunikacyjne, Warszawa.
- Di Baldassarre G., Montanari A., 2009, Uncertainty in river discharge observations: a quantitative analysis, *Hydrology and Earth System Sciences*, 13 (6), 913-921, DOI: 10.5194/hess-13-913-2009.
- Domeneghetti A., Castellarin A., Brath A., 2012, Assessing rating-curve uncertainty and its effects on hydraulic model calibration, *Hydrology and Earth System Sciences*, 16 (4), 1191-1202, DOI: 10.5194/hess-16-1191-2012.
- Dottori F., Martina M.L.V., Todini E., 2009, A dynamic rating curve approach to indirect discharge measurement, *Hydrology and Earth System Sciences*, 13 (6), 847-863, DOI: 10.5194/hess-13-847-2009.

- Eagelson P.S., 1978, *Hydrologia dynamiczna*, PWN, Warszawa.
- Fenton J.D., Keller R.J., 2001, The calculation of streamflow from measurements of stage, Technical Report 01/6, Cooperative Research Centre for Catchment Hydrology, available online <https://johndfenton.com/Papers/Calculation-of-streamflow-from-measurements-of-stage.pdf> (data access 19.06.2023).
- Gore J.A., Banning J. (eds.), 2017, *Methods in Stream Ecology. Volume 1: Ecosystem Structure*, Academic Press, 506 pp.
- Haque M.M., Rahman A., Haddad K., 2014, Rating curve uncertainty in flood frequency analysis: a quantitative assessment, *Journal of Hydrology and Environment Research*, 2 (1), 50-58.
- Hayes J., Davidson A., Boyton R., Malone D., 2012, Old and new, ADCP vs current meter, AHA 2012 Conference, Melbourne.
- Krause P., Boyle D.P., Base F., 2005, Comparison of different efficiency criteria for hydrological model assessment, *Advances in Geosciences*, 5, 89-97, DOI: 10.5194/adgeo-5-89-2005.
- Lang M., Pobanz K., Renard B., Renouf E., Sauquet E., 2010, Extrapolation of rating curves by hydraulic modelling, with application to flood frequency analysis, *Hydrological Sciences Journal*, 55 (6), 883-898, DOI: 10.1080/02626667.2010.504186.
- Leonard J., Mietton M., Najib H., Gourbesville P., 2000, Rating curve modelling with Manning's equation to manage instability and improve extrapolation, *Hydrological Sciences Journal*, 45 (5), 739-750, DOI: 10.1080/02626660009492374.
- Ozga-Zielińska M., Brzeziński J., 1994, *Hydrologia stosowana*, PWN, Warszawa.
- Ozga-Zieliński B., Szkutnicki J., Chudy Ł., 2014, Krzywa natężenia przepływu a przepływy ekstremalne, *Przegląd Geofizyczny*, LIX (3-4), 85-110.
- Radczuk L., Szymkiewicz R., Jelowicki J., Zyszkowska W., Brun J.F., 2001, Wyznaczanie stref zagrożenia powodziowego, Wrocław: Biuro Koordynacji Projektu Banku Światowego, SAFEGE.
- Reitan T., Petersen-Overleir A., 2009, Bayesian methods for estimating multi-segment discharge rating curves, *Stochastic Environmental Research and Risk Assessment*, 23, 627-642, DOI: 10.1007/s00477-008-0248-0.
- Singh V.P., Strupczewski W.G., 2002, On the status of flood frequency analysis, *Hydrological Processes*, 16 (18), 3737-3740, DOI: 10.1002/hyp.5083.
- Sivapragasam C., Muttill N., 2005, Discharge rating curve extension – a new approach, *Water Resources Management*, 19, 505-520, DOI: 10.1007/s11269-005-6811-2.
- Strupczewski W.G., 1996, Warning of application of the Chezy-Manning formula regardless of channel shape, *Proceedings of the International Conference on Hydrology and Water Resources*, 371-383, DOI: 10.1007/978-94-011-0389-3_24.
- Szkutnicki J., Kadłubowski A., Chudy Ł., 2007, *Metody wyznaczania krzywej natężenia przepływu*, IMGW, Warszawa.
- Szulczewski W., Jakubowski W., 2018, The application of mixture distribution for the estimation of extreme floods in controlled catchment basins, *Water Resources Management*, 32, 3519-3534, DOI: 10.1007/s11269-018-2005-6.
- Szulczewski W., Jakubowski W., Tokarczyk T., 2018, An analysis of the hydrological regime as a factor influencing on the distributions of maximum annual flows, *ITM Web of Conferences*, 23, 00034, DOI: 10.1051/itmconf/20182300034.
- Westerberg I.K., McMillan H.K., 2015, Uncertainty in hydrological signatures, *Hydrology and Earth System Sciences*, 19 (9), 3951-3968, DOI: 10.5194/hess-19-3951-2015.
- Węglarczyk S., 2010, *Statystyka w inżynierii środowiska*, Wydawnictwo PK, Kraków.